

UNIVERSITY OF TRENTO - Italy  
Department of Civil, Environmental  
and Mechanical Engineering



Doctoral School in Civil, Environmental and Mechanical Engineering  
Topic 1. Civil and Environmental Engineering - XXX cycle 2015/2017

Doctoral Thesis - April 2018

Angela Beltempo

# **Study of the aging hereditariness of concrete through a novel viscoelastic formulation**

## **Supervisors**

Prof. Oreste S. Bursi, University of Trento, Italy  
Prof. Daniele Zonta, University of Trento, Italy  
Prof. Massimiliano Zingales, University of Palermo, Italy



*To my family*



*We build too many walls and not enough bridges.*

Joseph Fort Newton



## ACKNOWLEDGEMENTS

First and foremost, I wish to express my deepest and most sincere gratitude to my family and to Pasquale. I would never complete my study successfully without their enormous support, precious advice, and infinite patience and love.

I wish also to thank my supervisors, Professors Oreste S. Bursi, Massimiliano Zingales, and Daniele Zonta. Their great knowledge and guidance benefited me enormously.

Many thanks also to Dr. Alessio Bonelli for numerous fruitful discussions we had, and to Professor Luca Deseri for his cooperation in publishing scientific papers.

The financial contribution of Autostrada del Brennero is also acknowledged and the scientific support of all those who cooperated with me in the modeling of the Colle Isarco viaduct.

Last but not least, my gratitude goes to all beautiful people that I had the fortune to meet in Trento as colleagues, but most importantly as friends, among whom Narges, Vincenzo, Rocco, Roberto, Istiak, and Camilo. Moreover, a big thank to my special friends of Pavia and Giovinazzo.



## ABSTRACT

This thesis focuses on the study of the creep deformations exhibited by concrete structures, with a particular attention to long-span prestressed box girders. During their service life, such structures can experience excessive multidecade deflections mainly due to the creep phenomenon and the large difference in shrinkage between the top and bottom slabs, sometimes causing damages of structural elements and huge economic losses. In order to prevent such consequences, the multidecade deflections of this class of structures need to be carefully predicted; therefore, very refined creep constitutive laws are required for relevant creep analyses. The most widely used creep model for the prediction of the time-dependent behavior of highly creep-sensitive structures is Model B3, which was calibrated through a data bank comprising results coming from different laboratories spread throughout the world. In this thesis, an already existing viscoelastic formulation, conceived for any viscous kernel, is integrated with Model B3 and the resulting finite element scheme is successfully applied to study the long-term behavior of a realistic structure, the Colle Isarco viaduct in Italy. Another contribution to this research work concerns the prediction of multidecade deflections exhibited by concrete structures through a novel creep constitutive law based on variable-order fractional calculus, resulting in an excellent feature with respect to classical creep models. Indeed, the creep deformations obtained through the proposed model are very close to the deformations evaluated by means of Model B3. Moreover, the suggested creep law is characterized by less aging terms than Model B3, with the consequent advantage to exactly derive the relevant relaxation function from the fundamental relationship of linear viscoelasticity. In order to perform creep analyses with the suggested fractional-order law, a numerical integration scheme characterized by a fractional-order viscous kernel is also developed and verified on realistic concrete structures subjected to multiple load histories.

To the best of the author's knowledge, this research work presents the first creep constitutive law available in literature that, through fractional operators, explores the time-dependent behavior of aging materials. Furthermore, a suitable numerical integration scheme is introduced and successfully applied to representative concrete structures.



## PUBLICATIONS

As a result of the work conducted by the author during her years of doctorate, the following publications have been produced:

### Journal publications

- **A. Beltempo**, G. Balduzzi, G. Alfano, F. Auricchio, 2015. Analytical derivation of a general 2D non-prismatic beam model based on the HellingerReissner principle. *Engineering Structures*. Volume 101, Pages 88-98. DOI: <http://dx.doi.org/10.1016/j.engstruct.2015.06.020>.
- **A. Beltempo**, O.S. Bursi, C. Cappello, D. Zonta, M. Zingales, 2017. A Viscoelastic Model for the Long-Term Deflection of Segmental Prestressed Box Girders. *Computer-Aided Civil and Infrastructure Engineering*. Volume 33, Pages 64-78. DOI: 10.1111/mice.12311.
- **A. Beltempo**, M. Zingales, O.S. Bursi, L. Deseri, 2017. A fractional-order model for aging materials: An application to concrete. *International Journal of Solids and Structures*. DOI: <https://doi.org/10.1016/j.ijsolstr.2017.12.024>.
- **A. Beltempo**, A. Bonelli, O.S. Bursi, M. Zingales. A numerical integration approach for fractional-order viscoelastic analysis of hereditary-aging structures. *International Journal for Numerical Methods in Engineering*. Submitted in January 2018 (under review).

### Conference proceeding publications

- **A. Beltempo**, C. Cappello, D. Zonta, A. Bonelli, O.S. Bursi, C. Costa, W. Par-datscher. Structural Health Monitoring of the Colle Isarco Viaduct. IEEE Workshop on Environmental, Energy and Structural Monitoring Systems, EESMS 2015. July 9-10, 2015. Trento, Italy.

- D. Zonta, C. Cappello, **A. Beltempo**, A. Bonelli, D. Bolognani, O.S. Bursi, C. Costa, W. Pardatscher. Structural Retrofit and Health Monitoring of Colle Isarco Viaduct. Structural Faults + Repair. May 17-19, 2016. Edinburgh, United Kingdom.
- C. Cappello, **A. Beltempo**, A. Bonelli, C. Costa, D. Bolognani, O.S. Bursi, D. Zonta, W. Pardatscher. Multi-sensor structural monitoring of Colle Isarco viaduct. 8th International Conference on Bridge Maintenance, IABMAS 2016. June 26-30, 2016. Foz do Iguacu, Brazil.
- C. Cappello, **A. Beltempo**, A. Bonelli, C. Costa, D. Bolognani, O.S. Bursi, D. Zonta. Advanced monitoring system applied to Colle Isarco viaduct. 8th European Workshop on Structural Health Monitoring, EWSHM 2016. July 5-8, 2016. Bilbao, Spain.

# Contents

<b>1</b>	<b>Introduction</b>	<b>1</b>
1.1	Creep and shrinkage of concrete structures . . . . .	1
1.2	Motivation and aim of this thesis . . . . .	3
1.3	Structure of the thesis . . . . .	6
<b>2</b>	<b>A viscoelastic model for the long-term deflection of segmental prestressed box girders</b>	<b>9</b>
2.1	Introduction . . . . .	10
2.1.1	Background and motivation . . . . .	10
2.1.2	Scope . . . . .	13
2.2	A FE formulation for prestressed concrete box girders . . . . .	14
2.2.1	A constitutive creep model: Model B3 . . . . .	14
2.2.2	FE viscoelastic formulation . . . . .	17
2.3	The case study of the Colle Isarco viaduct . . . . .	20
2.3.1	Bridge structural characteristics . . . . .	20
2.3.2	SHM system for field data acquisition . . . . .	23
2.4	FE modeling of the Colle Isarco viaduct . . . . .	27
2.4.1	3D FE model . . . . .	27
2.4.2	1D FE model . . . . .	31
2.4.3	1D model validation and prediction . . . . .	34
2.5	Development of a decision support system . . . . .	37
2.6	Conclusions and future perspectives . . . . .	38
2.A	Pseudocode for the FE formulation . . . . .	41
<b>3</b>	<b>A fractional-order model for aging materials: An application to concrete</b>	<b>43</b>
3.1	Introduction . . . . .	44
3.2	Preliminary remarks on material aging hereditariness . . . . .	47
3.3	The fractional-hereditary aging materials . . . . .	49

3.4	The fractional-aging hereditariness of concrete . . . . .	53
3.4.1	The aging hereditariness of concrete: Model B3 . . . . .	53
3.4.2	The fractional-aging hereditariness of concrete . . . . .	55
3.4.3	Derivation of the aging functions and model comparisons . . . . .	59
3.5	Conclusions . . . . .	63
3.A	Fundamental remarks of fractional calculus . . . . .	67
3.B	Fractional calculus of variable order . . . . .	68
3.B.1	Case 1 $\beta(t, \tau) = \beta(t)$ . . . . .	69
3.B.2	Case 2 $\beta(t, \tau) = \beta(\tau)$ . . . . .	70
3.B.3	Case 3 $\beta(t, \tau) = \beta(t - \tau)$ . . . . .	71
3.C	FHAM functions . . . . .	71
<b>4</b>	<b>A numerical integration approach for fractional-order viscoelastic analysis of hereditary-aging structures</b>	<b>73</b>
4.1	Introduction . . . . .	74
4.1.1	Background and motivation . . . . .	74
4.1.2	Scope . . . . .	76
4.2	Fractional-hereditary aging materials . . . . .	76
4.2.1	Material aging hereditariness . . . . .	77
4.2.2	Remarks on variable-order fractional calculus . . . . .	79
4.2.3	A fractional-hereditary aging constitutive law . . . . .	81
4.3	Structural analysis in presence of fractional-order aging hereditariness . . . . .	83
4.3.1	The FE formulation . . . . .	84
4.4	Convergence analysis . . . . .	90
4.4.1	The model problem . . . . .	90
4.4.2	Results . . . . .	91
4.5	Representative numerical examples . . . . .	96
4.5.1	A 2D frame structure . . . . .	96
4.5.2	A prestressed concrete box girder . . . . .	98

4.6	Conclusions . . . . .	107
4.A	Aging functions for a medium strength concrete for the 2D frame structure	109
4.B	Aging functions for a medium strength concrete for the prestressed concrete box girder . . . . .	111
<b>5</b>	<b>Summary, conclusions and future perspectives</b>	<b>115</b>
5.1	Summary . . . . .	115
5.2	Conclusions . . . . .	117
5.3	Future perspectives . . . . .	119

# List of Figures

2.1	(a)The Koror-Babelthuap Bridge in Palau; (b) the Koror-Babelthuap Bridge failure; (c) the central span of the Colle Isarco viaduct in Italy; (d) Northern lateral spans of the Colle Isarco viaduct. . . . .	13
2.2	DoFs of a plane beam finite element. . . . .	17
2.3	(a) Elevation of the three main spans of the viaduct, and (b) generic cross section of the box-girder. Dimensions in m. . . . .	21
2.4	Comparison between monitoring data (black dots) and design prediction of CEN (2004) (red line) relevant to cross section A of Figure 2.3(a). . .	22
2.5	Configuration of prisms between Piers #8 and #9. Dimensions in m. . .	24
2.6	Configuration of FOSs and PT100 sensors. . . . .	24
2.7	Time histories of deflection and temperature field data. . . . .	25
2.8	Measured deflection at prisms 8N1N and 8N1S and air temperature field data. . . . .	26
2.9	Phases of displacement evolution of upper point at cross section B of Figure 2.3(a) during construction estimated by a 3D FE simulation. . . .	29
2.10	Discretization of the box girder under exam. . . . .	32
2.11	Comparison between 1D FE model predictions and field data of time-deflection profile relevant to cross section A of Figure 2.3(a). . . . .	35
2.12	Deflection effects after the intervention of 2014 and prediction until 2040 relevant to cross section A of Figure 2.3(a). . . . .	36
2.13	The architecture of the decision support system. . . . .	39
3.1	Representation of a spring element $\beta = 0$ , a spring-pot element $0 < \beta < 1$ , and a Newtonian element $\beta = 1$ . . . . .	51
3.2	Creep function of Model B3 for different values of $t_0$ . . . . .	55
3.3	Variable-order fractional Maxwell model. . . . .	56

3.4	Results of the best-fitting procedure with Model B3 creep function and representations of functions $\beta(t_0)$ , $G_\beta(t_0)$ , and $C_\beta(t_0)$ by means of the solid black line. . . . .	63
3.5	Comparisons between the Model B3 creep function and the FHAM creep function for different values of the loading time $t_0$ . . . . .	64
3.6	Comparisons among the Model B3 relaxation function, the FHAM relaxation function, and the reference solution, which was evaluated according to Bažant (1972). . . . .	65
4.1	Variable-order fractional Maxwell model. . . . .	82
4.2	The beam finite element and its DoFs. . . . .	86
4.3	The model problem. . . . .	90
4.4	Global truncation error estimated from $t_0 = 1000$ days to $t_f = 10000$ days by varying $n$ and $r$ , with $nG = 4$ , $k = 30$ and $\bar{n} = 170$ . . . . .	93
4.5	Global truncation error estimated at $t_f = 10000$ days by varying the number of subintervals and the number of Gaussian quadrature points, with $r = 1$ , $k = 30$ and $\bar{n} = 170$ . . . . .	94
4.6	Global truncation error estimated at $t_f = 10000$ days by varying the number of subintervals, the number of Gaussian quadrature points, and the number of terms involved into the Grünwald-Letnikov approximation, with $r = 1$ and $k = 30$ . . . . .	95
4.7	Global truncation error estimated at $t_f = 10000$ days by varying the number of subintervals, the number of Gaussian quadrature points and the number of iterated Kernels, with $r = 1$ and $\bar{n} = 170$ . . . . .	95
4.8	A 2D statically indeterminate frame. . . . .	97
4.9	Time evolution of the horizontal displacement at node $B$ , for two horizontal loads equal to $100kN$ applied at 1000 days to nodes $A$ and $C$ . . . . .	98

4.10	Time evolution of the horizontal displacement at node <i>B</i> , caused by two horizontal loads of 100kN in nodes <i>A</i> and <i>C</i> applied at 1000 days and 4600 days, respectively. . . . .	99
4.11	The Colle Isarco viaduct. . . . .	99
4.12	The static configuration of the main box girder and its generic cross section. . . . .	100
4.13	Mesh used for the creep analysis of the Colle Isarco viaduct. . . . .	102
4.14	Time evolution of the vertical displacement at node 48, where negative values entail downward displacements. . . . .	102

## List of Tables

2.1	Geometrical characteristics. . . . .	28
2.2	Mechanical properties. . . . .	28
2.3	Algorithm for the evaluation of creep strains implemented in the ANSYS software. . . . .	30
2.4	Geometrical characteristics and Model B3 parameters of the cross section at Pier #8, where 'o' indicates the characteristics of old concrete and 'n' indicates the characteristics of the new layer of concrete. . . . .	33
2.5	Load history at Pier #8 during main interventions. . . . .	34
3.1	Mechanical and environmental conditions of a specimen chosen for the best-fitting procedure. . . . .	60
3.2	Values of $\beta$ , $G_\beta$ , and $C_\beta$ obtained through the best-fitting procedure. . . .	61
4.1	Mechanical properties of the medium-strength concrete specimen for the 2D frame structure. . . . .	91
4.2	Mechanical properties of the medium-strength concrete for the prestressed concrete box girder. . . . .	101
4.3	Geometrical characteristics for the FEs of the box girder. . . . .	103
4.4	Loads assigned to each node of the box-girder mesh at $t_0 = 1000$ and $t_0 = 4600$ days. . . . .	105



# Chapter 1

## Introduction

### 1.1 Creep and shrinkage of concrete structures

Nowadays, the most widely used material for the construction of both ordinary and outstanding structures is reinforced concrete, and one of the main reasons for it relates to its durability over years compared with other building materials. Typical phenomena that may strongly influence the time-dependent behavior of reinforced concrete structures are shrinkage and creep. The study of these phenomena and their effects on long-term structural behavior are important issues explored in this thesis.

In structural engineering, the term *shrinkage* indicates the stress-independent deformation observed in a concrete element due to changes in water content and long-term chemical processes. The *creep* is instead a stress-dependent deformation, and it generally describes the tendency of a structural element to increasingly deform under the influence of sustained loads. These two phenomena are strictly related to each other; indeed, the additional stresses induced in the material microstructure by shrinkage usually generate further creep deformations in the whole structural element (Bažant and L'Hermite, 1988; Bažant and Yunping, 1994). Moreover, the volumetric deformation of shrinkage is responsible for the change of material properties; and this phenomenon, known in literature as *aging*, tends to reduce creep deformations in the long term (Bažant, 1975). The time-dependent behavior characterizing aging materials in presence of creep is generally indicated in literature with the term *aging hereditariness* (Jirásek and Bazant, 2002). Due to the intricate interaction between creep and shrinkage, the aging hereditariness exhibited

by concrete structures is generally one of the most challenging time-dependent behaviors to be investigated. The research conducted in this field is very much fertile and several creep and shrinkage models were proposed in literature for the characterization of the material constitutive behavior. However, the choice of the creep and shrinkage constitutive law that better fits the time-dependent behavior exhibited by a concrete structure is not always trivial, also considering the influence of additional factors, such as the geometry of the structural element, environmental conditions, and the amplitude of sustained loads. Along this line, Bažant and Baweja (2000) propose the following approximate classification to guide researchers and practitioners in the model choice.

- Level 1: reinforced concrete beams, frames and slabs with spans under 20 m and heights of up to 30 m, plain concrete footings, retaining walls.
- Level 2: prestressed beams or slabs of spans up to 20 m, high-rise building frames up to 100 m high.
- Level 3: medium-span box girder, cable-stayed or arch bridges with spans of up to 80 m, ordinary tanks, silos, pavements.
- Level 4: long-span prestressed box girder, cable-stayed or arch bridges; large bridges built sequentially in stages by joining parts; large gravity, arch or buttress dams; cooling towers; large roof shells; very tall buildings.
- Level 5: record-span bridges, nuclear containments and vessels, large off-shore structures, large cooling towers, record-span thin roof shells, record-span slender arch bridges.

Overall, the authors state that for Level 1 a creep and shrinkage analysis of the structure is not required. Indeed, concrete beams or frames characterized by short spans are not subjected to evident creep deformations during their service life. Conversely, creep and shrinkage may represent the principal cause of excessive multidecade displacements in structures with longer spans, like bridges and very tall buildings. Therefore, for structures

belonging to Levels 3 and 4, the authors suggest to utilize more refined creep models. With regard to Level 2 and sometimes Level 3, simple creep models are sufficiently adequate; while, for Level 5, the most realistic and accurate analysis has to be performed, which typically consists in a step-by-step computer solution based on a general constitutive law.

An example of creep model suitable for Level 2 is the CEB-FIP creep and shrinkage model (CEB-FIP, 1993) illustrated in the European technical standards on the design of concrete structures - Eurocode 2 (CEN, 2004). This model includes both the material aging and the material hereditariness through two time-dependent terms. Furthermore, it also considers the mechanical properties of concrete and the relative humidity by means of additional terms. However, the model creep function tends to an asymptotic value, a trend which is not observable in the real life of a structure; thus, its inapplicability to Levels 3 and 4. A creep model suitable for Levels 3 and 4 is Model B3 instead, suggested by Bažant and Baweja (2000) and become an international standard recommendation (ACI, 2008). It consists of five parameters and includes a logarithmic term, whose creep effect never tends to an asymptotic value. An improved version of Model B3 has been recently derived by Wendner et al. (2013) and called Model B4. The main differences with respect to Model B3 are: the inclusion of temperature effects; and the separation of the drying and the autogenous components of shrinkage, the latter being particularly important for high strength concrete.

Among the aforementioned creep and shrinkage models and many others available in literature, Model B3 better fits the study faced in this thesis. More information on this matter is addressed hereinafter.

## **1.2 Motivation and aim of this thesis**

The research work presented in this thesis mainly aims to investigate the short- and long-term behavior of structures highly sensitive to creep and shrinkage phenomena. Thus, it focuses on those structures belonging to Levels 4 and 5 of the aforementioned classification, with a particular attention to long-span prestressed concrete box girders.

In long-span prestressed concrete box girders, the combination of creep and shrinkage phenomena with other factors, such as tension losses and the cast-in-place segmental method used for the construction, may lead to excessive multidecade deflections unforeseeable by classical creep models. In Italy, an evidence of this occurrence is the Colle Isarco viaduct (Gentilini and Gentilini, 1972), which represents a strategic highway corridor connecting the North-Eastern part of Italy with Austria. A similar behavior was also recorded for the Koror-Babelthuap Bridge in Palau, which unfortunately collapsed in 1996 (Bažant et al., 2012). In order to prevent further accidents, or simply damages to important structural elements, the future behavior of this class of concrete structures needs to be carefully investigated. However, to the author's knowledge, there is a paucity of research studies dealing with the modeling of highly creep-sensitive structures; major contributions to this research field only concern the development of refined creep constitutive laws for the characterization of the material mechanical behavior. Hence, a preliminary goal of this thesis is to provide useful indications about the modeling of prestressed concrete box girders, e.g.: i) the proper way to combine all load histories, also including construction stages; and ii) the FE technique, with the relevant assumptions, to be utilized in order to obtain highly accurate results in a reasonable computational time. The case study considered for this first research outcome is the aforementioned Colle Isarco viaduct, which is characterized by a relatively simple static configuration, but very complex load histories, i.e. pretensioning of cables, tension losses, and maintenance work. The developed FE model relies on an energetic formulation conceived for linear viscoelastic problems and characterized by a relaxation integral form (Carini et al., 1995b,a). Additionally, in order to describe the material mechanical behavior, the relaxation function of the refined constitutive Model B3 (Bažant et al., 2013) is properly introduced in the formulation.

Another goal of this thesis concerns the development of a novel constitutive model, which can be successfully used as alternative to Model B3 for the study of highly creep-sensitive structures. The proposed model includes variable-order fractional operators (Podlubny, 1998; Lorenzo and Hartley, 2002, 2007); moreover, it consists of three aging

parameters, properly calibrated with the aid of Model B3. The main advantages related to the use of fractional calculus in the field of linear viscoelasticity are: i) the derivation of a simple function for the description of the creep phenomenon; ii) the inclusion of power laws, which are in perfect agreement with experimental curves (Nutting, 1921; Gemant, 1938); and iii) the possibility to exactly derive the relaxation function from the fundamental relationship of linear viscoelasticity (Bažant, 1972); this way, the thermodynamical and mathematical consistency of the constitutive model is guaranteed. However, these advantages and many others were proven through studies on hereditary materials (Di Paola and Zingales, 2012; Deseri et al., 2014c); in other words, materials whose time-dependent behavior does not depend on the material aging, such as some polymers and rubbers. Therefore, this part of the research mainly aims to investigate the effective applicability of fractional operators to the study of the time-dependent behavior of more complex materials, like aging materials; moreover, it aims to verify the validity of the aforementioned advantages even in presence of aging.

In order to perform creep analyses on realistic structures with the proposed constitutive law, a suitable numerical integration scheme is also presented as further research outcome of this thesis. The method relies on an already existing FE formulation (Carini et al., 1995b), properly integrated with the fractional-order relaxation function. A convergence analysis is then performed to set the value of some variables affecting the solution quality, such as the number of Gaussian points or the number of subintervals involved in the step-by-step integration procedure (Carini et al., 1995a). The FE scheme is finally utilized to study both the short- and long-term behavior of representative concrete structures, including the Colle Isarco viaduct.

Eventually, further developments of this thesis concern the correlation of the three parameters characterizing the fractional-order creep model with the mechanical properties of the material, and the extension of the relevant numerical integration scheme to the case of multidimensional bodies.

### 1.3 Structure of the thesis

This thesis illustrates the major research outcomes achieved by the author during her years of doctorate. Moreover, it is organized as a collection of three journal publications, for a total number of five chapters. A brief overview of the remaining chapters follows:

- Chapter 2 includes the publication titled: 'A viscoelastic model for the long-term deflection of segmental prestressed box girders'. The manuscript begins with a literature review on the principal effects that time-dependent phenomena may generate in a specific class of concrete structures, i.e. segmental prestressed box girders. Then, a careful description of an already existing energetic formulation (Carini et al., 1995b) and its integration with the approximate relaxation function of Model B3 follows (Bažant et al., 2013). The presented formulation is applied to the study of a realistic concrete structure, the Colle Isarco viaduct in Italy. Furthermore, many details about the implementation of its geometry and load history into the aforementioned FE formulation are provided, together with a discussion of model results.
- Chapter 3 includes the publication titled: 'A fractional-order model for aging materials: An application to concrete'. The manuscript begins with a literature review on the classical creep models utilized for both hereditary and aging materials. Also, particular attention is given to those models already developed within the framework of fractional-order calculus. General definitions of material aging hereditariness and fractional-order operators are then provided. Finally, a novel fractional-hereditary aging model, properly calibrated with the aid of Model B3, is presented.
- Chapter 4 includes the publication titled: 'A numerical integration approach for fractional-order viscoelastic analysis of hereditary-aging structures'. The manuscript begins with a literature review on the principal models adopted for the characterization of the aging hereditariness of concretes. Moreover, some FE techniques

utilized in the same context are illustrated, focusing on the general FE formulation proposed by Carini et al. (1995b). This formulation is then particularized to include the fractional-order constitutive model proposed in Chapter 3. In addition, in order to set the values of some variables affecting the solution quality, a convergence analysis is performed with the aid of a model problem. Interesting applications to realistic concrete structures follow, including the Colle Isarco viaduct.

- Chapter 5 summarizes conclusions with future perspectives.



## **Chapter 2**

# **A viscoelastic model for the long-term deflection of segmental prestressed box girders**

*by Angela Beltempo, Oreste S. Bursi, Carlo Cappello, Daniele Zonta, and Massimiliano Zingales*

### **Abstract**

Most of segmental prestressed concrete box girders exhibit excessive multidecade deflections unforeseeable by past and current design codes. In order to investigate such a behavior, mainly caused by creep and shrinkage phenomena, an effective FE formulation is presented in this paper. This formulation is developed by invoking the stationarity of an energetic principle for linear viscoelastic problems and relies on the Bazant creep constitutive law. A case study representative of segmental prestressed concrete box girders susceptible to creep is also analyzed in the paper, i.e. the Colle Isarco viaduct. Its FE model, based on the aforementioned energetic formulation, was successfully validated through the comparison with monitoring field data. As a result, the proposed 1D FE model can effectively reproduce the past behavior of the viaduct and predict its future behavior with a reasonable run time, which represents a decisive factor for the model implementation in a decision support system.

## **2.1 Introduction**

### **2.1.1 Background and motivation**

"Clarification of the causes of major disasters and serviceability losses has been, and will always be, a prime opportunity for progress in structural engineering" (Bažant et al., 2012). This need always arises behind important upgrades in design codes and is followed by many researchers for a better understanding of complex phenomena.

According to that need, this study will cover a specific class of bridges, i.e. prestressed concrete box girders, which reveal excessive multidecade deflections unforeseeable by past and current design codes. For instance, let us examine the Koror-Babelthuap Bridge in Palau, depicted in Figures 2.1(a) and 2.1(b), which collapsed in 1996 mainly due to an excessive creep deflection recorded at midspan; or other four segmental prestressed box girders in Japan, which exhibited a similar behavior (Koshirazu, Tsukiyono, Konaru, and Urado) (Bažant et al., 2012). An example in Europe, proving once more that the multidecade deflections are not unique occurrences for the Koror-Babelthuap Bridge, is represented by the Colle Isarco viaduct, shown in Figures 2.1(c) and 2.1(d), which still constitutes a strategic link in the highway corridor connecting Northern Italy with Germany.

Specifically, the excessive multidecade deflections of the aforementioned box girders and many others bridges spread throughout the world may be due to the combination of several factors (Beltempo et al., 2015) listed herein: i) the cast-in-place segmental method used for construction; ii) creep deformation; iii) losses of pre-tensioning force in tendons; and iv) differential shrinkage between top and bottom slabs. However, with regard to the Colle Isarco viaduct, i.e. the case study of this paper, any attempt to investigate the midspan deflection drift using the classical CEB-FIP creep and shrinkage models (CEB-FIP, 1993) - those currently recognized by Eurocode 2 (CEN, 2004)- failed to provide a convincing explanation/prediction. In fact, according to the CEB-FIP model, creep effects become negligible 20 years after concrete casting, whilst the Colle Isarco viaduct experiences a

deflection still growing 40 years after its construction. Thus, the hyperbolic law exploited in Eurocode 2 creep models clearly exhibits limitations to its applicability. Bažant et al. (2012), focusing on Koror-Babelthuap Bridge, also demonstrated that classical CEB-FIP shrinkage and creep models are clearly not suited for reproducing the long-term deflection of large-span segmentally-erected box girders and recommended the use of creep Model B3 (Bažant and Baweja, 2000), which has been recently improved in Model B4 (Wendner et al., 2013). Unlike CEB-FIP models, both Model B3 and Model B4 consider a creep component whose effect persists even many decades after concrete casting. Moreover, they properly take into account difference in shrinkage between top and bottom slabs of the box girder, a phenomenon that could strongly influence the deflection trend. Model B4 includes two major improvements with respect to Model B3: the first is the inclusion of temperature effects in the creep function; the second concerns the separation of the drying and the autogenous components of shrinkage, particularly important for high strength concrete.

An innovative approach to investigate excessive deflections in massive concrete structures could be the introduction of fractional (real-order) operators into the creep constitutive law (Di Paola and Zingales, 2012; Di Paola et al., 2013b). Specifically, the use of fractional operators could bring significant computational savings to model calibration due to the reduced number of parameters -about three- involved into the formulation. However, both Di Paola and Zingales (2012) and Di Paola et al. (2013b) applied fractional operators to hereditary materials, e.g. polymers, and not to aging materials like concrete. Therefore, in this research work we focus on Model B3 mainly because its creep and relaxation functions (Bažant and Baweja, 2000; Bažant et al., 2013), can be fitted by fractional operators. Moreover, a reliable relaxation function is not yet available for Model B4 and, therefore, Model B3 is preferred.

Significant aspects relative to monitoring and modeling of segmental box girders should worthy of investigation. In fact, in most cases, the inexplicable behavior of this specific class of structures led to the installation of efficient Structural Health Monitoring (SHM) systems and to the development of FE models. This is the case of the Colle

Isarco viaduct, for which both field data -revealed to assess the effectiveness of the last maintenance work undertaken in 2014- and FE model predictions were used to provide information on future structural performance and to support decisions concerning the viaduct management. The SHM system installed on the Colle Isarco viaduct includes: i) fiber-optic sensors based on fiber Bragg gratings (Balageas et al., 2010; Glisic and Inaudi, 2008) to measure strains of top and bottom slabs; ii) PT100 resistance thermometers to acquire temperature variations along the whole structure; and iii) a topographic network with prisms to measure displacements. This fusion of data coming from different sensors certainly reduces uncertainties regarding structural behavior (Han et al., 2017), helps the bridge manager to identify causes of possible anomalies and improves his or her capability to take optimal decisions (Cappello et al., 2016).

As further support for computational frameworks for Bayesian inference and bridge maintenance decisions, a 1D FE model of the Colle Isarco viaduct, which is presented in this paper, was also developed. Along the same lines, Caracoglia et al. (2009) developed a time-domain FE model to better interpret the behavior of long-span modern bridges under vortex shedding-induced loads. Torbol et al. (2013) used a FE analysis to evaluate bridge fragility throughout its service life. Shapiro (2007) built a FE model of the Interstate Highway 565 Bridge in Huntsville (Alabama), to investigate the main causes of cracking phenomena observed just after the construction of the bridge. The main difference between the aforementioned models and the model of the Colle Isarco viaduct is that they are all available in commercial software, mainly ANSYS or OpenSEES (Mazzoni et al., 2006); conversely, the Colle Isarcos model is implemented in MATLAB and relies on an energetic formulation for linear viscoelastic problems (Carini et al., 1995b). Another important aspect is its reduced run time, which is determinant for both stochastic computations and model implementation in a Decision Support System (DSS). In sum, to the authors knowledge, there is a paucity of papers dealing with modeling of creep and shrinkage phenomena for simple yet effective FE simulations of complex segmental prestressed concrete box girders; box girders that, in addition, are subjected to complex loading histories. These are the important issues that the paper explores further.



(a)



(b)



(c)



(d)

Figure 2.1: (a)The Koror-Babelthuap Bridge in Palau; (b) the Koror-Babelthuap Bridge failure; (c) the central span of the Colle Isarco viaduct in Italy; (d) Northern lateral spans of the Colle Isarco viaduct.

### 2.1.2 Scope

This paper presents the main issues regarding the modeling of creep and shrinkage phenomena for a specific class of bridges, i.e. segmental prestressed concrete box girders subjected to complex loading histories. It also shows how a reliable SHM system coupled to an effective FE model can be used to investigate the past behavior and predict the short- and long-term deflection of such complex structures, considering, as representative case study, the Colle Isarco viaduct. According to this aim, we organize the paper as

follows. Firstly, Section 2.2 describes an energetic formulation and a creep constitutive law suitable for the problem under investigation. Section 2.3 introduces a segmental prestressed concrete box girder, i.e. the Colle Isarco viaduct, focusing on the main structural characteristics and the SHM system installed on the viaduct in 2014. Section 2.4 provides details about the implementation of the viaduct geometry and the whole load history into the FE formulation, together with model results. Moreover, an overview of the conceived DSS as further development of this research work can be found in Section 2.5. Finally, we present conclusions and future developments in Section 2.6.

## 2.2 A FE formulation for prestressed concrete box girders

In this section, we propose an effective way to model segmental prestressed concrete box girder deflection and, generally, all structures highly sensitive to creep, without resorting to commercial software analyses. Hence, we present a 1D FE formulation by invoking the stationarity of a functional for linear viscoelastic problems, which relies on the creep constitutive law of Bazant (Bažant and Baweja, 2000).

Hereinafter, we recall the Bazants creep law, known in the literature as Model B3 (Bažant and Baweja, 2000); and present, in greater detail, an energetic formulation for concrete (aging) materials derived from a previous formulation proposed by Carini et al. (1995b).

### 2.2.1 A constitutive creep model: Model B3

In its most general form, Model B3 (Bažant and Baweja, 2000) assumes that, for a constant stress  $\sigma$  applied at age  $t_0$ , the resulting strain  $\varepsilon(t)$  at time  $t$  can be expressed as,

$$\varepsilon(t) = J_{B3}(t, t_0) \cdot \sigma + \varepsilon_{sh}(t) + \alpha \cdot \Delta T(t) \quad (2.1)$$

in which  $J_{B3}(t, t_0)$  defines the compliance function, i.e. strain at time  $t$  caused by a unit uniaxial constant stress at  $t_0$ ,  $\varepsilon_{sh}$  is the shrinkage strain,  $\Delta T$  defines the temperature variation, and  $\alpha$  the thermal expansion coefficient. Furthermore, we can conceive the

compliance function as the sum of three components,

$$J_B(t, t_0) = q_1 + C_0(t, t_0) + C_d(t, t_0, t') \quad (2.2)$$

where  $q_1$  defines the instantaneous strain due to a unit stress,  $C_0$  is the compliance function for basic creep, meaning the creep at constant moisture content and no moisture movement through the material, and  $C_d$  defines the compliance function for drying starting at time  $t'$ .

The basic creep compliance can be further broken down into,

$$C_0(t, t_0) = q_2 Q(t, t_0) + q_3 \ln [1 + (t - t_0)^n] + q_4 \ln(t/t_0) \quad (2.3)$$

where function  $Q$  is discussed in more detail in Bažant and Baweja (2000). The terms in (2.3) containing  $q_2$ ,  $q_3$ ,  $q_4$  represent the aging viscoelastic compliance, non-aging viscoelastic compliance and flow compliance, respectively, as deduced from the solidification theory. The drying compliance  $C_d$  reads,

$$C_d(t, t_0, t') = q_5 \left[ \exp \{-8H(t)\} - \exp \{-8H(t'_0)\} \right]^{1/2} \quad (2.4)$$

where  $H$  is the hydraulic radius of the section, i.e. the volume-to-surface ratio and  $t'_0 = \max(t', t_0)$ . Evidently, Equation (2.4) is valid for  $t > t'_0$ , otherwise it is equal to zero. The five parameters of Model B3 can be either treated as statistical variables or estimated through the following formulas, valid only for certain ranges of material mechanical properties (Bažant and Baweja, 2000), i.e.,

$$q_1 = 0.6 \cdot 10^6 / E_{28} \quad (2.5a)$$

$$q_2 = 185.4 c^{0.5} \bar{f}_c^{-0.9} \quad (2.5b)$$

$$q_3 = 0.29 (w/c)^4 q_2 \quad (2.5c)$$

$$q_4 = 20.3 (a/c)^{-0.7} \quad (2.5d)$$

$$q_5 = 7.57 \cdot 10^5 \bar{f}_c^{-1} |\varepsilon_{sh\infty}|^{-0.6} \quad (2.5e)$$

All the formulas above are given in SI (metric) units (MPa, m). In addition,  $E_{28}$  is the Young's modulus at 28 days,  $\bar{f}_c$  defines the cylinder compression strength,  $w/c$  is water-cement ratio,  $a/c$  is aggregate-cement ratio, and  $\varepsilon_{sh\infty}$  is the shrinkage strain at infinity.

Once the compliance function and its five parameters are known, it is also possible to estimate the corresponding relaxation function  $G_{B3}$  through the following approximate formula (Bažant et al., 2013),

$$G_{B3}(t, t_0) = \frac{1}{J_{B3}(t, t_0)} \cdot \left[ 1 + \frac{c_1 \alpha(t, t_0) J_{B3}(t, t_0)}{q J_{B3}(t, t - \eta)} \right]^{-q} \quad (2.6)$$

where,

$$c_1 = 0.0119 \cdot \ln(t_0) + 0.08 \quad (2.7a)$$

$$\alpha(t, t_0) = \frac{J_{B3}\left(\frac{t + t_0}{2}, t_0\right)}{J_{B3}\left(t, \frac{t + t_0}{2}\right)} - 1 \quad (2.7b)$$

$$q = 10 \quad \eta = 1 \quad (2.7c)$$

Unlike the formula developed in 1979 by Bažant and Kim (1979), Equation (2.6) prevents any violation of the thermodynamic requirement of negatives of  $G_{B3}(t, t')$ . Therefore, (2.6) can be utilized to describe the long-time relaxation phenomenon of concrete loaded at a young age; for this reason, it is particularly useful for compliance functions that correctly describe multidecade creep, which is the case of the Model B3 compliance function.

In summary, Model B3 depends on five different terms, controlled by parameters  $q_1$ ,  $q_2$ ,  $q_3$ ,  $q_4$ , and  $q_5$ . The first three components roughly reproduce the same effect as the classical CEB-FIP model (CEB-FIP, 1993) and have no impact on the long-term behavior. In contrast, the flow compliance term, including  $q_4$ , is unique to Model B3 and to the aforementioned Model B4 (Wendner et al., 2013); it depends on the logarithm of

time and, thus, keeps producing its effects in the long term. Lastly, the term involving  $q_5$ , which depends on the effective thickness  $H$ , allows us to properly take into account the differential drying rate of the two (bottom/top) slabs of box girders.

### 2.2.2 FE viscoelastic formulation

In order to take into account creep effects, we start from the classical total potential energy with an additional integration over time. Moreover, we assume the classical hypotheses of Bernoulli-Navier and first-order beam theories, denoting with  $x$  the coordinate of the beam longitudinal axis,  $u(x, t)$  the longitudinal displacement, and  $v(x, t)$  the transversal displacement of the generic point of the beam. Hence,  $x$  defines the local axis of the beam and, in the case under investigation, it matches the global axis.

The extension of the total potential energy functional to viscoelasticity reads,

$$F[u, v] = \frac{1}{2} \int_{t_0}^t \int_0^L G(x, t_0, t_0) \left[ A \left( \frac{\partial \hat{u}(x, t)}{\partial x} \right)^2 + I \left( \frac{\partial^2 \hat{v}(x, t)}{\partial x^2} \right)^2 \right] dx dt + \quad (2.8)$$

$$- \int_{t_0}^t \int_0^L p(x, t) \hat{u}(x, t) dx dt - \int_{t_0}^t \int_0^L q(x, t) \hat{v}(x, t) dx dt$$

where  $[t_0, t]$  is the time interval,  $G(x, t_0, t_0)$  defines the viscous relaxation kernel evaluated at  $t_0$ , and  $p(x, t)$  and  $q(x, t)$  are the longitudinal and transversal components of distributed load, respectively; whereas,  $\hat{u}(x, t)$  and  $\hat{v}(x, t)$  define the solution of the auxiliary problem.

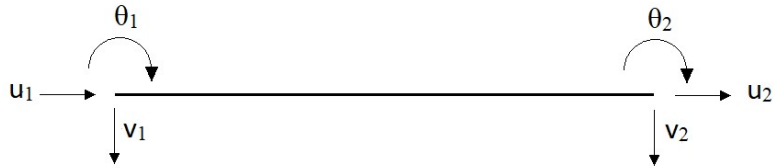


Figure 2.2: DoFs of a plane beam finite element.

Now, among the admissible displacement fields, the solution of the viscoelastic problem, in the given time interval, is the field that makes the functional minimum. The

admissible displacement fields are intended as those that satisfy both compatibility equations and the Dirichlet boundary condition.

Due to the double dimension of the integral, we need to introduce into (2.8) both space and time discretizations. For the spatial discretization, beam finite elements with three DoFs per node are considered. Figure 2.2 depicts a single beam finite element with its six DoFs. In addition, we take into account the classical linear shape functions for the extensional DoFs  $\mathbf{r}_u = [u_1 \quad u_2]^T$ , and the classical cubic shape functions for the bending DoFs  $\mathbf{r}_v = [v_1 \quad \theta_1 \quad v_2 \quad \theta_2]^T$ . The shape functions, referring to each node of the mesh, are collected into the operator  $\mathbf{N}(x)$  and the corresponding nodal DoFs into the vector  $\mathbf{r}(t)$ . Thus, we can express the displacement vector  $\mathbf{u} = [u \quad v]^T$  as follows,

$$\mathbf{u} = \begin{bmatrix} \mathbf{n}_u^T & \mathbf{0}^T \\ \mathbf{0}^T & \mathbf{n}_v^T \end{bmatrix} \cdot \begin{bmatrix} \mathbf{r}_u \\ \mathbf{r}_v \end{bmatrix} = \mathbf{N}(x)\mathbf{r}(t) \quad (2.9)$$

where  $\mathbf{r}(t) = \mathbf{A}\boldsymbol{\alpha}(t)$ ; moreover,  $\mathbf{A}$  denotes the coordinate transformation operator and  $\boldsymbol{\alpha}(t)$  the vector of nodal DoFs. With regard to the time discretization, the vector  $\boldsymbol{\alpha}(t)$  reads,

$$\boldsymbol{\alpha}(t) = \mathbf{M}(t)\boldsymbol{\beta} \quad (2.10)$$

It expresses the product of time shape functions, collected into the operator  $\mathbf{M}(t)$ , and time DoFs, collected into the vector  $\boldsymbol{\beta}$ . For each spatial DoF, we consider two linear time shape functions, for a total of 12 DoFs per beam finite element. The first time shape function is 0 at the beginning of the time step and 1 at the end of the time step, whilst the second is 1 at the beginning and 0 at the end.

The discretized form of (2.8) reads,

$$\begin{aligned}
F[u, v] = & \frac{1}{2} \int_{t_0}^t \hat{\boldsymbol{\alpha}}^T(t) \left\{ \int_0^L G(x, t_0, t_0) \left[ A \left( \frac{d\mathbf{n}_u(x)}{dx} \right) \left( \frac{d\mathbf{n}_u(x)}{dx} \right)^T + \right. \right. \\
& \left. \left. + I \left( \frac{d^2 \mathbf{n}_v(x)}{dx^2} \right) \left( \frac{d^2 \mathbf{n}_v(x)}{dx^2} \right)^T \right] dx \right\} \hat{\boldsymbol{\alpha}}(t) dt - \int_{t_0}^t \hat{\boldsymbol{\alpha}}^T(t) \left\{ \int_0^L \mathbf{n}_u(x) p(x, t) dx \right\} \hat{\boldsymbol{\alpha}}(t) dt + \\
& - \int_{t_0}^t \hat{\boldsymbol{\alpha}}^T(t) \left\{ \int_0^L \mathbf{n}_v(x) q(x, t) dx \right\} \hat{\boldsymbol{\alpha}}(t) dt
\end{aligned} \tag{2.11}$$

The vector  $\hat{\boldsymbol{\alpha}}(t)$  of the 'fictitious' displacement unknowns can be obtained by means of the aforementioned auxiliary elastic problem with the following longitudinal and transversal distributed loads,

$$\hat{p}(x, t) = -\frac{\partial}{\partial x} \left( G(x, t, t_0) A \frac{\partial u(x, t)}{\partial x} \right) - \frac{\partial}{\partial x} \int_{t_0}^t G(x, t, \tau) A \frac{\partial du(x, \tau)}{\partial x} \tag{2.12a}$$

$$\hat{q}(x, t) = -\frac{\partial^2}{\partial x^2} \left( G(x, t, t_0) I \frac{\partial^2 v(x, t)}{\partial x^2} \right) - \frac{\partial^2}{\partial x^2} \int_{t_0}^t G(x, t, \tau) I \frac{\partial^2 dv(x, \tau)}{\partial x^2} \tag{2.12b}$$

named 'fictitious' loads by Carini et al. (1995b). Invoking the stationarity of the classical total potential energy functional, we reach the following resolving system for the auxiliary problem,

$$\mathbf{k} \hat{\boldsymbol{\alpha}}(t) = \mathbf{H} \boldsymbol{\beta} \tag{2.13}$$

with  $\mathbf{k}$  the well-known elastic stiffness operator of the assembled structure and,  $\mathbf{H}$ , an operator depending on both the relaxation kernel and the time shape functions. Hence, we can derive the vector  $\hat{\boldsymbol{\alpha}}(t)$  from (2.13) and, then, introducing its expression into (2.11), its minimum is reached when  $\boldsymbol{\beta}$  corresponds to the solution of the following linear system,

$$\mathbf{L} \boldsymbol{\beta} = \mathbf{g} \tag{2.14}$$

where  $\mathbf{L}$  is the extended stiffness operator and  $\mathbf{g}$  is the extended vector of equivalent nodal forces.

In order to specialize the solution to the case of aging materials, it is necessary to consider a proper creep model into the formulation. For instance, according to the reasoning set out in Section 2.1 for box girders under investigation, the relaxation function of Model B3 (2.6) has to be replaced into (2.12). Moreover, the subdivision of the whole time step into small subintervals will further improve the proposed formulation. As a result, a sequence of smaller problems can be solved and, at every step, the calculation is accomplished by starting from the results available from previous steps. A pseudocode, summarizing the whole FE viscoelastic formulation, is reported in the Appendix 2.A.

## **2.3 The case study of the Colle Isarco viaduct**

### **2.3.1 Bridge structural characteristics**

The Colle Isarco viaduct is an example of segmental prestressed concrete box girder that experienced excessive multidecade deflections just after its construction. It was designed by engineers Bruno and Lino Gentilini and erected between 1968 and 1971 (Gentilini and Gentilini, 1972). Overall, the viaduct comprises two structurally independent decks, the so-called North and South carriageways, with 13 spans, for a total length of 1028.2 m. The main span of the viaduct, 163 m long, consists of two symmetric reinforced concrete Niagara box girders, which support a suspended beam of 45 m, as depicted in Figure 2.3. Each box girder ends with a 59m-long cantilever, counterbalanced by a back arm with a length of 91 m. Moreover, each box girder is composed of 33 box-girder cast-in-place segments with a depth varying from 10.93 m, at the pier, to 2.57 m, at the edge. The thickness of the top slab of the box girder is constant at 0.29 m, whilst the bottom slab varies from 0.99 m to 0.12 m. A concrete of nominal class  $R_{ck} = 450$  kg/cm<sup>2</sup> (C35/45 according to Eurocode 2 (CEN, 2004)) was used for all cast-in-place elements of piers and girders. The initial prestressing was applied through 32 mm diameter Dywidag ST 85/105 threaded bars, with 1030 MPa nominal tensile strength and an initial

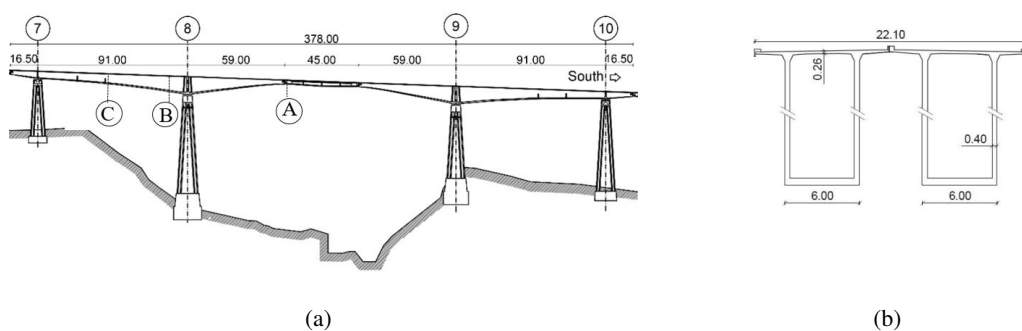


Figure 2.3: (a) Elevation of the three main spans of the viaduct, and (b) generic cross section of the box-girder. Dimensions in m.

jacking tension of 720 MPa. For each 59m-long cantilever, the longitudinal force above the pier was about 120 MN and was provided by a total of 266 cables. As mentioned in Section 2.1, after only a few years from the viaduct opening, monitoring field data started to exhibit a deflection drift that cannot be explained using classical creep models such as those found in most design codes, e.g. Eurocode 2 (CEN, 2004). In this respect, Figure 2.4 depicts the deflection trend recorded at cross section A of Figure 2.3(a). In stark contrast with the design prediction (CEN, 2004) of 160 mm in 1988, the actual deflection reached 230 mm with an apparent rate of 8 mm/year. A similar behavior was also observed for the other three box girders. These first observations prompted the owner to undertake, between 1988 and 1989, a radical intervention. Specifically, 10 cm of road pavement was removed from the cantilever arms and the suspended central beam, and replaced with a thinner layer of lightweight asphalt. The effect of this work is evident in Figure 2.4 through the immediate recovery of 70 mm in deflection and the disappearance of the deflection drift for a few years after the intervention. A second major maintenance activity was accomplished between 1998 and 1999, with the aim of repairing the concrete cover of the top slab, heavily deteriorated by the extensive use of salt during winter. The repair consisted of a scarification of the damaged concrete, replacement of corroded unprestressed bars, and restoration of the damaged concrete cover. In the following years, dumpy level measurements showed once more an increase in deflection drift. Therefore,

another important intervention followed in 2014, which mainly involved the installation of an external post-tensioning system within the four box girders. The retrofit was designed by the Autostrada del Brennero SpA technical office in collaboration with an engineering consultant, SEICO SRL. The additional prestress was provided by a total of 212 0.6" diameter compact strands, with a jacking load of 213 kN. The additional longitudinal force produced above the pier was about 45 MN, which is almost 40% of the original prestress. To compensate the additional post-tensioning force, the thickness of the top slab of the box girder was increased from 260 mm to 290 mm. This last intervention led to a recovery of 80 mm in deflection and a change from negative to positive deflection slope. Other minor work was carried out along with the post-tensioning. Details of the retrofit work can be found in the relevant design documentation (Viviani, 2013).

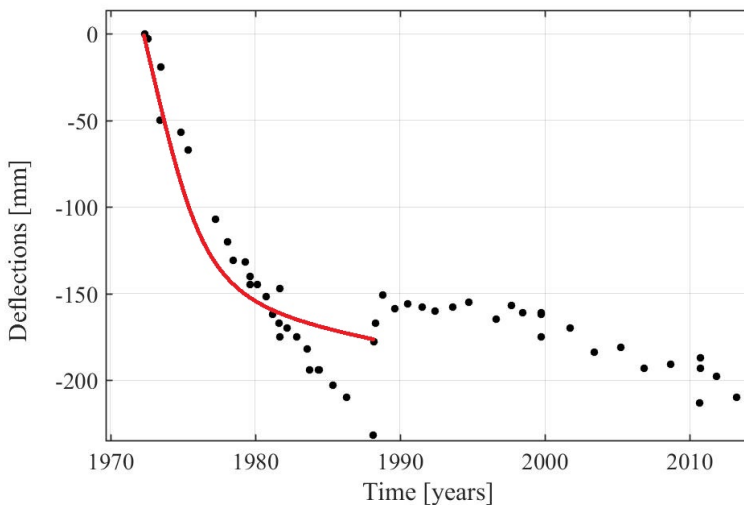


Figure 2.4: Comparison between monitoring data (black dots) and design prediction of CEN (2004) (red line) relevant to cross section A of Figure 2.3(a).

### 2.3.2 SHM system for field data acquisition

The SHM system recently installed on the viaduct consists of three different sets of instruments, each based on a different technology. The first set is made of two Leica TM50 topographic total stations and 72 GPR112 prisms. It was installed and activated in early 2014, so it managed to record the effects of the retrofit intervention. The total stations can detect the position of each prism with a precision in the range of 2 to 20 mm, every hour. The second and third set of the system were installed in June 2016 but have not yet been activated. These are made of 56 fiber optic sensors (FOSs) implementing fiber Bragg gratings (FBGs) and 74 PT100 platinum resistance thermometers connected to their respective reading units. The topographic network was designed to monitor the deflection of the decks between Piers #7 and #10 during the structural intervention and afterwards. The total stations were installed on a 1.50 m-high concrete pile and protected by low-iron glass, a type of glass that minimizes the measurement error due to refraction. The location of the two stations was chosen both to ensure stability and to maximize the precision of the measurements. In general, the latter is enhanced by placing the measurement points and the benchmarks at approximately the same distance from the total stations and at the same altitude. The location of the 60 prisms used as measurement points and the 12 benchmarks is depicted in Figure 2.5. In order to reduce the uncertainty (Kirkup and Frenkel, 2006), 6 benchmarks were used for each total station and were positioned in sparse locations around the Isarco Valley.

The systems based on FOSs and PT100 sensors were designed to monitor the long-term effects of the recent post-tensioning intervention and to assist the investigation into possible structural anomalies. These systems record the strain of both the top and bottom slabs of the box girders and the temperature pattern between Piers #7 and #10. The FBGs sensors measure the average uniaxial strain with a base of 2.00 m, whilst the PT100 resistance thermometers measure local temperature. Each instrumented section contains 4 FOSs, 2 for each deck, 1 for each slab, whilst 4 acquisition units are located near Piers #8 and #9. In total, 14 sections are measured using the FOSs. The temperature field is

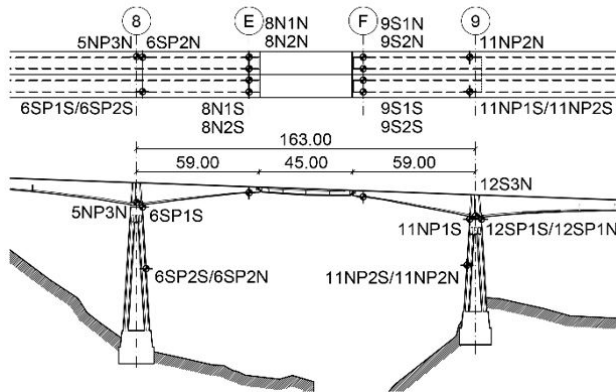


Figure 2.5: Configuration of prisms between Piers #8 and #9. Dimensions in m.

measured in 10 sections: 16 PT100 sensors, 8 for each deck, are devoted to cross sections C5 and C7, see Figure 2.6, whilst 6 PT100 sensors, 3 for each deck, are devoted to each of the remaining sections. The strategy consists in accurately measuring the temperature pattern in cross sections C5 and C7, and then obtaining the pattern in the remaining sections by using the temperatures provided by the 3 sensors as boundary conditions. Since the units that record data from the PT100 sensors can acquire measurements from 4 different sensors at most, 4 acquisition units are installed in cross sections C5 and C7, and 2, one for each deck, in the others. Each acquisition unit has an RJ-45 interface and is connected to an industrial PC by means of a TCP/IP protocol.

The total stations started acquiring data on June 9, 2014. Figure 2.7 shows the vertical

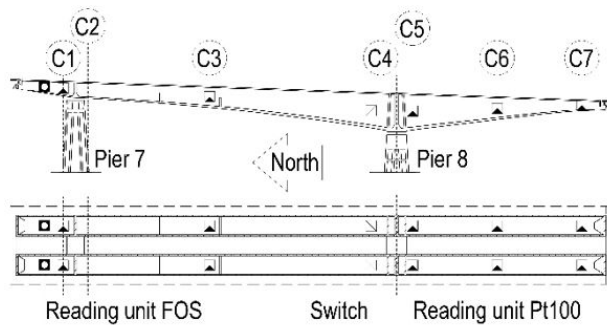


Figure 2.6: Configuration of FOSs and PT100 sensors.

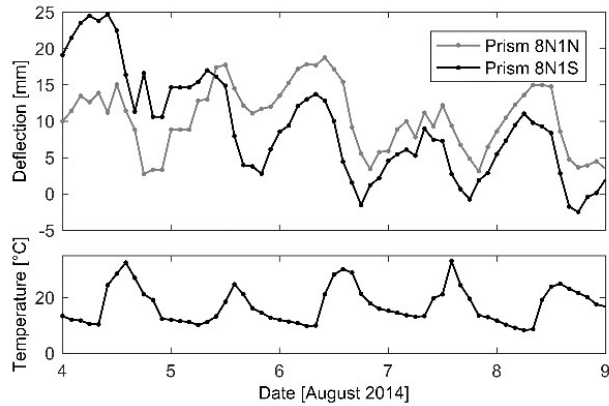


Figure 2.7: Time histories of deflection and temperature field data.

displacement of prisms 8N1N and 8N1S, along with the air temperature, recorded from August 4 to 9, 2014. These prisms are placed at the edge of the north girders, i.e. a location that is sensitive to variations in loads, temperature and mechanical properties. By observing these measurements, we can conclude that the behavior of the two decks before post-tensioning was similar, and mostly affected by temperature rather than live loads. Based on Figure 2.7, we can also argue that when the air temperature increases in the morning, the edge of each deck moves down, with a short time delay. This occurs because the source of heat, i.e. the sun, increases the temperature of the top slab more than that of the bottom slab, and so leads the top slab to elongate more than the bottom one.

In Figure 2.8, we show the instant effects of post-tensioning. The figure displays one measurement per day, acquired from 5 am to 7 am -when a measurement exists within this interval-. Three phenomena can be observed in Figure 2.8:

- from July 31 to August 11, 2014, part of the top slab belonging to the girder bearing the southbound carriageway was removed and new concrete was cast to the required thickness; this weakened the corresponding deck, leading it to behave differently from the girder bearing the northbound carriageway;
- from November 25 to December 3, 2014, the external cables installed in the girder

bearing the southbound carriageway were tensioned, causing the same deck to rise by about 70 mm;

- the behavior of the southbound deck after post-tensioning in 2014 was different from the other, as its deflection clearly increased more over time than that of the northbound carriageway.

In addition, Figure 2.8 also shows the influence of the environmental temperature. In particular, we can notice that whereas the measurements of Figure 2.7 are strongly influenced by the hourly effects of the sun, which causes the edge of the cantilever to lower, the deflection displayed in Figure 2.8 seems to increase with the temperature. The reason for this is that measurements shown in Figure 2.7 were recorded before sunrise, i.e. when the temperature of the two slabs should be about the same and close to the average temperature of the air in the early morning. Based on this reasonable assumption, a global increase in temperature of the structure increases the size of the whole viaduct, in particular of the piers, resulting in larger measurements of the edge deflection.

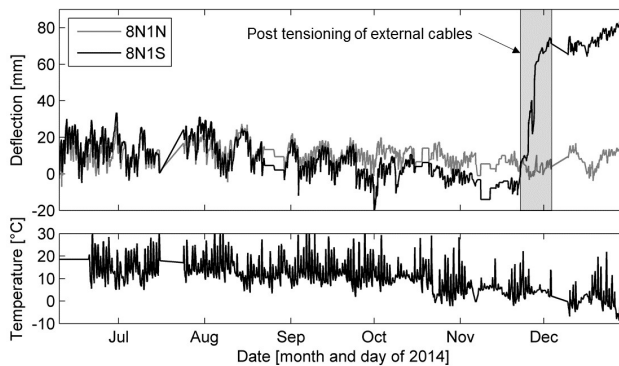


Figure 2.8: Measured deflection at prisms 8N1N and 8N1S and air temperature field data.

Finally, Figure 2.8 shows that the effect of every stage of the 2014 intervention was monitored with a good precision and that measurements agree well with first principles and engineering judgment.

## **2.4 FE modeling of the Colle Isarco viaduct**

A realistic FE model of the Colle Isarco viaduct may be useful not only for the investigation of the main causes of its past behavior, but also to estimate future deflections, to detect the effectiveness of the last intervention, and to provide a useful means for the development of a DSS, resulting in significant cost savings in future maintenance.

Therefore, in the sequel, we present two separate FE models. The first is a refined 3D model that we used to perform local analyses only; in fact, the run time required for analyses of the whole structure appeared to be excessive. The second is a simpler 1D model, based on the formulation presented in Section 2 and conceived to perform rapid and accurate creep analyses on the main box girders. To the best of authors knowledge, this is the first time that an energetic formulation for linear viscoelastic problems is developed and applied to a realistic structure subjected to such a complex loading history.

### **2.4.1 3D FE model**

We developed a 3D FE model of the Colle Isarco viaduct in ANSYS v. 12.1. The concrete structure of the viaduct was implemented using SOLID186 elements, whereas the 414 cables were modeled with 8059 BEAM188 Timoshenko beam elements, for a total of 260000 degrees of freedom (DoFs). With regard to the prestressing load, each cable was placed into the model at its proper longitudinal and transversal position, simulating the prestress friction losses by applying an equivalent thermal gradient between the two edges of each cable. The geometrical characteristics considered in the model reproduce the actual geometry of the viaduct, as well as the mechanical properties of materials. We summarize both geometrical and mechanical properties in Table 2.1 and Table 2.2, where  $2.38 \div 10.80$  m indicates that the cross-section depth varies from 2.38 m at section A of Figure 2.3(a) to 10.80 m at Pier #8 as well as for the lower slab thickness.

With regard to the constitutive law of Bazant, ANSYS allows users to redefine the mechanical constitutive behavior of materials through User Programmable Features (UPF).

Table 2.1: Geometrical characteristics.

<b>Cross section properties</b>	
Cross section depth	2.38 ÷ 10.80 m
Upper slab width	11.00 m
Lower slab width	6.00 m
Upper slab thickness	0.26 m
Lower slab thickness	0.12 ÷ 0.99 m
Lateral slab thickness	0.40 m

Table 2.2: Mechanical properties.

<b>Concrete</b>	
Compressive strength	45 MPa
Young's modulus	31043 MPa
Poisson's ratio	0.2
Density	2500 kg/m <sup>3</sup>
<b>Dywidag bars</b>	
Yield strength	850 MPa
Young's modulus	210000 MPa
Poisson's ratio	0.3
Density	7850 kg/m <sup>3</sup>

Thus, Model B3 was implemented in FORTRAN language as an external user-defined subroutine with two outputs: i) the incremental creep strain at the current time step; ii) the corresponding time derivative. According to Equations (2.2)-(2.4), these two strain quantities are functions of five parameters, which were estimated through a Bayesian analysis (Bolstad, 2010) and read:  $q_1 = 19.33\mu\epsilon$ ,  $q_2 = 129.93\mu\epsilon$ ,  $q_3 = 0.56\mu\epsilon$ ,  $q_4 = 10.09\mu\epsilon$  and  $q_5 = 19352.92\mu\epsilon \cdot \epsilon_{sh\ inf}$ .

Regardless of the constitutive law considered in the model, ANSYS can analyze creep

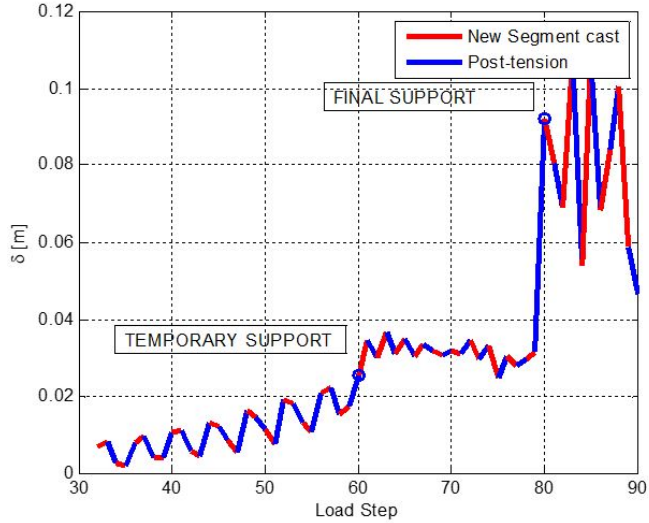


Figure 2.9: Phases of displacement evolution of upper point at cross section B of Figure 2.3(a) during construction estimated by a 3D FE simulation.

phenomena by means of two different integration methods.

The first is the explicit forward Euler method, whilst the second corresponds to the implicit backward Euler method. The explicit method is widely used in creep analysis because of simplicity, and its accuracy depends on the time-step size. Furthermore, it is conditionally stable, which means that its stability is restricted to small time steps. On the other hand, the implicit Euler method is numerically unconditionally stable, which implies that it does not require as small a time step as the explicit creep method, so it is much faster overall. However, the price for the unconditional stability is the need to solve non-linear equations at each time step. The computation of the creep strain,  $\varepsilon^{cr}$ , through the implicit integration method, i.e. the method selected for modeling the Colle Isarco viaduct, follows the algorithm summarized in Table 2.3 Therein, we use  $n$  to indicate the current time step,  $i$  the iteration step,  $\mathbf{D}$  the derivative operator,  $\mathbf{k}$  the stiffness operator, and  $\epsilon$  a tolerance vector.

As clearly shown in Table 2.3, the accuracy and effectiveness of the implicit method depend on both the chosen tolerance and the convergence ratio of the fixed point iterations.

A drawback that might occur in this type of analysis concerns the slow convergence of the fixed point iterations. Therefore, if the desired accuracy is not reached within 3-4 iterations, the time-step size will be decreased and calculations repeated starting from Step 1. For instance, in the case of the Colle Isarco viaduct model, due to the heavier deformation gradient occurring within the first few days after load application, we divided initial time steps into several small subintervals.

Table 2.3: Algorithm for the evaluation of creep strains implemented in the ANSYS software.

<b>Implicit creep method</b>
<p><b>Set</b> <math>i = 0</math>; <math>\boldsymbol{\varepsilon}_{n+1}^{cr^i} = \boldsymbol{\varepsilon}_n^{cr}</math>; <math>\boldsymbol{\sigma}_{n+1}^i = \boldsymbol{\sigma}_n</math>;</p> <p>1. Subroutine computes <math>\Delta\boldsymbol{\varepsilon}_n^{cr^i}</math>; <math>\boldsymbol{\varepsilon}_{n+1}^{cr^{i+1}} = \boldsymbol{\varepsilon}_n^{cr} + \Delta\boldsymbol{\varepsilon}_n^{cr^i}</math>;</p> <p><b>If</b> <math> \boldsymbol{\varepsilon}_{n+1}^{cr^{i+1}} - \boldsymbol{\varepsilon}_{n+1}^{cr^i}  &gt; \epsilon</math> <b>then</b></p> <p style="padding-left: 2em;">solve: <math>\mathbf{DkD}^T \mathbf{u}_{n+1}^{i+1} = -\mathbf{f} + \mathbf{Dk}\boldsymbol{\varepsilon}_{n+1}^{cr^{i+1}} + \mathbf{Dk}\boldsymbol{\varepsilon}_{n+1}^{th^{i+1}}</math>;</p> <p style="padding-left: 2em;">calculate: <math>\boldsymbol{\sigma}_{n+1}^{i+1} = \mathbf{k}(\mathbf{D}^T \mathbf{u}_{n+1}^{i+1} - \boldsymbol{\varepsilon}_{n+1}^{cr^{i+1}})</math>;</p> <p style="padding-left: 2em;">set <math>i = i + 1</math> and go to 1;</p> <p><b>else</b></p> <p style="padding-left: 2em;">set <math>\boldsymbol{\varepsilon}_{n+1}^{cr} = \boldsymbol{\varepsilon}_{n+1}^{cr^{i+1}}</math>;</p> <p><b>end</b></p>

The 3D model accounts for all variations in loading, geometry and boundary conditions. Furthermore, it can reproduce both bridge history and construction stages with optimal accuracy. For instance, Figure 2.9 shows the principal construction phases tracked by ANSYS in terms of deflection at cross section B, specified in Figure 2.3(a). In particular, the box girder deck was erected in alternate segments launched each side of Pier #8, known in the technical literature as balanced construction. As a result, after a new segment cast, indicated in red in the curve of Figure 2.9, the post tension followed,

whose deflection is depicted in blue, in the same curve. Then, because of the different lengths of the cantilever arm (59 m) and the back arm (91 m), the balanced construction required the erection of a temporary support at cross section C of Figure 2.3(a). After the construction of the back arm, the temporary support was removed, reaching its final configuration.

We employed the same 3D FE model to perform a creep analysis from 1969 to 2016; anyhow it did not lead to satisfactory results due to: i) the huge simulation time, more than 15 days with an 8-core machine -32 GB of RAM and 2.10 GHz of CPU frequency;- ii) the amount of memory required to complete the analysis. Given this computational burden, we mainly used the ANSYS model to perform 3D elastic analyses; moreover, the extent of local stresses at the anchorage blocks of the post-tensioning systems and at other critical parts of the structure were estimated.

#### **2.4.2 1D FE model**

Owing to the drawbacks of the 3D ANSYS model, the 1D model was then selected for non-linear simulations accounting for: i) the construction stages of the viaduct; ii) its geometry; iii) the prestress loadings; iv) the tension losses; v) and major maintenance work. Accordingly, we describe herein the main input data for the FE formulation anticipated in Subsection 2.2.2.

As depicted in Figure 2.10, we divided the box girder into 48 segments. Hence, 49 nodes, with three DoFs per node, characterize the 1D FE model, for a total number of 147 DoFs against the 260000 DoFs of the 3D model. In order to take into account the exact assembly of the segments and the change of constraint configuration, we redefine the geometric input data at each time step within the interval 0 days (start of construction on May 1969) to 731 days (end of construction on May 1971), with a time-step size equal to 1 day. After the construction end, the static configuration of the box girder was left unchanged. Thus as depicted in Figure 2.3(a), the final configuration of each single box girder consists of a roller at Pier #7 and a pin at Pier #8.

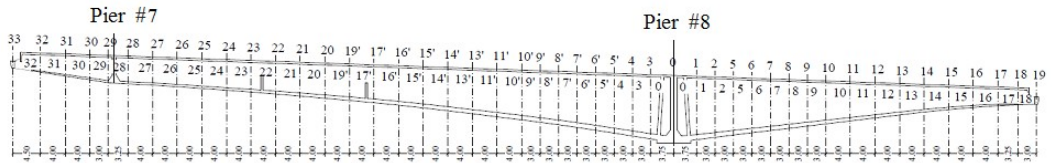


Figure 2.10: Discretization of the box girder under exam.

Other important input data provide information about the number of upper and lower pretensioning cables, the homogenized area, the homogenized moment of inertia, and the volume-to-surface ratio at each cross section of mesh; all assigned according to the technical reports of Autostrada del Brennero SpA. In detail, the area and moment of inertia are two fundamental quantities for the determination of the element stiffness operator  $\mathbf{k}^e$ , whereas the volume-to-surface ratio is utilized to compute the drying compliance of Model B3. All additional information useful for estimating the five parameters of Model B3 through Equations (2.5), i.e. cement content, aggregate content, water content, environmental relative humidity, and other mechanical properties of materials, are directly included into the MATLAB code. As previously discussed, we reassigned these geometric input data, i.e. number of cables, area, moment of inertia, and volume-to-surface ratio, at each time step within the first 731 days and during the last maintenance work in 2014. For instance, Table 2.4 collects geometric input data and information about the Model B3 parameters at Pier #8, where 'o' indicates the characteristics of the old concrete C35/45 and 'n' indicates the characteristics of the new layer of concrete C45/55 added at the top of the upper slab during the last maintenance work (2014). In addition, it is important to underline that we set the final values of Model B3 parameters through a proper calibration process; it was accomplished by varying the main quantities related to shrinkage phenomena, i.e. relative humidity and volume-to-surface ratio. Since they are taken into account by parameter  $q_5$ , it affected the most the creep response of the structure.

Both the dead loads and the prestress loads were assigned at each time step. A total of 1373 time steps were assigned until year 2040, in terms of bending moment  $M$  and

Table 2.4: Geometrical characteristics and Model B3 parameters of the cross section at Pier #8, where 'o' indicates the characteristics of old concrete and 'n' indicates the characteristics of the new layer of concrete.

<b>Characteristics of the cross section at Pier #8</b>	
Cross section depth	10.80 m
Upper slab width	11.00 m
Lower slab width	6.00 m
Upper slab thickness	0.26 m
New upper slab thickness	0.09 m
Lower slab thickness	0.99 m
Lateral slab thickness	0.40 m
Number of upper cables	260
Number of lower cables	0
Homogenized area	18.13 m <sup>2</sup>
Homogenized inertia	340.43 m <sup>4</sup>
Volume-to-surface ratio (o)	0.22 m
Volume-to-surface ratio (n)	0.09 m
$q_{1,o}$	19.33 $\mu\epsilon$
$q_{2,o}$	143.90 $\mu\epsilon$
$q_{3,o}$	1.07 $\mu\epsilon$
$q_{4,o}$	9.22 $\mu\epsilon$
$q_{5,o}$	323.47 $\mu\epsilon$
$q_{1,n}$	17.41 $\mu\epsilon$
$q_{2,n}$	101.43 $\mu\epsilon$
$q_{3,n}$	0.75 $\mu\epsilon$
$q_{4,n}$	6.99 $\mu\epsilon$
$q_{5,n}$	304.79 $\mu\epsilon$

concentrated force P. Table 2.5 reports the load history of the cross section at Pier #8 relative to the dates of main interventions. Moreover, in order to guarantee the compati-

Table 2.5: Load history at Pier #8 during main interventions.

Date	M[kN m]	P[kN]
15/05/1971	$-8.66 \cdot 10^5$	$1.09 \cdot 10^5$
15/03/1988	$-7.06 \cdot 10^5$	$9.94 \cdot 10^5$
24/11/2014	$-7.60 \cdot 10^5$	$9.64 \cdot 10^5$
04/10/2015	$-7.60 \cdot 10^5$	$1.40 \cdot 10^5$

bility of displacements between the old and new slab after the intervention of 2014, we considered a horizontal force applied at the interface. We evaluated this horizontal force by simply subtracting the increment of creep-shrinkage deformation of the new layer to the increment of creep-shrinkage deformation of the old upper slab; then, we multiplied this difference by the Young's modulus and the cross section area of the new layer.

### 2.4.3 1D model validation and prediction

In this section, we discuss the validation of the 1D FE formulation through comparison between field data and the simulated time-deflection profile. Moreover, we also present the prediction made by the 1D model.

With regard to model validation, Figure 2.11 depicts the deflection trend at cross section A of Figure 2.3(a), from the construction of the viaduct in 1969 up to 2016. The first part of the simulation curve is characterized by a slope very similar to the one acquired by dumpy level measurements. We can also observe a high level of accuracy in reproducing the elastic recoveries during the two maintenance interventions, in 1988 and 2014, respectively. A slight deviation between field data and the FE model occurs from 1989 to 1996; however, this mismatch vanishes a few years after 1996. Overall, we estimated a RMSE equal to 5.7 % between the results of 1D FE model and measured field data. Therefore, it is evident that the proposed FE model can capture the past behavior of the viaduct with a favorable accuracy.

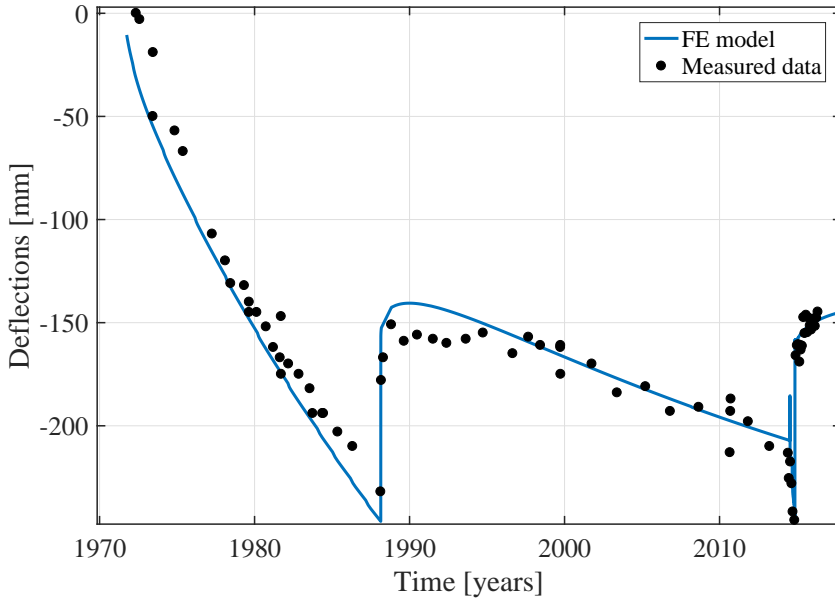


Figure 2.11: Comparison between 1D FE model predictions and field data of time-deflection profile relevant to cross section A of Figure 2.3(a).

The comparison between field and model data during the last maintenance work can be better appreciated in Figure 2.12; more precisely, deflection values decrease in sign before the post-tensioning of November 2014 and increase afterwards, at a rate of 7 mm/year from December 2014 to September 2016. Obviously, this deflection increase will reduce over the years due to both tension losses and reduction in the differential shrinkage between top and bottom slabs. As a result, the 1D FE model predicts a horizontal configuration of cross-section A around November 2025 with a limited decrease up to 2040. The relevant FE analysis from 1969 to 2040 requires 8 hours, with an 8-core desktop machine, 32 GB of RAM and 2.10 GHz of CPU frequency.

It is then evident that the 1D model requires a lower computational effort than the model involved in the ANSYS 3D analysis, briefly described in Subsection 2.4.1. The relevant main reasons are: i) the reduced number of DoFs; ii) the integration method used to compute creep strains; and iii) the time-step size required for the analysis. In

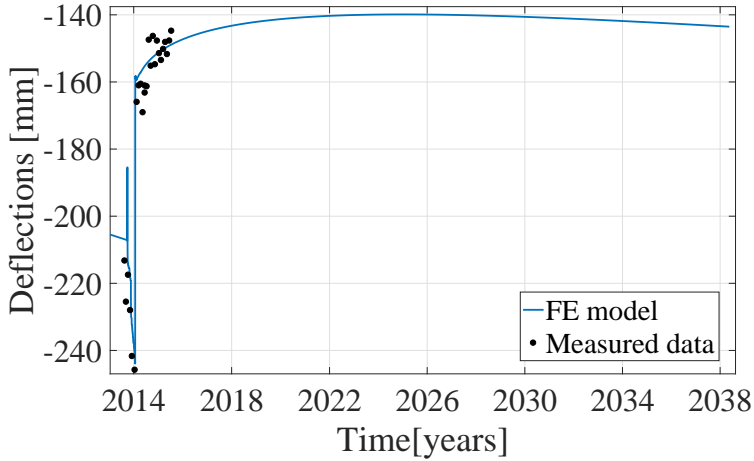


Figure 2.12: Deflection effects after the intervention of 2014 and prediction until 2040 relevant to cross section A of Figure 2.3(a).

fact, as most of commercial software, ANSYS software evaluates the creep strain  $\varepsilon_n^{cr}$  through the backward Euler method performing an iteration process at each time step  $n$ , as summarized in Table 2.3. On the other hand, no iteration process is required in the proposed 1D formulation, mainly because of the linearity of the problem and the update of both  $\mathbf{L}$  and  $\mathbf{g}$ , see Equation (2.14), at each time step. In addition, the 1D formulation allows for the use of larger time steps than the backward Euler method, guaranteeing accurate results nonetheless. Another limitation of the backward Euler method regards its accuracy, which depends on the time-step and the convergence ratio of the fixed point iterations. Conversely, the accuracy of the 1D FE formulation also depends on the order of the chosen time shape functions collected in  $\mathbf{M}(t)$  of Equation (2.10). In other words, if we perform 1D and 3D analyses with the same time-step size, the choice of higher order shape functions in the 1D model can guarantee a better accuracy. Moreover, the presented 1D FE model, implemented in MATLAB and based on the energetic formulation presented in Subsection 2.2.2 seems to be particularly effective for the simulation of the Colle Isarco viaduct, including its history. Notwithstanding that, the proposed model neglects shear deformations, which is acceptable considering the slenderness of the structure, i.e.

the incidence of bending deformations.

## 2.5 Development of a decision support system

In this section, we propose a general scheme of DSS for the Colle Isarco viaduct, in which information coming from the 1D FE model are also involved. As depicted in Figure 2.13, the proposed DSS consists of two main parts: i) Bayesian logic (Sivia and Skilling, 2006; Bolstad, 2010; Han et al., 2017) to compute probabilities of structural states that may occur; and ii) axiomatic Expected Utility Theory (EUT) (Schlaifer and Raiffa, 1961; Von Neumann and Morgenstern, 2007) to identify economically optimal choices. To the best of authors' knowledge, no DSS based on EUT has yet been proposed for everyday use in the field of civil engineering. Indeed, a recent publication by Faber and Maes (2008) pointed out a number of issues arising when optimal decision-making has to be implemented in real-life settings for management of structures and infrastructures. Conversely, DSSs already operational in the real life can be found in fields of medicine and finance (Mussi, 2004; Sauter, 2014), as the probabilities of different scenarios and the financial consequences can be easily assessed.

The DDS proposed herein takes as inputs four variables:

- The most recent SHM measurements,  $\mathbf{y}$ , which, in our case, are the displacements from the total stations, the strains from the FOSs and the temperatures from the PT100 sensors;
- the prior probability  $\rho(\boldsymbol{\theta})$  of the parameters  $\boldsymbol{\theta}$  that define the structural state, i.e. Young's modulus of concrete, initial prestress and relative humidity;
- the prior probability  $\rho(S)$  of possible structural conditions, i.e. 'pristine' and 'damaged';
- iv. the costs  $\mathbf{C}$  corresponding to each possible event, i.e. costs of using a damaged structure -including indirect costs- and costs of inspection.

The DSS contains a Bayesian inference module and a decision-analysis module. In order to calculate the probability  $\rho(S|\mathbf{y})$  of each possible state of the viaduct, given the updated

observations  $y$ , the former module implements a numerical Bayesian inference such as the Metropolis-Hastings algorithm (Cappello et al., 2015) and Monte Carlo importance sampling (Evans and Swartz, 1995). In order to identify the economically optimal choice  $a_{opt}$  for the detected structural behavior, the decision-analysis module takes into account costs  $C$  (Cappello et al., 2016). Typical choices to be considered are: 'do nothing', 'close the bridge' and 'send an inspector'. The optimal action  $a_{opt}$  corresponds to the maximum expected utility, calculated by applying the EUT axioms.

In this framework, the 1D FE model proposed in Subsection 2.4.2 is used to train the Bayesian inference module depicted in Figure 2.13. The objective of the Bayesian module is to identify which structural condition  $S$  - 'pristine' or 'damaged' - agrees with the measurements best; therefore, it must contain the response predicted by the FE model in both conditions. During training, the structural behavior is simulated using the FE model for different realizations of structural condition  $S$  and for different realizations of state parameters  $\theta$ . The need to perform a number of simulations that is significant from a statistical viewpoint made it necessary to develop an extremely efficient structural model. Straub (2014) estimated that  $10^2$  to  $10^3$  simulations are required to accurately calculate structural reliability. Relevant simulation results are stored in a lookup table, which provides the structural response of the viaduct for the realizations of  $S$  and  $\theta$  not considered during training. The use of a lookup table reduces the execution time of the Bayesian inference algorithm within the DSS, and therefore, expedites the identification of the optimal action  $a_{opt}$  that is recommended to the bridge manager.

## 2.6 Conclusions and future perspectives

In this paper, we have presented the conception and development of effective FE-based tools to model, in general, segmental prestressed concrete box girders susceptible to creep and, in particular, the significant Colle Isarco viaduct. We have also shown the recordings from the structural health monitoring system recently installed on the viaduct, thus highlighting its key role in both model validation and interpretation of the structural

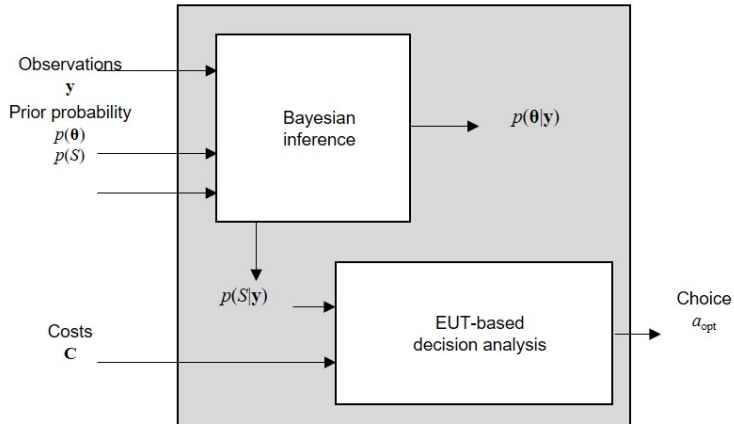


Figure 2.13: The architecture of the decision support system.

behavior of the viaduct.

Two different FE models of the Colle Isarco viaduct were presented, both based on the creep constitutive law proposed by Bazant and co-workers. The first is a 3D FE model developed in a commercial software, utilized to perform elastic analyses only, due to the excessive simulation time required to perform creep analyses. The second is a 1D FE model conceived through an energetic formulation for linear viscoelastic problems, used to estimate the deflection trend at the tip of the longest cantilever, from viaduct construction in 1969 up to 2040. Unlike the 3D FE model, the 1D FE formulation relies on an extension of the classical total potential energy and is particularly convenient for accomplishing creep analyses mainly due to its reduced run time. Furthermore, it simulates the past behavior of the viaduct with a good level of accuracy and provides a satisfactory prediction of its long-term behavior up to 2040, with a clear change in the deflection trend at the end of 2025. The results of the 1D FE model were validated using both field data from the old dumpy level acquisition method until 2013 and from the new structural health monitoring system, afterwards. Moreover, the structural health monitoring system not only provides accurate and reliable data for validation of the proposed 1D FE model, but also successfully records the response of the viaduct during

the last maintenance work in 2014.

The obvious exploitation of both the 1D FE model and monitoring field data, presented above as an effective tool for future risk estimation and viaduct management, is their use into the context of Bayesian inference for the implementation of an efficient decision support system. Finally, further run time savings can be achieved in the 1D FE model by parallelizing the algorithm solution for different load applications and by replacing the 5-parameter Bazant model creep constitutive law with three parameters fractional-based real-order operators.

## 2.A Pseudocode for the FE formulation

In this appendix, we summarize the FE viscoelastic formulation presented in Subsection 2.2.2 by means of the following pseudocode.

`%-----`

`-`

### **INPUTs**

**nodes** = coordinates of each mesh node;

**elements** = mechanical and geometrical properties of elements;

**loads** = load applied at each mesh node;

$t_0$  = initial time instant;

$t_f$  = final time instant;

`%-----`

### **Initialize:**

$\mathbf{k}_{gl}$  = global stiffness operator;

$\mathbf{f}$  = global load vector;

$\mathbf{L}$  = extended stiffness operator;

$\mathbf{g}$  = extended vector of equivalent nodal forces;

**for**  $i=1:nel$  `% loop over elements`

**compute** the element stiffness operator  $\mathbf{k}_{el}$ ;

**assemble** into global stiffness operator  $\mathbf{k}_{gl}$ ;

**end**

**set**  $GE \rightarrow$  number of Gauss points for external integration;

**choose** coordinates  $t$  and weights  $w$  within the time interval  $[t_0, t_f]$ ;

**for**  $j=1:GE$

```

initialize  $\mathbf{H}_{gl}$ ;
for i=1:nel
    compute:
         $R_{B3}(t(j), t_0)$ ;
         $M(t_0)$ ;
         $\mathbf{G} = (G_{B3}(t(j), t_0)/G_{B3}(t_0, t_0)) * M(t_0)$ ;
    set GI  $\rightarrow$  number of Gauss points for internal integration;
    choose coordinates tt and weights ww within the time interval  $[t(j), t_0]$ ;

    for x=1:GI
        compute:
             $G_{B3}(t(j), tt(x))$ ;
             $dM \rightarrow$  derivative vector;
             $\mathbf{G} = \mathbf{G} + ww(x) * (G_{B3}(t(j), tt(x))/G_{B3}(t_0, t_0)) * dM$ ;
    end

    compute the element relaxation operator  $\mathbf{H}_{el}$ ;
    assemble into global relaxation operator  $\mathbf{H}_{gl}$ ;
end

 $\mathbf{g} = \mathbf{g} + w(j) * (\mathbf{H}_{gl})' * (\mathbf{k}_{gl} \setminus \mathbf{f})$ ;
 $\mathbf{L} = \mathbf{L} + w(j) * (\mathbf{H}_{gl})' * (\mathbf{k}_{gl} \setminus \mathbf{H}_{gl})$ ;
end

```

**compute** the time DoFs vector  $\beta = \mathbf{L} \setminus \mathbf{g}$ ;

%-----

## OUTPUT

$\alpha$  = DoFs vector of the assembled structure;

%-----

## Chapter 3

### **A fractional-order model for aging materials: An application to concrete**

*by Angela Beltempo, Massimiliano Zingales, Oreste S. Bursi, and Luca Deseri*

#### **Abstract**

In this paper, the hereditariness of aging materials is modeled within the framework of fractional calculus of variable order. A relevant application is made for the long-term behavior of concrete, for which the creep function is evaluated with the aid of Model B3. The corresponding relaxation function is derived through the Volterra iterated kernels and a comparison with the numerically-obtained relaxation function of Model B3 is also reported. The proposed fractional hereditary aging model (FHAM) for concretes leads to a relaxation function that fully agrees with the well-established Model B3. Furthermore, the FHAM takes full advantage of the formalism of fractional-order calculus to yield semi-analytic expressions in terms of material parameters.

**Keywords:** variable-order fractional calculus; fractional aging concrete; concrete relaxation; concrete creep; RILEM database; fractional hereditary aging materials..

### 3.1 Introduction

The study of the time-dependent behavior of materials is a crucial issue in structural engineering. Such a feature is often encountered since one of the main assumptions of the structural analysis, i.e. the elasticity of materials, is not fulfilled in nature. Indeed, real-type materials show a mechanical behavior in terms of strain/stress that depends on the previously experienced stress/strain histories, and this behavior is usually observed by means of creep and relaxation tests (Flügge, 2013). Both phenomena, i.e. creep and relaxation, are exhibited by several materials, like rubbers, polymers, collagens, concretes, but over different durations, i.e. some hours for polymers, a few minutes for collagen structures, and many years for concretes.

In the context of linear viscoelasticity, the most common approach used to describe the mechanical behavior of materials consists in providing the so-called rheological models (Drozdov, 1998), where each model element represents a basic feature of the material, e.g. the spring indicates the elastic response, the dashpot describes the viscous response, and so on. Hence, the time-dependent behavior of materials is illustrated by a specific arrangement of the aforementioned elements, like the well-known Kelvin-Voigt, Maxwell, and Zener models. Furthermore, this approach leads to a time-dependent behavior expressed as a linear combination of exponential functions, which are characterized by parameters obtained through a best-fitting procedure with experimental data (Christensen, 2012). However, the major drawback of using exponential functions is that the obtained time-dependent model often yields negative values of the relevant physical parameters that, instead, must be intrinsically positive. This problem was solved at the middle of the last century by introducing the so-called spring-pot element (Blair, 1949), which is a two-parameters element that can be reverted to a spring or to a viscous element by assigning specific values to the relevant parameters (Mainardi, 1997). In a greater detail, the time-dependent behavior of the spring-pot corresponds to a power law characterized by a real exponent  $0 \leq \beta < 1$  and a dimensional-force constant.

Power laws describe in an excellent way the time-dependent behavior of polymers

(Nutting, 1921; Gemant, 1938), biocomposites (Cataldo et al., 2015), and biological tissues (Deseri et al., 2013; Magin et al., 2013). In addition, the use of power laws in combination with the linear superposition theorem (Boltzmann, 1878; Volterra, 1959) leads to the description of the mechanical behavior of several materials by the so-called fractional order integrals and derivatives (Mainardi, 2010; Podlubny, 1998). Basically, these operators represent the generalization of the classical integer-order operators to the case of the real-order differentiation/integration. Another important aspect of fractional-order operators is that they are mathematically well defined (Samko et al., 1987); moreover, they can be defined as a non-euclidean measure of Sobolev spaces (Bongiorno, 2004). Some relationships between the order of differentiation/integration and the topological dimension of the underlying set were also provided (Alaimo and Zingales, 2015; Butera and Di Paola, 2015; Bongiorno and Corrao, 2015a,b).

Fractional-order calculus was also introduced to capture the time-dependent behavior of non-aging concrete beams (Di Paola and Granata, 2016). However, since the mechanical properties of concrete significantly change after many decades from its casting, for an accurate prediction of the long-term behavior of this material, the aging phenomenon cannot be neglected.

The study of the time-dependent phenomena exhibited by concrete structures represents one of the most challenging issue in the field of linear viscoelasticity; indeed, the time-dependent behavior of concrete is influenced by several factors, such as shrinkage, drying, temperature, humidity, pore sizes (Bažant and Prasannan, 1989), and additional long-term effects involved in presence of prestress (Bažant et al., 2012; Deseri et al., 2014b; Beltempo et al., 2018). Thus, a precise prediction of the concrete time-dependent behavior is still a matter of debate among researchers (Goel et al., 2007). As a consequence, technical codes propose different models on this matter, which find their experimental bases on the RILEM database for data of concrete specimens and structures (Bažant and Li, 2008; RILEM, 2016). The theoretical assumptions are instead borrowed from the so-called Model B3 (Bažant and Baweja, 2000), which consists of five parameters, mainly expressed as functions of the cement content, the age when drying begins, the material

strength, the environmental conditions, and the geometrical properties. Furthermore, Model B3 accounts for creep and drying simultaneously that represents a crucial aspect for a correct prediction of the material long-term behavior, and several contributions have been provided in the relevant scientific literature (Pickett, 1942; Bažant et al., 1997). In some simplified approaches the so-called aging coefficient is introduced, such as the Age-Adjusted Effective Modulus method (AAEM), which is widely used by researchers and practitioners due to its satisfactory results (Bažant, 1972; Bažant and Kim, 1979). However, the main drawback related to approximate approaches, like the AAEM, is the lack of thermodynamical consistency: in particular, no relations between stiffness and compliance exist. In this regard, a possible approach to relate aging-dependent creep and relaxation was presented in Bažant et al. (2013) by resorting to approximate formulations and reducing the functional class of the aging relaxation. The proposed relaxation function, however, is not related to the relevant creep function through the fundamental relationship of linear viscoelasticity (Flügge, 2013). Hence, the mathematical consistency of the approach in Bažant et al. (2013) is not guaranteed.

In this paper, a constitutive model within the framework of fractional calculus is proposed, which turns out to be thermodynamically and mathematically consistent. In other words, the obtained material response can uniquely describe both creep and relaxation phenomena and satisfies the fundamental Volterra's relationship of linear viscoelasticity. Moreover, the proposed constitutive model is conceived for any aging material and, since the constitutive behavior of concrete is quite complex among such solids, it is here applied to the study of the long-term response of concrete. More precisely, we introduce a specific form of material aging by means of a three-parameter model, which corresponds to a viscoelastic model characterized by fractional operators of variable order (Lorenzo and Hartley, 2002). The aging functions of the model are derived for concretes through a best-fitting procedure with the RILEM database data. The obtained creep and relaxation functions fully comply with the aforementioned mathematical and thermodynamical consistencies and are compared against the five-parameters Model B3 functions, thereby resulting in an effective model for the description of the time-dependent behavior of aging

materials.

This paper is organized as follows: we report some general definitions of material aging hereditariness in Section 3.2; in Section 3.3, we introduce the fractional-order aging hereditariness; and, in Section 3.4, we propose a fractional-hereditary aging model (FHAM) with a relevant application to concrete structures. Main conclusions are summarized in Section 3.5 with further developments.

### 3.2 Preliminary remarks on material aging hereditariness

The constitutive behavior of materials in long-standing mechanical tests is described by means of the well-known creep and relaxation functions, dubbed  $J(t)$  and  $G(t)$ , respectively. The linear superposition applied to a generic stress/strain history, namely  $\sigma(\tau)$  and  $\varepsilon(\tau)$  with  $\tau \leq t$ , yields,

$$\varepsilon(t) = \int_0^t J(t - \tau) \cdot d\sigma(\tau) = \int_0^t J(t - \tau) \cdot \dot{\sigma}(\tau) d\tau \quad (3.1a)$$

$$\sigma(t) = \int_0^t G(t - \tau) \cdot d\varepsilon(\tau) = \int_0^t G(t - \tau) \cdot \dot{\varepsilon}(\tau) d\tau. \quad (3.1b)$$

Both expressions indicate the Boltzman superposition, where with the following notation  $\dot{f}(t) = df(t)/dt$  we denote the increment of the generic function  $f(t)$  and, in the case under investigation (3.1), the increment of the history of stress  $\sigma(t)$  and strain  $\varepsilon(t)$ .

The convolution integrals in Equations (3.1) are completely described as we introduce the functional class of creep and relaxation functions with the aid of experimental data. Creep and relaxation functions characterize the material behavior and they must satisfy the conjugation relation  $\hat{J}(s)\hat{G}(s) = 1/s^2$ , where  $s$  indicates the Laplace parameter and  $[\hat{f}(s)] = \mathcal{L}[f(t)]$  the Laplace transform of the generic function  $f(t)$ .

However, Equations (3.1) refer to hereditary materials, which do not show any degradation/improvement of their mechanical characteristics during their service life. Thus, the behavior of hereditary materials only depends on the loading duration,  $(t - t_0)$ , but does not depend on the material age, when the constant stress/strain is applied,  $t_0$ . Conversely, several materials, like structural concretes, rubbers and polymers under photo-degradation,

show a significant change of their mechanical properties over time. In such a context, i.e. aging-dependent materials, the structural behavior depends on both the material age,  $t_0$ , when a stress/strain history begins, and the time occurred from the stress/strain application,  $(t - t_0)$ . This composed behavior is defined in literature as the aging hereditariness of materials (Jirásek and Bazant, 2002) and, under the assumption of the linear superposition, it may be characterized by the so-called creep function,  $J_c(t, t_0)$ , as well as by the relaxation function,  $G_s(t, t_0)$ . The creep function represents the strain undergone by the specimen due to an unitary stress applied at the time instant  $t_0$ , i.e.  $\sigma(t_0) = 1$ . Furthermore,  $J_c(t, t_0)$  is a function of two separate variables,  $t$  and  $t_0$ , with  $t \geq t_0$ . A similar consideration holds true for the relaxation function, which measures the stress at the generic time instant  $t$  due to an applied unitary strain at  $t_0$ ,  $\varepsilon(t_0) = 1$ , with  $t \geq t_0$ .

The constitutive equations for aging materials read,

$$\varepsilon(t) = \int_0^t J_c(t, \tau) \cdot d\sigma(\tau) = \int_0^t J_c(t, \tau) \cdot \dot{\sigma}(\tau) d\tau \quad (3.2a)$$

$$\sigma(t) = \int_0^t G_s(t, \tau) \cdot d\varepsilon(\tau) = \int_0^t G_s(t, \tau) \cdot \dot{\varepsilon}(\tau) d\tau, \quad (3.2b)$$

where we assume that both stress (3.2a) and strain (3.2b) histories are sufficiently smooth functions so that the Stieltjes integrals in (3.2) revert to the standard Riemann integrals in terms of functions  $\dot{\sigma}(t)$  and  $\dot{\varepsilon}(t)$ .

Creep-compliance and stiffness-relaxation functions are related by means of (3.2), yielding the first theorem of the linear aging hereditariness (Bažant, 1972) as,

$$J_c(t, t_0)G_s(t_0, t_0) + \int_{t_0}^t J_c(t, \tau) \frac{\partial G_s(\tau, t_0)}{\partial \tau} d\tau = 1. \quad (3.3)$$

This latter relationship is a Volterra integral equation of the second kind for the creep function  $J_c(t, t_0)$ . More precisely, Equation (3.3) yields the creep function as we measured the relaxation function,  $G_s(t, t_0)$ , for different couples of time instants  $(t, t_0)$ . However, the knowledge of the relaxation function is not so common in structural engineering, since the relaxation function should be obtained through field experiments on existing structures.

On the other hand, field measures allow for the estimation of the creep function,  $J_c(t, t_0)$ , so that the corresponding relaxation function,  $G_s(t, t_0)$ , can be obtained from the second theorem of the linear aging hereditariness as,

$$G_s(t, t_0)J_c(t_0, t_0) + \int_{t_0}^t G_s(t, \tau) \frac{\partial J_c(\tau, t_0)}{\partial \tau} d\tau = 1. \quad (3.4)$$

This represents a Volterra integral equation of the second kind for the relaxation function, as we specify the time instant  $t_0$  corresponding to the application of the strain history  $\varepsilon(t) = U(t - t_0)$ , with  $U(\cdot)$  the unit-step function.

In order to obtain an analytical expression of the relaxation function, we solve Equation (3.4) by means of the iterated-kernels method (Tricomi, 1957), yielding the following sequence,

$$G_s^{(1)}(t, t_0) = \frac{1}{J_c(t_0, t_0)}, \quad (3.5a)$$

$$G_s^{(2)}(t, t_0) = \frac{1}{J_c(t_0, t_0)} \left( 1 - \int_{t_0}^t \frac{\partial J_c(\tau, t_0)}{\partial \tau} G_s^{(1)}(t, \tau) d\tau \right), \quad (3.5b)$$

.....

$$G_s^{(k)}(t, t_0) = \frac{1}{J_c(t_0, t_0)} \left( 1 - \int_{t_0}^t \frac{\partial J_c(\tau, t_0)}{\partial \tau} G_s^{(k-1)}(t, \tau) d\tau \right), \quad (3.5c)$$

.....

In passing, we observe that both the first and second theorem of the linear aging hereditariness revert to the well-known equation in the Laplace domain, i.e.  $\hat{J}(s)\hat{G}(s) = 1/s^2$ , as hereditary materials are considered,  $J_c(t, t_0) = J(t - t_0)$  and  $G_s(t, t_0) = G(t - t_0)$ .

### 3.3 The fractional-hereditary aging materials

The study of the aging hereditariness of materials is highly influenced by the choice of the creep function,  $J_c(t, t_0)$ , as well as the choice of the relaxation function,  $G_s(t, t_0)$ , as shown in Equations (3.2a) and (3.2b).

In the context of the non-aging hereditariness of materials, a power-law representation of creep and relaxation functions, i.e.  $J(t)$  and  $G(t)$ , were introduced at the beginning of

the last century (Nutting, 1921),

$$J(t) = \frac{1}{C_\beta \Gamma(\beta + 1)} t^\beta \quad (3.6a)$$

$$G(t) = \frac{C_\beta}{\Gamma(1 - \beta)} t^{-\beta}, \quad (3.6b)$$

where  $\Gamma(\cdot)$  is the well-known Euler-Gamma function,  $0 \leq \beta < 1$  and  $C_\beta$ , a positive real number, are material parameters that may be estimated through a best-fitting procedure with experimental data (Di Paola et al., 2011; Mino et al., 2016). Straightforward manipulations show that the power-law functional class chosen for the definition of both creep and relaxation functions, as in Equations (3.6), satisfies the conjugation relation. By substituting Equations (3.6) into (3.1) we obtain,

$$\begin{aligned} \varepsilon(t) &= \frac{1}{C_\beta \Gamma(\beta + 1)} \int_0^t (t - \tau)^\beta \dot{\sigma}(\tau) d\tau = \frac{1}{C_\beta \Gamma(\beta)} \int_0^t (t - \tau)^{\beta-1} \sigma(\tau) d\tau = \\ &= \frac{1}{C_\beta} \left( I_{0+}^\beta \sigma \right) (t) = \left( I_{0+}^\beta \tilde{\varepsilon} \right) (t) \end{aligned} \quad (3.7a)$$

$$\sigma(t) = \frac{C_\beta}{\Gamma(1 - \beta)} \int_0^t (t - \tau)^{-\beta} \dot{\varepsilon}(\tau) d\tau = C_\beta \left( D_{0+}^\beta \varepsilon \right) (t) = \left( D_{0+}^\beta \tilde{\sigma} \right) (t) \quad (3.7b)$$

that represent the generalization of the well-known Riemann integral and Leibniz derivative of non-integer orders (Podlubny, 1998). Moreover,  $\tilde{\varepsilon}(t) = \sigma(t)/C_\beta$  and  $\tilde{\sigma}(t) = \varepsilon(t)C_\beta$  are sets of instantaneous values of strain and stress, involved in the absence of the material hereditariness.

The use of power laws and, as a consequence, of fractional-order operators is usually referred, in a rheological context, to the spring-pot element. The spring-pot is a one-dimensional element that is defined by means of two parameters, i.e.  $C_\beta$  and  $\beta$ , with  $C_\beta$  a positive real number and  $0 \leq \beta < 1$ , where  $\beta$  is representative of the differentiation order. More precisely, a simple spring corresponds to  $\beta = 0$  and  $\frac{d^\beta f}{dt^\beta} = \frac{d^0 f}{dt^0} = f$ ; whilst, case of  $\beta = 1$  corresponds to a first order derivative, i.e.  $\frac{d^\beta f}{dt^\beta} = \frac{df}{dt} = f'$ , which is a Newtonian rheological element. The three cases of a spring, a spring-pot and a Newtonian element are depicted in Figure 3.1, where  $E_c$  indicates the Young's modulus and  $\mu$  the viscous coefficient.

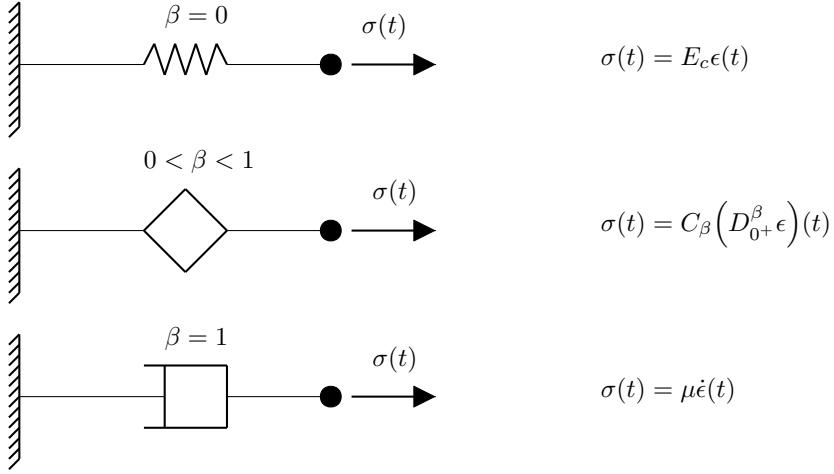


Figure 3.1: Representation of a spring element  $\beta = 0$ , a spring-pot element  $0 < \beta < 1$ , and a Newtonian element  $\beta = 1$ .

The fractional-order hereditariness of materials has been related to appropriate mechanical models (Di Paola and Zingales, 2012; Di Paola et al., 2013b; Deseri et al., 2014a), as well as to the fractal distribution of the material microstructure (Deseri et al., 2013). Despite of the fractional-calculus success in describing the constitutive behavior of hereditary materials (Deseri et al., 2014b), the presence of the material aging has never been accounted for.

In order to fill this gap, we assume that the material aging is described through the variation over time of the coefficients  $C_\beta \rightarrow C_\beta(t_0)$  and  $\beta \rightarrow \beta(t_0)$ . In this setting, we assume that the creep function is expressed as,

$$J_c(t, t_0) = \frac{(t - t_0)^{\beta(t_0)}}{C_\beta(t_0)\Gamma(\beta(t_0) + 1)} \quad (3.8)$$

and by substituting (3.8) into Equation (3.2a) we obtain,

$$\begin{aligned}
\varepsilon(t) &= \int_0^t \frac{(t-\tau)^{\beta(\tau)}}{C_\beta(\tau)\Gamma(\beta(\tau)+1)} \dot{\sigma}(\tau) d\tau = \\
&= \int_0^t \frac{(t-\tau)^{\beta(\tau)}}{\Gamma(\beta(\tau)+1)} \dot{\tilde{\varepsilon}}(\tau) d\tau + \int_0^t \frac{(t-\tau)^{\beta(\tau)}}{\Gamma(\beta(\tau)+1)} \frac{\dot{C}_\beta(\tau)}{C_\beta(\tau)} \tilde{\varepsilon}(\tau) d\tau = \\
&= - \int_0^t \left[ \frac{(t-\tau)^{\beta(\tau)}}{\Gamma(\beta(\tau)+1)^2} \left( \ln(t-\tau)\Gamma(1+\beta(\tau)) - \Gamma'(1+\beta(\tau)) \right) \right] \tilde{\varepsilon}(\tau) d\tau + \\
&\quad + \int_0^t \left[ \frac{(t-\tau)^{\beta(\tau)-1}}{\Gamma(\beta(\tau))} + \frac{(t-\tau)^{\beta(\tau)}}{\Gamma(\beta(\tau)+1)} \frac{\dot{C}_\beta(\tau)}{C_\beta(\tau)} \right] \tilde{\varepsilon}(\tau) d\tau = \left( \mathbb{I}_{0^+}^{\beta(t)} \tilde{\varepsilon} \right) (t) + \tilde{\varepsilon}_r(t),
\end{aligned} \tag{3.9}$$

where we use the usual chain rule of differentiation and we introduce a rate-dependent field  $\tilde{\varepsilon}_r(t)$ , described by the latter term in Equation (3.9). The first term in Equation (3.9) is the Riemann-Liouville fractional integral of order  $\beta = \beta(\tau)$  (Lorenzo and Hartley, 2002; Valério and Da Costa, 2011), as reported in Appendix 3.B. Incidentally, we observe that, as we assign constant values to  $\beta$  and  $C_\beta$ , the well-know fractional hereditary model is obtained as in Equation (3.6a).

The relaxation function corresponding to the presented fractional-order creep function (3.8) is provided by the iterated-kernels method (3.5).

A constitutive equation, formally similar to (3.9), may also be provided by assuming that the fractional-hereditary aging material is characterized by a relaxation function with the following form,

$$G_s(t, t_0) = \frac{(t-t_0)^{-\beta(t_0)}}{\Gamma(\beta(t_0))} C_\beta(t_0). \tag{3.10}$$

The latter yields the following expression of the stress,

$$\begin{aligned}
\sigma(t) &= \int_0^t \frac{(t-\tau)^{-\beta(\tau)}}{\Gamma(\beta(\tau))} C_\beta(\tau) \dot{\varepsilon}(\tau) d\tau = \int_0^t \frac{(t-\tau)^{-\beta(\tau)}}{\Gamma(\beta(\tau))} \dot{\tilde{\sigma}}(\tau) d\tau + \\
&\quad - \int_0^t \frac{(t-\tau)^{-\beta(\tau)}}{\Gamma(\beta(\tau))} \frac{\dot{C}_\beta(\tau)}{C_\beta(\tau)} \tilde{\sigma}(\tau) d\tau = \left( \mathbb{D}_{0^+}^{\beta(t)} \tilde{\sigma} \right) (t) - \tilde{\sigma}_r(t),
\end{aligned} \tag{3.11}$$

where the additional contribution relevant to the evaluation of the material parameters up to the time instant  $t$  is actually involved.

In the next section, variable-order fractional calculus is used to deal with the aging hereditariness of concrete by means of a three-parameters model.

### 3.4 The fractional-aging hereditariness of concrete

In this section, we aim to formulate a constitutive model for the aging hereditariness of concrete within the formalism of the fractional-order calculus presented in Section 3.3. In this regard, we observe that a fractional-order constitutive model for the hereditariness of concrete was recently proposed by Di Paola and Granata (2016). It was shown, indeed, that, for fixed values of the aging time  $t_0$ , a precise representation of the creep function and the relaxation function is achieved by means of power laws as  $t^\beta$  and  $t^{-\beta}$ , respectively.

In order to derive the Fractional-Hereditary Aging Model (FHAM), we first present Model B3, one of the most widely used viscoelastic models for prestressed concrete structures. Then, in Subsection 3.4.2 we illustrate the FHAM creep function and we define its three aging terms through a best-fitting procedure with Model B3. A numerical procedure for the evaluation of the FHAM relaxation function is also proposed in Subsection 3.4.2 and interesting comparisons between Model B3 and the proposed FHAM are reported in Subsection 3.4.3.

#### 3.4.1 The aging hereditariness of concrete: Model B3

Several experimental studies reported since the beginning of eighties (Bažant and Panula, 1980; Bažant and Wittmann, 1982) show that a significant evolution of the material hereditariness is involved for concrete specimens and structures. These latter considerations led to the introduction of the Model B3 (Bažant and Baweja, 2000) conceived to capture the aging hereditariness of concrete as,

$$J_B(t, t_0) = q_1 + C_0(t, t_0) + C_d(t, t_0, t'), \quad (3.12)$$

where  $J_B(t, t_0)$  is the creep function of Model B3, in which  $q_1$  is the instantaneous strain due to a unitary stress,  $C_0(t, t_0)$  is the compliance function for basic creep (creep at constant moisture content and no moisture movement through the material) and  $C_d(t, t_0, t')$  is an additional compliance function due to the simultaneous drying starting at time  $t'$ . Then,

the full expressions of  $C_0(t, t_0)$  and  $C_d(t, t_0, t')$  read as follows:

$$C_0(t, t_0) = q_2 Q(t, t_0) + q_3 \ln[1 + (t - t_0)^n] + q_4 \ln(t/t_0) \quad (3.13a)$$

$$C_d(t, t_0, t') = q_5 \left[ \exp\{-8H(t)\} - \exp\{-8H(t'_0)\} \right]^{1/2}, \quad (3.13b)$$

where  $q_2$ ,  $q_3$ , and  $q_4$  represent the aging viscoelastic compliance, the non-aging viscoelastic compliance and the flow compliance, respectively (Bažant et al., 1997). Moreover,  $Q(t, t_0)$  can be calculated either using an approximate explicit formula or by means of a numerical integration of its time derivative, whereas  $t'_0 = \max(t_0, t')$  is the time at which drying and loading first act simultaneously. It is worth noting that the expression of  $C_d$  (3.13) is valid if  $t \geq t'_0$ , otherwise  $C_d = 0$ . With regard to the five parameters, they can be determined by means of a statistical analysis or through the following expressions:  $q_1 = 0.6 \cdot 10^6 / E_{28}$ ,  $q_2 = 185.4c^{0.5}\bar{f}_c^{-0.9}$ ,  $q_3 = 0.29(w/c)^4 q_2$ ,  $q_4 = 20.3(a/c)^{-0.7}$ ,  $q_5 = 7.57 \cdot 10^5 \bar{f}_c^{-1} |\varepsilon_{sh\infty}|^{-0.6}$ . All the formulas above are given in SI (metrics) units (MPa,m). In addition,  $E_{28}$  is the Young's modulus at 28 days,  $c$  is the cement content,  $\bar{f}_c$  is the standard cylinder compression strength of concrete at 28 days,  $w/c$  is the water-cement ratio,  $a/c$  is the aggregate-cement ratio, and  $\varepsilon_{sh\infty}$  is the mean shrinkage strain.

An attentive exam of (3.12) entails that the creep function of Model B3 depends on both the loading time  $t_0$  and the elapsed time  $(t - t_0)$ . Thus, the aging nature of Model B3 is also evident in Figure 3.2, where the value of  $J_B(10000, t_0)$  decreases by an increase of  $t_0$ . For further details about Model B3, the interested readers may refer to Bažant and Baweja (2000).

Regarding the relaxation function of Model B3, Bažant et al. (2013) proposes an approximate formula that prevents any violation of the thermodynamic requirement of negativeness. Furthermore, this formula can be utilized to describe long-term relaxation phenomena even in concretes loaded at a young age. The expression of the aforementioned

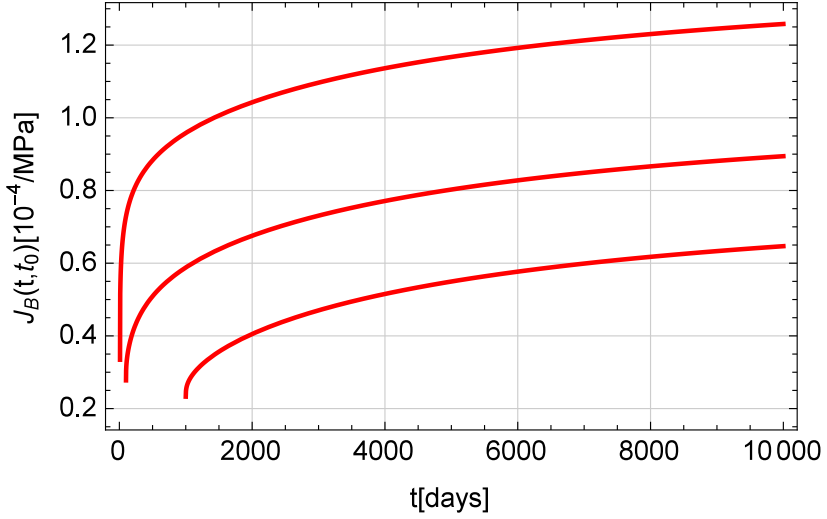


Figure 3.2: Creep function of Model B3 for different values of  $t_0$ .

approximate formula follows, i.e.,

$$G_B(t, t_0) = \frac{1}{J_B(t, t_0)} \cdot \left[ 1 + \frac{c_1 \alpha(t, t_0) J_B(t, t_0)}{q J_B(t, t - \eta)} \right]^{-q}, \quad (3.14)$$

where  $c_1 = 0.0119 \cdot \ln(t_0) + 0.08$ ,  $\alpha(t, t_0) = J_B\left(\frac{t + t_0}{2}, t_0\right) / J_B\left(t, \frac{t + t_0}{2}\right) - 1$ , with  $q = 10$  and  $\eta = 1$ . Thus, under the linear viscoelasticity hypothesis, the relaxation function of Model B3 can be accurately estimated by the explicit formula (3.14), leading to an analytical expression of the stress  $\sigma(t)$  as function of the strain history and material properties. Conversely, no analytical expression for  $\sigma(t)$  can be derived by numerically solving the Volterra equation (Bažant, 1972).

### 3.4.2 The fractional-aging hereditariness of concrete

In this subsection, we aim to formulate the constitutive behavior of aging concretes in the framework of variable-order fractional calculus. In this regard, we assume that the creep function belongs to the same fractional class of (3.8) yielding the following

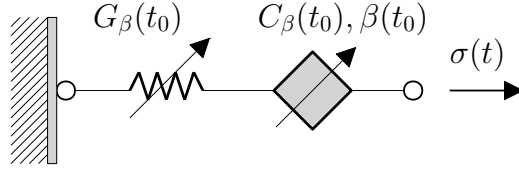


Figure 3.3: Variable-order fractional Maxwell model.

expression.

$$J_F(t, t_0) = \frac{1}{G_\beta(t_0)} + \frac{(t - t_0)^{\beta(t_0)}}{C_\beta(t_0)\Gamma(\beta(t_0) + 1)}, \quad (3.15)$$

where the creep function  $J_F(t, t_0)$  depends on both the elapsed time  $(t - t_0)$  and the material age  $t_0$ , as expected from a model describing the concrete aging hereditariness. Moreover, it corresponds to the definition of a rheological model consisting of a time-varying spring and a variable-order fractional dashpot, as depicted in Figure 3.3. The quantities  $C_\beta(t_0)$ ,  $G_\beta(t_0)$  and  $\beta(t_0)$  are aging functions representative of the material mechanical characteristics and environmental conditions. In particular,  $1/G_\beta(t_0)$  is the time-dependent compliance of concrete, whereas,  $\beta(t_0)$  and  $C_\beta(t_0)$  are related to the change of pore shapes and to the rearranging of the material microstructure during the closed phase. The explicit expressions of functions  $C_\beta(t_0)$ ,  $\beta(t_0)$  and  $G_\beta(t_0)$  can be derived through a best-fitting procedure with experimental data or in terms of an existing creep function.

From the creep function in Equation (3.15), we can then obtain the analytical expression of the relaxation function  $G_F(t, t_0)$  by means of the iterated-kernels method, as illustrated in Section 3.2. In this regard, we rewrite the Volterra integral equation (3.4) as follows:

$$G_F(t, t_0) = \frac{1}{J_F(t_0, t_0)} - \frac{1}{J_F(t_0, t_0)} \int_{t_0}^t G_F(t, \tau) \frac{\partial J_F(\tau, t_0)}{\partial \tau} d\tau, \quad (3.16)$$

where, according to Equation (3.15), the first partial derivative of the creep function takes the following form:

$$\frac{\partial J_F(\tau, t_0)}{\partial \tau} = \frac{(\tau - t_0)^{\beta(t_0)-1}}{\Gamma(\beta(t_0))C_\beta(t_0)}. \quad (3.17)$$

Then, through the application of the iterated-kernels method, we obtain the following approximations for the relaxation function, and similar expressions, herein omitted for brevity, can be derived for the successive kernels, i.e.:

$$\mathbf{G}_F^{(1)}(t, t_0) = \frac{1}{\mathbf{J}_F(t_0, t_0)} = \mathbf{G}_\beta(t_0), \quad (3.18a)$$

$$\mathbf{G}_F^{(2)}(t, t_0) = \mathbf{G}_\beta(t_0) - \mathbf{G}_\beta(t_0) \int_{t_0}^t \frac{(\tau - t_0)^{\beta(t_0)-1}}{\Gamma(\beta(t_0))\mathbf{C}_\beta(t_0)} \mathbf{G}_\beta(\tau) d\tau, \quad (3.18b)$$

$$\begin{aligned} \mathbf{G}_F^{(3)}(t, t_0) = & \mathbf{G}_\beta(t_0) - \mathbf{G}_\beta(t_0) \left[ \int_{t_0}^t \frac{(\tau - t_0)^{\beta(t_0)-1}}{\Gamma(\beta(t_0))\mathbf{C}_\beta(t_0)} \mathbf{G}_\beta(\tau) d\tau - \int_{t_0}^t \frac{(\tau - t_0)^{\beta(t_0)-1}}{\Gamma(\beta(t_0))\mathbf{C}_\beta(t_0)} \cdot \right. \\ & \left. \cdot \left( \int_\tau^t \frac{(\xi - \tau)^{\beta(\tau)-1}}{\Gamma(\beta(\tau))\mathbf{C}_\beta(\tau)} \mathbf{G}_\beta(\tau) \mathbf{G}_\beta(\xi) d\xi \right) d\tau \right], \end{aligned} \quad (3.18c)$$

.....

It is then important to highlight that, to accurately estimate the relaxation phenomenon, a large number of iterations is required, and this number increases with the size of the time interval  $[t, t_0]$ . Moreover, due to the variable-order nature of Riemann-Liouville integrals in (3.18), the composition property, illustrated in Appendix 3.B and used to reduce the dimension of multiple integrals within the framework of fractional calculus, cannot be applied anymore. In order to solve this problem, we simplify the multiple integrals involved into the iterated-kernels procedure by introducing the Grünwald-Letnikov approximation (Podlubny, 1998). Thus, Equations (3.18b) and (3.18c) become:

$$\mathbf{G}_F^{(2)}(t, t_0) = \mathbf{G}_\beta(t_0) - \frac{\mathbf{G}_\beta(t_0)h_1^{\beta(t_0)}}{\mathbf{C}_\beta(t_0)} \left( \sum_{r_1=0}^{\bar{n}_1} (-1)^{r_1} \binom{-\beta(t_0)}{r_1} \mathbf{G}_\beta(t_0 + r_1 h_1) \right) \quad (3.19a)$$

$$\begin{aligned} \mathbf{G}_F^{(3)}(t, t_0) = & \mathbf{G}_\beta(t_0) - \frac{\mathbf{G}_\beta(t_0)h_1^{\beta(t_0)}}{\mathbf{C}_\beta(t_0)} \left[ \left( \sum_{r_1=0}^{\bar{n}_1} (-1)^{r_1} \binom{-\beta(t_0)}{r_1} \mathbf{G}_\beta(t_0 + r_1 h_1) \right) + \right. \\ & - \left( \sum_{r_1=0}^{\bar{n}_1} (-1)^{r_1} \binom{-\beta(t_0)}{r_1} \frac{\mathbf{G}_\beta(t_0 + r_1 h_1)}{\mathbf{C}_\beta(t_0 + r_1 h_1)} h_2^{\beta(t_0+r_1 h_1)} \cdot \right. \\ & \left. \left. \cdot \left( \sum_{r_2=0}^{\bar{n}_2} (-1)^{r_2} \binom{-\beta(t_0 + r_1 h_1)}{r_2} \mathbf{G}_\beta(t_0 + r_1 h_1 + r_2 h_2) \right) \right) \right], \end{aligned} \quad (3.19b)$$

where  $\bar{n}_i$  indicates the number of subintervals used to approximate the generic fractional integral, and  $h_i$  represents the interval amplitude. For the sake of simplicity, we set a

unique number of subintervals, i.e.  $\bar{n}$ ; thus,  $h_1 = h_2 = \dots = h_i = (t - t_0)/\bar{n} = h$ ,  $\bar{n}_2 = \bar{n} - r_1$ ,  $\bar{n}_3 = \bar{n} - r_1 - r_2$ ,  $\bar{n}_4 = \bar{n} - r_1 - r_2 - r_3$ , and so on.

A further simplification can be reached with the introduction of the following column vector  $\mathbf{G}_\beta$  with dimension  $(\bar{n} + 1)$ :

$$\mathbf{G}_\beta = [\mathbf{G}_\beta(t_0) \quad \mathbf{G}_\beta(t_0 + h) \quad \dots \quad \mathbf{G}_\beta(t_0 + \bar{n}h)]^T = [g_1 \quad g_2 \quad \dots \quad g_{\bar{n}+1}]^T \quad (3.20)$$

and the upper-diagonal matrix  $\mathbf{L}$  with dimension  $(\bar{n} + 1) \times (\bar{n} + 1)$ :

$$\mathbf{L} = \begin{bmatrix} \frac{h^{\beta(t_0)} \mathbf{G}_\beta(t_0)}{C_\beta(t_0)} (-1)^0 \binom{-\beta(t_0)}{0} & \dots & \frac{h^{\beta(t_0)} \mathbf{G}_\beta(t_0)}{C_\beta(t_0)} (-1)^{\bar{n}} \binom{-\beta(t_0)}{\bar{n}} \\ & \ddots & \vdots \\ & & \frac{h^{\beta(t_0 + \bar{n}h)} \mathbf{G}_\beta(t_0 + \bar{n}h)}{C_\beta(t_0 + \bar{n}h)} (-1)^0 \binom{-\beta(t_0 + \bar{n}h)}{0} \end{bmatrix}. \quad (3.21)$$

Moreover, we indicate the matrix product between the generic  $j^{\text{th}}$  power of  $\mathbf{L}$  and  $\mathbf{G}_\beta$  with the following notation:

$$\mathbf{L}^j \cdot \mathbf{G}_\beta = [a_1^j \quad a_2^j \quad \dots \quad a_{\bar{n}+1}^j]^T. \quad (3.22)$$

The notation introduced in (3.20), (3.21), and (3.22) yields a compact definition of iterated kernels in (3.18) as follows:

$$\mathbf{G}_F^{(1)}(t, t_0) = g_1 \quad (3.23a)$$

$$\mathbf{G}_F^{(2)}(t, t_0) = g_1 - a_1^1 \quad (3.23b)$$

$$\mathbf{G}_F^{(3)}(t, t_0) = g_1 - [a_1^1 - a_1^2] \quad (3.23c)$$

.....

$$\mathbf{G}_F^{(k)}(t, t_0) = g_1 - \left[ \sum_{j=1}^{k-1} (-1)^{j-1} a_1^j \right], \quad (3.23d)$$

where with  $k$  we indicate the  $k^{\text{th}}$  approximation for the FHAM relaxation function that we assume can accurately describe the relaxation phenomena.

### 3.4.3 Derivation of the aging functions and model comparisons

In what follows, we illustrate the best-fitting procedure performed between the proposed FHAM and the existing aging Model B3 by considering as free parameters  $\beta$ ,  $C_\beta$  and  $G_\beta$ . The best fitting was referred to a specific concrete specimen and environmental conditions. In particular, the mechanical characteristics, the relative humidity and the geometry of the cross-section are summarized in Table 3.1. Hence, the five parameters of Model B3 can be now computed:  $q_1 = 19.33 \cdot 10^{-6}/\text{MPa}$ ;  $q_2 = 116.32 \cdot 10^{-6}/\text{MPa}$ ;  $q_3 = 2.87 \cdot 10^{-6}/\text{MPa}$ ;  $q_4 = 6.49 \cdot 10^{-6}/\text{MPa}$ ;  $q_5 = 323.50 \cdot 10^{-6}/\text{MPa}$ .

We perform the best-fitting procedure for a time window extended from  $t_0$  to 10000 days and by fulfilling the following physical conditions for a given  $t_0$ :  $C_\beta$  a positive real number,  $G_\beta$  a positive real number, and  $0 \leq \beta < 1$ . Table 3.2 collects the results of the best-fitting procedure, where a careful reader can observe that both  $\beta$  and  $C_\beta$  increase until  $t_0 = 8000$  days, after that they start to decrease. Likewise, the parameter  $G_\beta$  increases until  $t_0 = 400$  days, after that it is almost constant. From the results in Table 3.2, the corresponding trends of  $\beta$ ,  $G_\beta$ , and  $C_\beta$  can be easily expressed as function of  $t_0$ . As a result, the expressions of  $\beta(t_0)$ ,  $G_\beta(t_0)$ , and  $C_\beta(t_0)$  are depicted in Figures 3.4(a), 3.4(b), 3.4(c) and listed in (3.24a) (3.24b) (3.24c).

$$\begin{aligned} \beta(t_0) = & \Theta(T_2 - t_0) \cdot f_1^\beta(t_0) + \Theta(t_0 - T_2) \cdot f_2^\beta(t_0) + \Theta(t_0 - T_3) \cdot f_3^\beta(t_0) \\ & - \Theta(t_0 - T_3) \cdot f_2^\beta(t_0) \end{aligned} \quad (3.24a)$$

$$\begin{aligned} G_\beta(t_0) = & \Theta(T_2 - t_0) \cdot f_1^{G_\beta}(t_0) + \Theta(t_0 - T_2) \cdot f_2^{G_\beta}(t_0) + \Theta(t_0 - T_3) \cdot f_3^{G_\beta}(t_0) \\ & - \Theta(t_0 - T_3) \cdot f_2^{G_\beta}(t_0) \end{aligned} \quad (3.24b)$$

$$\begin{aligned} C_\beta(t_0) = & \Theta(T_4 - t_0) \cdot f_1^{C_\beta}(t_0) + \Theta(t_0 - T_4) \cdot f_2^{C_\beta}(t_0) + \Theta(t_0 - T_3) \cdot f_3^{C_\beta}(t_0) \\ & - \Theta(t_0 - T_3) \cdot f_2^{C_\beta}(t_0), \end{aligned} \quad (3.24c)$$

where  $\Theta(\cdot)$  indicates the Heaviside step function and  $T_1 = 10$  days,  $T_2 = 100$  days,  $T_3 = 1000$  days,  $T_4 = 200$  days.

In order to reduce percentage errors between approximate and real trends of the three

Table 3.1: Mechanical and environmental conditions of a specimen chosen for the best-fitting procedure.

$\bar{f}_c$ - cylinder compression strength at 28 days [MPa]	43
$E_{28}$ - Young modulus at 28 days [MPa]	31043
$w/c$ - water-cement ratio	0.54
$a/c$ - aggregate-cement ratio	5.10
$c$ - cement content $[\text{kg}/\text{m}^3]$	343.04
$m$ - empirical parameter	0.5
$n$ - empirical parameter	0.1
$t'$ - drying time [ <i>days</i> ]	7
$RH$ - relative humidity [%]	60
$k_S$ - cross-section shape factor	1.25
$V/S$ - volume to surface ratio [cm]	15

parameters, three functions active in different time intervals are used to describe each parameter. In particular, a second-degree function  $f_1^\beta(t_0)$  is the best choice to fit the values of  $\beta$  within the time interval  $[10, 100]$  days. Later on, two sixth-degree polynomials, i.e.  $f_2^\beta(t_0)$  and  $f_3^\beta(t_0)$ , are selected to perform the best-fitting within  $[100, 1000]$  and

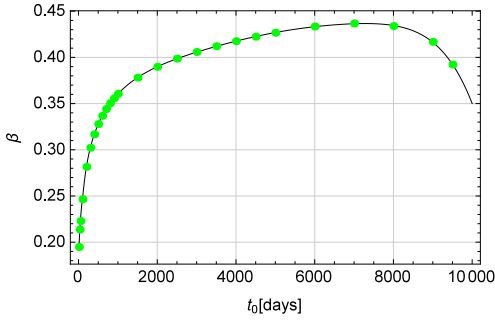
Table 3.2: Values of  $\beta$ ,  $G_\beta$ , and  $C_\beta$  obtained through the best-fitting procedure.

$t_0$	$\beta$	$G_\beta$	$C_\beta$
10	0.199	27483.0	74753.76
100	0.247	47511.9	152988.32
200	0.282	47832.5	238684.18
400	0.317	48061.9	373440.96
600	0.337	47994.2	484741.42
800	0.350	47829.6	582564.53
1000	0.361	47636.2	670241.33
3000	0.406	46132.2	1354441.39
5000	0.427	45429.0	1986155.88
7000	0.437	45181.1	2565382.86
9500	0.392	45656.2	2266373.77

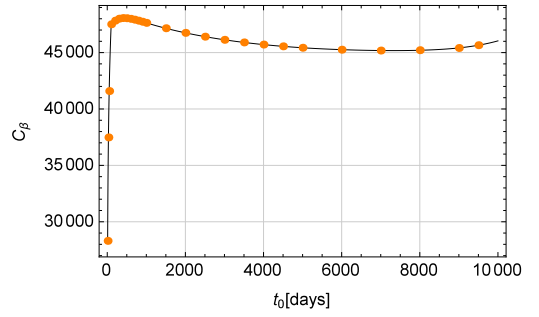
[1000, 10000] days, respectively. Then, a logarithmic function  $f_1^{G_\beta}(t_0)$  is chosen to fit the values of  $G_\beta$  within the interval [10, 100] days; afterwards two sixth-degree polynomials, i.e.  $f_2^{G_\beta}(t_0)$  and  $f_3^{G_\beta}(t_0)$ , are selected for [100, 1000] and [1000, 10000] days. Regarding the last parameter,  $C_\beta$ , a second-degree function  $f_1^{C_\beta}(t_0)$  is selected for the best-fitting within [10, 200] days, whilst two sixth-degree polynomials, i.e.  $f_2^{C_\beta}(t_0)$  and  $f_3^{C_\beta}(t_0)$ , are chosen for [200, 1000] and [1000, 10000] days. All functions used to describe  $\beta(t_0)$ ,  $G_\beta(t_0)$ , and  $C_\beta(t_0)$  are reported in Appendix 3.C.

Figure 3.5(a) depicts the comparison between the Model B3 creep function and the FHAM creep function, both computed for a loading time of 10 days. The fractional-aging model provides values of the creep function very similar to the values of the reference model. For instance, at 11 days we compute the maximum percentage error of 5.6%. There is also a high degree of matching in Figure 3.5(c), with the maximum percentage error of 6.2% at 1001 days.

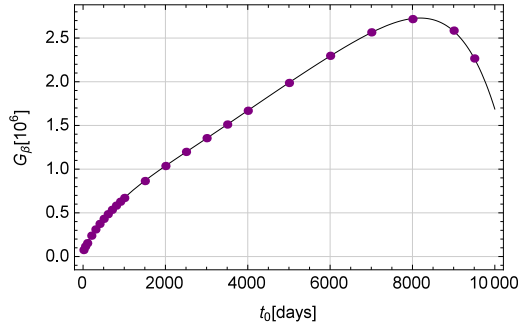
Another important comparison regards relaxation functions evaluated for different loading times. In particular, to compute the FHAM relaxation function, we follow the procedure described in Subsection 3.4.2 by setting  $\bar{n} = 170$  and  $k = 200$ ; whilst, to compute the relaxation function of Model B3, we use the improved approximate formula proposed by Bažant et al. (2013) and illustrated in Subsection 3.4.1. Thus, Figures 3.6(a), 3.6(b), and 3.6(c) depict both the FHAM and Model B3 relaxation function for loading ages  $t_0 = 10, 100, \text{ and } 1000$  days, respectively. The fractional relaxation function is plotted as dotted red line, whereas, the Model B3 relaxation function is plotted as thick solid blue line. Moreover, the thin solid black line indicates our reference solution, i.e. the relaxation function of Model B3 obtained by numerically solving the Volterra's integral as shown in Appendix of Bažant (1972). Overall, from the comparison of relaxation functions, we conclude that the procedure proposed in Subsection 3.4.2 leads to values of the relaxation function very close to the reference solution, especially for the case of long-term relaxation beginning at ages  $t_0 = 100$  and 1000 days. Furthermore, the approximate formula suggested by Bažant et al. (2013) resulted less accurate than the proposed formula (3.23) for the evaluation of the structural response at the long term, i.e.



(a) Trend of the parameter  $\beta$ .



(b) Trend of the parameter  $C_\beta$ .



(c) Trend of the parameter  $C_\beta$ .

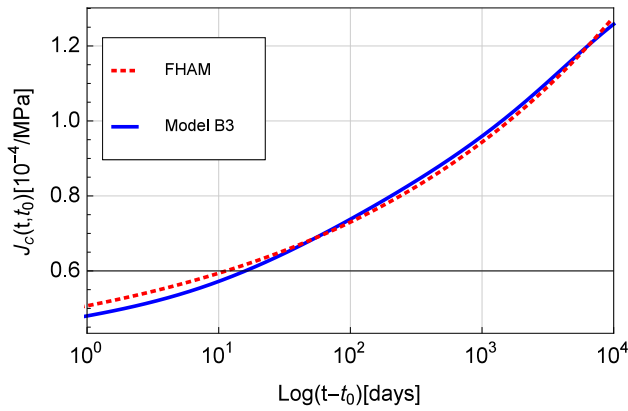
Figure 3.4: Results of the best-fitting procedure with Model B3 creep function and representations of functions  $\beta(t_0)$ ,  $G_\beta(t_0)$ , and  $C_\beta(t_0)$  by means of the solid black line.

$t = 10000$  days.

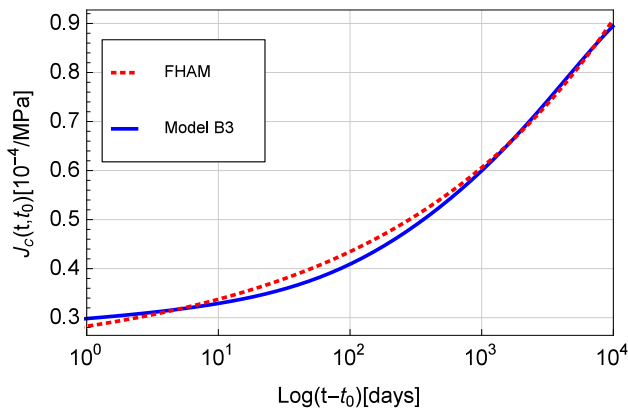
### 3.5 Conclusions

In this paper we propose a novel fractional-order model for the characterization of the hereditariness of aging materials.

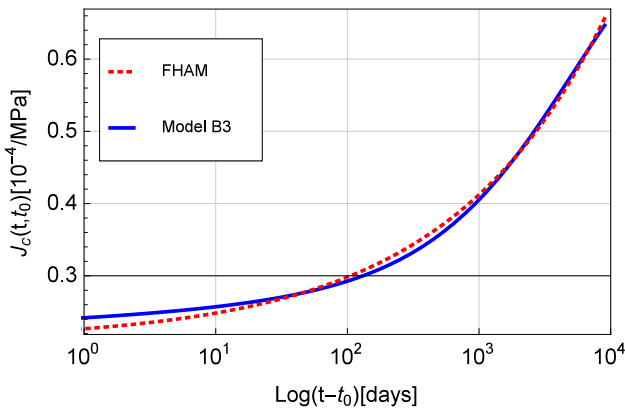
More precisely, as discussed in Sections 3.2 and 3.3, no fractional-order model available in literature is suitable to describe the degradation/improvement of mechanical characteristics, which is a phenomenon typical in aging materials, like structural concretes, rubbers and polymers under photo-degradation. Nonetheless, the use of fractional-order models to describe both creep and relaxation phenomena can bring many advantages,



(a) Comparison for  $t_0 = 10$  days.

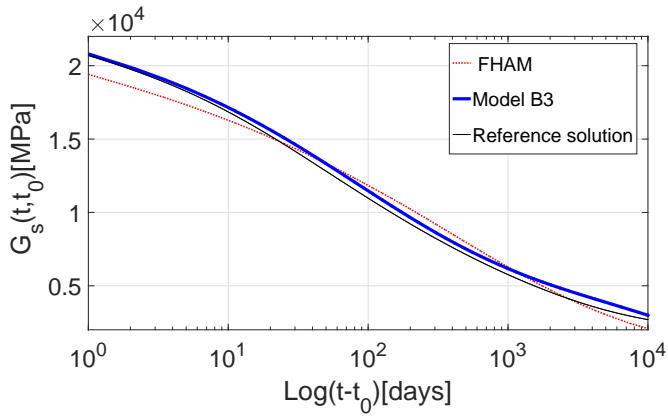


(b) Comparison for  $t_0 = 100$  days.

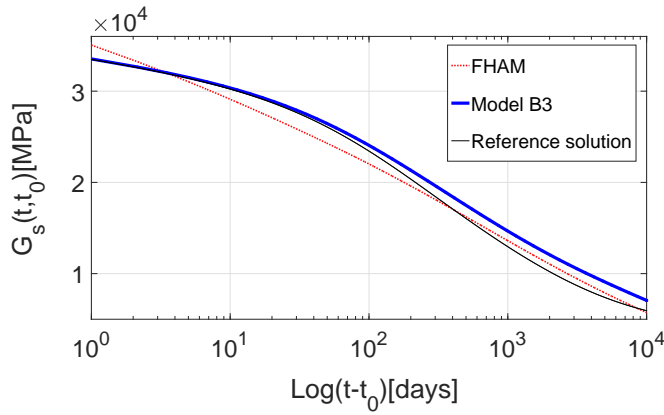


(c) Comparison for  $t_0 = 1000$  days.

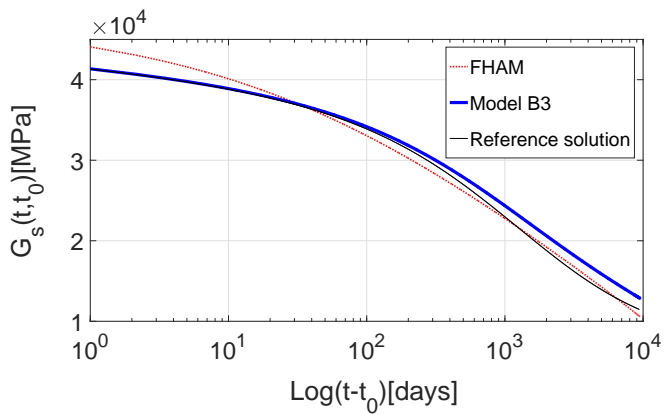
Figure 3.5: Comparisons between the Model B3 creep function and the FHAM creep function for different values of the loading time  $t_0$ .



(a) Comparison for  $t_0 = 10$  days.



(b) Comparison for  $t_0 = 100$  days.



(c) Comparison for  $t_0 = 1000$  days.

Figure 3.6: Comparisons among the Model B3 relaxation function, the FHAM relaxation function, and the reference solution, which was evaluated according to Bažant (1972).

such as a more realistic description of creep/relaxation and computational savings for the solution of the Volterra integral equation, as proven by many studies on material hereditarity. On these bases, in Section 3.4, we propose a fractional-order creep function suitable for aging-hereditary materials, characterized by three aging terms,  $C_\beta(t_0)$ ,  $\beta(t_0)$  and  $G_\beta(t_0)$ , and an hereditary term function of the elapsed time  $(t - t_0)$ . Moreover, considering an aging concrete, the inverse of  $G_\beta(t_0)$  describes the time-dependent compliance, and both  $\beta(t_0)$  and  $C_\beta(t_0)$  are related to the change of pore shapes and to the rearranging of the material microstructure. In Section 3.4, we also propose an effective procedure for exactly deriving the corresponding relaxation function by starting from the well-known Volterra integral equation of the second kind. The explicit expressions of  $G_\beta(t_0)$ ,  $\beta(t_0)$  and  $C_\beta(t_0)$  are derived for a specific medium-strength concrete and through a best-fitting procedure with the creep function of Model B3, one of the most widely used models for prestressed concrete. The relevant comparison between Model B3 creep function and the creep function of the proposed fractional model entails percentage errors less than 6%, which is a reasonable value in engineering practice. A good agreement is also found between the relaxation functions, proving once more that the proposed model can be effectively applied to the simulation of aging hereditarity of materials like concrete and prestressed concrete.

As further development, the best-fitting procedure illustrated in Section 3.4 can be used to correlate  $G_\beta(t_0)$ ,  $\beta(t_0)$  and  $C_\beta(t_0)$  of the proposed fractional-order model with experimental data available in the database of RILEM (2016). Finally, the influence of mechanical properties, environmental conditions and cross-section geometry on  $G_\beta(t_0)$ ,  $\beta(t_0)$  and  $C_\beta(t_0)$  deserves further studies.

### 3.A Fundamental remarks of fractional calculus

Fractional calculus may be considered the extension of the ordinary differential calculus to non-integer powers of derivation orders. In this section, we address some basic notions about this mathematical tool.

Riemann-Liouville fractional integrals and derivatives with  $0 < \beta < 1$  of functions defined on the entire real axis have the following forms,

$$\left(I_+^\beta f\right)(t) = \frac{1}{\Gamma(\beta)} \int_{-\infty}^t \frac{f(\tau)}{(t-\tau)^{1-\beta}} d\tau \quad (3.25a)$$

$$\left(D_+^\beta f\right)(t) = \frac{1}{\Gamma(1-\beta)} \frac{d}{dt} \int_{-\infty}^t \frac{f(\tau)}{(t-\tau)^\beta} d\tau. \quad (3.25b)$$

Riemann-Liouville fractional integrals and derivatives, with  $0 < \beta < 1$ , of functions defined over intervals of the real axis, namely  $f(t)$  such that  $t \in [a, b] \subset \mathbb{R}$ , have the following forms,

$$\left(I_a^\beta f\right)(t) = \frac{1}{\Gamma(\beta)} \int_a^t \frac{f(\tau)}{(t-\tau)^{1-\beta}} d\tau \quad (3.26a)$$

$$\left(D_a^\beta f\right)(t) = \frac{f(a)}{\Gamma(1-\beta)(t-a)^\beta} + \frac{1}{\Gamma(1-\beta)} \int_a^t \frac{f'(\tau)}{(t-\tau)^\beta} d\tau \quad (3.26b)$$

where the Euler-Gamma function  $\Gamma(z)$  is the generalization of the factorial function since as  $z$  assumes integer values as  $\Gamma(z+1) = z!$ . The Euler-Gamma function defined as the result of the integral reads,

$$\Gamma(z) = \int_0^\infty e^{-x} x^{z-1} dx. \quad (3.27)$$

In addition to the Riemann-Liouville fractional operators illustrated above, another class of fractional derivatives that is often used in the context of the fractional viscoelasticity is represented by Caputo fractional derivatives, defined as,

$$\left({}_C D_{a^+}^\beta f\right)(t) := I_{a^+}^{m-\beta} \left(D_{a^+}^m f\right)(t) \quad m-1 < \beta < m \quad (3.28)$$

and, whenever  $0 < \beta < 1$ , it reads,

$$\left({}_C D_{a^+}^\beta f\right)(t) = \frac{1}{\Gamma(1-\beta)} \int_a^t \frac{f'(\tau)}{(t-\tau)^\beta} d\tau \quad (3.29)$$

A closer analysis of (3.28) and (3.29) shows that Caputo fractional derivative coincides with the integral part of the Riemann-Liouville fractional derivative in a bounded domain. Moreover, the definition in (3.28) entails that the function  $f(t)$  has to be absolutely integrable of order  $m$  (e.g. in (3.29) the order is  $m = 1$ ). Whenever  $f(a) = 0$ , Caputo and Riemann-Liouville fractional derivatives coalesce.

Similar considerations hold true also for Caputo and Riemann-Liouville fractional derivatives defined on the entire real axis. Caputo fractional derivatives may be considered as the interpolation among the well-known integer-order derivatives, operating over functions  $f(\circ)$  that belong to the class of Lebesgue integrable functions ( $f(\circ) \in L^1$ ); as a consequence, they are very useful in the mathematical description of a complex system evolution. We recall that Laplace and Fourier integral transforms are defined as follows,

$$\mathcal{L}[f(t)] = \int_0^{\infty} f(t)e^{-st} dt \quad (3.30a)$$

$$\mathcal{F}[f(t)] = \int_{-\infty}^{+\infty} f(t)e^{i\omega t} dt \quad (3.30b)$$

It is worth introducing integral transforms for fractional operators and, similarly to classical calculus, the Laplace integral transform  $\mathcal{L}(\circ)$  can be defined in the following forms:

$$\mathcal{L} \left[ \left( D_{0+}^{\beta} f \right) (t) \right] = s^{\beta} \mathcal{L}[f(t)] = s^{\beta} \tilde{f}(s) \quad (3.31a)$$

$$\mathcal{L} \left[ \left( I_{0+}^{\beta} f \right) (t) \right] = s^{-\beta} \mathcal{L}[f(t)] = s^{-\beta} \tilde{f}(s) \quad (3.31b)$$

Likewise, the Fourier integral transform  $\mathcal{F}(\circ)$  assumes the following forms,

$$\mathcal{F} \left[ \left( D_{+}^{\beta} f \right) (t) \right] = (-i\omega)^{\beta} \mathcal{F}[f(t)] = (-i\omega)^{\beta} \hat{f}(\omega) \quad (3.32a)$$

$$\mathcal{F} \left[ \left( I_{+}^{\beta} f \right) (t) \right] = (-i\omega)^{-\beta} \mathcal{F}[f(t)] = (-i\omega)^{-\beta} \hat{f}(\omega) \quad (3.32b)$$

### 3.B Fractional calculus of variable order

In this section we briefly recall the main concepts of fractional calculus, when the order of integration/differentiation is allowed to vary with the independent variable  $t$ . Lorenzo

and Hartley (1998) first suggested the concept of variable-order fractional operators and several candidate definitions for variable-order fractional integrals are addressed in Lorenzo and Hartley (2002). Moreover, the definitions for the variable-order integration introduced by Lorenzo and Hartley (2002) may be formally extended to variable-order fractional differentiation as illustrated in Ingman and Suzdalnitsky (2005) and Valério and Da Costa (2011).

Recalling Riemann-Liouville fractional integrals and derivatives with order  $0 < \beta < 1$  defined in Equations (4.5), in the current case of variable-order fractional calculus, they become,

$$\left( I_a^{\beta(t)} f \right) (t) = \int_a^t \frac{(t - \tau)^{\beta(t, \tau) - 1}}{\Gamma(\beta(t, \tau))} f(\tau) d\tau \quad (3.33a)$$

$$\left( D_a^{\beta(t)} f \right) (t) = \frac{(t - a)^{-\beta(t, a)}}{\Gamma(1 - \beta(t, a))} f(a) + \int_a^t \frac{(t - \tau)^{-\beta(t, \tau)}}{\Gamma(1 - \beta(t, \tau))} f'(\tau) d\tau \quad (3.33b)$$

where the order of integration/differentiation is now function of the independent variable  $t$  and the integration/differentiation variable  $\tau$ .

In the discussion that follows we focus on the main implications resulting from various choices of  $\beta(t, \tau)$ , assuming that the arguments of  $\beta(t, \tau)$  at the exponent of  $(t - \tau)$  and in the Gamma function are the same. In particular, the following choices are considered:  $\beta(t, \tau) = \beta(t)$ ;  $\beta(t, \tau) = \beta(\tau)$ ;  $\beta(t, \tau) = \beta(t - \tau)$ . However, a briefly discussion is pointed out in this appendix; thus, more details about all cases can be found in Lorenzo and Hartley (2002) and Valério and Da Costa (2011).

### 3.B.1 Case 1 $\beta(t, \tau) = \beta(t)$

For this case, we redefine the Riemann-Liouville fractional integral and derivative as follows,

$$\left( I_a^{\beta(t)} f \right) (t) = \int_a^t \frac{(t - \tau)^{\beta(t) - 1}}{\Gamma(\beta(t))} f(\tau) d\tau \quad (3.34a)$$

$$\left( D_a^{\beta(t)} f \right) (t) = \frac{(t - a)^{-\beta(t)}}{\Gamma(1 - \beta(t))} f(a) + \int_a^t \frac{(t - \tau)^{-\beta(t)}}{\Gamma(1 - \beta(t))} f'(\tau) d\tau \quad (3.34b)$$

Since the argument of  $\beta(t)$  at the exponent of  $(t - \tau)$  in (3.34) is not a function of  $(t - \tau)$ , the fractional operator becomes time variant. We recall that an operator is said to be time invariant when the input  $f(t)$  produces a response  $y(t)$ , then the input  $f(t + \Delta t)$  produces the response  $y(t + \Delta t)$  (Lorenzo and Hartley, 2002). Moreover, it is noted that the operator is no more linear with respect to the order  $\beta(t)$ . Hence, the composition property is not applicable, i.e.,

$$I_+^{\beta(t)} I_+^{\alpha(t)} f(t) \neq \left( I_+^{\beta(t)+\alpha(t)} f \right) (t) \quad (3.35)$$

### 3.B.2 Case 2 $\beta(t, \tau) = \beta(\tau)$

For this case, we redefine the Riemann-Liouville fractional integral and derivative as follows,

$$\left( I_a^{\beta(t)} f \right) (t) = \int_a^t \frac{(t - \tau)^{\beta(\tau)-1}}{\Gamma(\beta(\tau))} f(\tau) d\tau \quad (3.36a)$$

$$\left( D_a^{\beta(t)} f \right) (t) = \frac{(t - a)^{-\beta(a)}}{\Gamma(1 - \beta(a))} f(a) + \int_a^t \frac{(t - \tau)^{-\beta(\tau)}}{\Gamma(1 - \beta(\tau))} f'(\tau) d\tau \quad (3.36b)$$

Because of the argument of  $\beta(\tau)$  in both the exponent of  $(t - \tau)$  and Gamma function, the fractional operator results to be time variant. Moreover, as previously discussed for Case 1, the composition property in (4.8) is no more valid. It is important to highlight that the last implication strongly influenced the evaluation of the fractional relaxation function in Subsection (3.4.2). In particular, if the composition property was still valid for the case under investigation, i.e.  $\beta(t, \tau) = \beta(\tau)$ , the relaxation function of the proposed fractional aging model would be simpler to carry out and the final expression of the relaxation function would be a combination of Riemann-Liouville integrals with maximum order  $i \cdot \beta$ , where  $i$  indicates the number of iterated kernels used to approximate the solution (Tricomi, 1957).

### 3.B.3 Case 3 $\beta(t, \tau) = \beta(t - \tau)$

For the last case under investigation we consider the definitions,

$$\left(I_a^{\beta(t)} f\right)(t) = \int_a^t \frac{(t - \tau)^{\beta(t-\tau)-1}}{\Gamma(\beta(t - \tau))} f(\tau) d\tau \quad (3.37a)$$

$$\left(D_a^{\beta(t)} f\right)(t) = \frac{(t - a)^{-\beta(t-a)}}{\Gamma(1 - \beta(t - a))} f(a) + \int_a^t \frac{(t - \tau)^{-\beta(t-\tau)}}{\Gamma(1 - \beta(t - \tau))} f'(\tau) d\tau \quad (3.37b)$$

Now, since the argument of  $\beta(t - \tau)$  in both the exponent of  $(t - \tau)$  and Gamma function is function of  $(t - \tau)$ , the fractional operators are time invariant, as defined for Case 1 earlier. Moreover, also for this last case of variable-order operator the composition property in (4.8) is no more applicable.

### 3.C FHAM functions

In the following, we list all functions needed to define  $\beta(t_0)$ ,  $C_\beta(t_0)$ , and  $G_\beta(t_0)$  in Subsection 3.4.3, i.e.

$$f_1^\beta(t_0) = -3.10 \cdot 10^{-6}(t_0 - T_1)^2 + 7.99 \cdot 10^{-4}(t_0 - T_1) + 0.199 \quad (3.38a)$$

$$\begin{aligned} f_2^\beta(t_0) = & -1.11 \cdot 10^{-18}(t_0 - T_2)^6 + 3.63 \cdot 10^{-15}(t_0 - T_2)^5 + \\ & -4.81 \cdot 10^{-12}(t_0 - T_2)^4 + 3.39 \cdot 10^{-9}(t_0 - T_2)^3 + \\ & -1.45 \cdot 10^{-6}(t_0 - T_2)^2 + 4.68 \cdot 10^{-4}(t_0 - T_2) + f_1^\beta(T_2) \end{aligned} \quad (3.38b)$$

$$\begin{aligned} f_3^\beta(t_0) = & -6.41 \cdot 10^{-24}(t_0 - T_3)^6 + 1.53 \cdot 10^{-19}(t_0 - T_3)^5 + \\ & -1.46 \cdot 10^{-15}(t_0 - T_3)^4 + 7.17 \cdot 10^{-12}(t_0 - T_3)^3 + \\ & -2.02 \cdot 10^{-8}(t_0 - T_3)^2 + 4.36 \cdot 10^{-5}(t_0 - T_3) + f_2^\beta(T_3) \end{aligned} \quad (3.38c)$$

$$f_1^{G_\beta}(t_0) = 8674.33 \cdot \ln(t_0) + 7379.72 \quad (3.38d)$$

$$f_2^{G_\beta}(t_0) = -3.03 \cdot 10^{-15}(t_0 - T_2)^6 + 9.65 \cdot 10^{-11}(t_0 - T_2)^5 +$$

$$\begin{aligned}
& - 1.24 \cdot 10^{-7}(t_0 - T_2)^4 + 8.45 \cdot 10^{-5}(t_0 - T_2)^3 + \\
& - 3.41 \cdot 10^{-2}(t_0 - T_2)^2 + 7.72(t_0 - T_2) + f_1^{G\beta}(T_2)
\end{aligned} \tag{3.38e}$$

$$\begin{aligned}
f_3^{G\beta}(t_0) = & 3.06 \cdot 10^{-20}(t_0 - T_3)^6 - 6.47 \cdot 10^{-16}(t_0 - T_3)^5 + \\
& + 5.89 \cdot 10^{-12}(t_0 - T_3)^4 - 3.50 \cdot 10^{-8}(t_0 - T_3)^3 + \\
& + 2.07 \cdot 10^{-4}(t_0 - T_3)^2 - 1.06(t_0 - T_3) + f_2^{G\beta}(T_3)
\end{aligned} \tag{3.38f}$$

$$f_1^{C\beta}(t_0) = - 0.37(t_0 - T_1)^2 + 931(t_0 - T_1) + 74753.76 \tag{3.38g}$$

$$\begin{aligned}
f_2^{C\beta}(t_0) = & 2.32 \cdot 10^{-13}(t_0 - T_4)^6 - 3.65 \cdot 10^{-10}(t_0 - T_4)^5 + \\
& - 5.71 \cdot 10^{-8}(t_0 - T_4)^4 + 4.9 \cdot 10^{-4}(t_0 - T_4)^3 + \\
& - 0.55(t_0 - T_4)^2 + 767.75(t_0 - T_4) + f_1^{C\beta}(T_4)
\end{aligned} \tag{3.38h}$$

$$\begin{aligned}
f_3^{C\beta}(t_0) = & - 5.62 \cdot 10^{-17}(t_0 - T_3)^6 + 1.2 \cdot 10^{-12}(t_0 - T_3)^5 + \\
& - 1.06 \cdot 10^{-8}(t_0 - T_3)^4 + 4.74 \cdot 10^{-5}(t_0 - T_3)^3 + \\
& - 0.11(t_0 - T_3)^2 + 437.57 \cdot 10^{-3}(t_0 - T_3) + f_2^{C\beta}(T_3)
\end{aligned} \tag{3.38i}$$

## Chapter 4

### **A numerical integration approach for fractional-order viscoelastic analysis of hereditary-aging structures**

*by Angela Beltempo, Alessio Bonelli, Oreste S. Bursi, and Massimiliano Zingales*

#### **Abstract**

In this paper, a novel numerical integration scheme is proposed for fractional-order viscoelastic analysis of hereditary-aging structures. More precisely, the idea of aging is first introduced through a new phenomenological viscoelastic model characterized by variable-order fractional operators. Then, the presented fractional-order viscoelastic model is included in a variational formulation, conceived for any viscous kernel and discretized in time by employing a discontinuous Galerkin method. The accuracy of the resulting FE scheme is analyzed through a model problem, whose exact solution is known; and the most significant variables affecting the solution quality, such as the number of Gaussian quadrature points and time subintervals, are then investigated in terms of error and computational cost. Eventually, the proposed FE integration scheme is applied to study the short- and long-term behavior of concrete structures, which, due to the severe aging exhibited during their service life, represents one of the most challenging time-dependent behavior to be investigated.

**Keywords:** aging hereditariness; variable-order fractional calculus; structural analysis; linear viscoelasticity; concrete; convergence analysis.

## 4.1 Introduction

### 4.1.1 Background and motivation

The viscoelastic models used in literature to analyze time-dependent phenomena, like creep and relaxation, usually rely on rheological schemes composed of springs and dashpots (Christensen, 1971; Flügge, 2013). However, such elementary models can be successfully employed to observe the short-term response of real materials, but they become inaccurate for long-term observations. For instance, due to their exponential nature both creep and relaxation curves present an asymptote, not observed during real experiments; furthermore, a single exponential-based model is not suitable for describing at the same time creep and relaxation phenomena. A possible solution to overcome the drawbacks exhibited by classical viscoelastic models is given by the use of power laws with real-order exponent. Moreover, the introduction of power laws into the Boltzmann linear superposition principle (Boltzmann, 1878) yields to the description of material constitutive behavior through the so-called fractional-order integrals and derivatives (Podlubny, 1998). These operators are mathematically well defined (Samko et al., 1987); in addition, they can be defined as a non-euclidean measure of Sobolev spaces (Bongiorno et al., 2002; Bongiorno, 2004, 2014; Bongiorno and Corrao, 2015a).

The application of fractional calculus to linear viscoelasticity covers many decades and finds its bases in twenties with (Nutting, 1921) and (Gemant, 1938). All studies on this topic, such as Cataldo et al. (2015), Deseri et al. (2013), Di Paola et al. (2013a), and Di Paola and Granata (2016), proved the success of using fractional differential operators in the description of time-dependent phenomena exhibited by hereditary materials, like polymers, rubbers and biological tissues. A fractional-order viscoelastic model suitable for aging materials, i.e. materials whose mechanical properties vary over their service life, has been recently proposed by Beltempo et al. (2017) with the aid of variable-order operators (Lorenzo and Hartley, 2002, 2007). The model is characterized by three parameters only and can be adopted to study any aging material by assigning to these

parameters specific laws, which must be function of material age. However, to the best of authors' knowledge, Beltempo et al. (2017) represents the first study that investigates the applicability of fractional-order operators to the characterization of both creep and relaxation phenomena taking material aging into account. Thus, the effective use of such operators in the context of material aging still needs a wide investigation, especially in relation to their use in structural analysis.

The simplest way to analyze the viscoelastic behavior of real structures is given by their modeling in commercial software and, then, by means of the relevant creep analysis. Nonetheless, in some cases, such as for structures highly sensitive to time-dependent phenomena, more refined procedures are required (Beltempo et al., 2018). For instance, the use of a variational formulation conceived for viscoelastic problems may bring more accurate solutions and can allow for the choice of a proper viscous kernel. The idea of using viscoelastic variational formulation for structural analyses is certainly not new. It dates back to Biot (1956) and finds its first generalization in Gurtin (1963), which provided variational principles, for both relaxation and creep integral forms. Later, several authors exploited the same research field, mainly focusing on the reformulation of viscoelastic problems in variational terms. For instance, Christensen (1968) under restrictive assumptions proposed a variational formulation and established minimum theorems for linear viscoelasticity. Furthermore, other interesting attempts were made by other researchers, like Rafalski (1969), Taylor et al. (1970), Breuer (1973), Reiss and Haug (1978), Huet (1992), and Idesman et al. (2000). As regards Finite Element (FE) techniques developed within the framework of fractional calculus, Cortés and Elejabarrieta (2007) proposed an approach for transient dynamic analyses, while Musto and Alfano (2015) illustrated a FE procedure, where a fractional hereditary model was implemented into a user subroutine of the software ABAQUS (Smith, 2009). However, all the aforementioned works led to FE formulations suitable for hereditary materials or for particular conditions, but not applicable to a general viscous kernel. A more general variational approach was instead derived by Carini et al. (1995b), where an extremal FE formulation was proposed under the assumptions of a non-homogeneous and non-isotropic solid. The formulation

relies on Tonti (1984) and is based on an extension of the classical total potential energy with a relaxation integral form. In addition, it was applied to aging concretes through the CEB'78 model (Chiorino, 1984).

In sum, we underline that no FE approach has been proposed for a fractional-order viscous kernel in presence of material aging until now. In addition, limited convergence analyses were performed in the same context. These are important issues that this article explores further.

#### **4.1.2 Scope**

Along these lines, this paper proposes a novel numerical integration scheme for the fractional-order aging constitutive law proposed by Beltempo et al. (2017). The presented method relies on the variational formulation developed by Carini et al. (1995b) and, is herein illustrated under the assumptions of Euler-Bernoulli and first-order beam theories. Moreover, an accuracy analysis is performed on a model problem for which the exact solution is known. As a result, both the number of Gaussian quadrature points and the number of subintervals, used in the step-by-step time procedure, are analyzed in terms of error and computational cost.

The paper is organized as follows: we introduce the idea of hereditary aging materials together with a suitable fractional-order constitutive law in Section 4.2; in Section 4.3, we present the numerical integration scheme characterized by a fractional relaxation kernel; in Section 4.4, we perform a convergence analysis of the proposed scheme by considering a suitable model problem, and in Section 4.5 we apply the proposed fractional-order formulation to representative concrete structures. Main conclusions are summarized in Section 4.6 with further developments.

#### **4.2 Fractional-hereditary aging materials**

Due to the success of fractional-order operators in the characterization of the long-term behavior of hereditary materials, e.g. polymers and rubbers, in this study we investigate

their applicability to more complex cases, like aging materials. Along this line, in this section we first introduce remarks on material aging hereditariness; then, we focus on the idea of fractional calculus of variable order, which leads to a correct description of the aging phenomenon within the framework of fractional calculus. Finally, we present the fractional hereditary aging model recently derived by Beltempo et al. (2017), to be introduced as aging kernel into the proposed fractional-order numerical scheme for structural analysis.

#### 4.2.1 Material aging hereditariness

The constitutive behavior of materials in long-standing mechanical tests is well described by means of creep and relaxation functions, named  $J(t, t_0)$  and  $G(t, t_0)$ , respectively. The creep function represents the strain undergone by the specimen due to an unitary stress applied at the time instant  $t_0$ , i.e.  $\sigma(t_0) = 1$ ; while, the relaxation function measures the stress at the generic time instant  $t$  due to an applied unitary strain at  $t_0$ ,  $\varepsilon(t_0) = 1$ , with  $t \geq t_0$ .

In this work, we focus on a specific class of materials, whose mechanical properties continuously vary over time. They are known in literature as hereditary aging materials (Jirásek and Bazant, 2002), and the relevant creep and relaxation functions depend on both the elapsed time,  $(t - t_0)$ , and the material age when the load is applied,  $t_0$ . Examples in nature of hereditary aging materials are structural concretes, rubbers and polymers under photo degradation. The constitutive relationships of hereditary aging materials are obtained by applying the linear superposition to a generic stress/strain history as follows,

$$\varepsilon(t) = \int_0^t J_c(t, \tau) \cdot d\sigma(\tau) = \int_0^t J_c(t, \tau) \cdot \dot{\sigma}(\tau) d\tau \quad (4.1a)$$

$$\sigma(t) = \int_0^t G_s(t, \tau) \cdot d\varepsilon(\tau) = \int_0^t G_s(t, \tau) \cdot \dot{\varepsilon}(\tau) d\tau, \quad (4.1b)$$

where we assume that  $t_0 = 0$  days and the initial stress/deformation is also zero. Both expressions, (4.1a) and (4.1b), state the Boltzman superposition principle that, differently from the case of hereditary materials for which  $J(t, t_0) = J(t - t_0)$  and  $G(t, t_0) = G(t - t_0)$ ,

does not include convolution integrals.

The integrals in (4.1) are completely described as we introduce the functional class of creep and relaxation functions. Indeed, creep and relaxation functions characterize the material behavior and can be related through some mathematical manipulations on (4.1), yielding the first theorem of the linear aging hereditariness (Bažant, 1972),

$$J(t, t_0)G(t_0, t_0) + \int_{t_0}^t J(t, \tau) \frac{\partial G(\tau, t_0)}{\partial \tau} d\tau = 1. \quad (4.2)$$

The relationship in (4.2) is a Volterra integral equation of the second kind for the creep function  $J(t, t_0)$ . In other words, we can obtain the creep function through (4.2) as the relaxation function,  $G(t, t_0)$ , is known for different couples of time instants  $(t, t_0)$ . However, the estimation of the relaxation function by means of field experiments on existing structures is not so common in structural engineering. On the other hand, field tests for the estimation of the creep function are usually performed and the corresponding relaxation function can be obtained from the second theorem of the linear aging hereditariness,

$$G(t, t_0)J(t_0, t_0) + \int_{t_0}^t G(t, \tau) \frac{\partial J(\tau, t_0)}{\partial \tau} d\tau = 1. \quad (4.3)$$

The relationship in (4.3) represents a Volterra integral equation of the second kind for the relaxation function. Thus, we can obtain the relaxation function through (4.3) as the creep function is known for different couples of time instants  $(t, t_0)$ . It is important to observe that both the first and second theorem of the linear aging hereditariness entail to a very simple conjugation relation in the Laplace domain, i.e.  $\hat{J}(s)\hat{G}(s) = 1/s^2$ , as hereditary materials are considered.

A possible method to solve a Volterra integral equation of the second kind in time domain is the iterated-kernels method described in Tricomi (1957). For the case under investigation, a sequence of approximations for the relaxation function is obtained by applying the iterated-kernels method to Equation (4.3),

$$G^{(1)}(t, t_0) = \frac{1}{J(t_0, t_0)}, \quad (4.4a)$$

$$G^{(2)}(t, t_0) = \frac{1}{J(t_0, t_0)} \left( 1 - \int_{t_0}^t \frac{\partial J(\tau, t_0)}{\partial \tau} G^{(1)}(t, \tau) d\tau \right), \quad (4.4b)$$

$$\begin{aligned} & \dots\dots \\ & \mathbf{G}^{(k)}(t, t_0) = \frac{1}{J(t_0, t_0)} \left( 1 - \int_{t_0}^t \frac{\partial J(\tau, t_0)}{\partial \tau} \mathbf{G}^{(k-1)}(t, \tau) d\tau \right), \quad (4.4c) \\ & \dots\dots \end{aligned}$$

It is worth observing that the number of kernels required for a highly accurate approximation depends on the size of the time interval  $[t_0, t]$ . In other words, for small time intervals we need a number of kernels smaller than the one required for larger time intervals.

#### 4.2.2 Remarks on variable-order fractional calculus

In this section, we briefly recall the main ideas of fractional calculus, when the order of integration/differentiation is allowed to vary over time. Fractional operators with variable order can be successfully used to describe several physical phenomena, as discussed in Coimbra (2003), Tenreiro Machado et al. (2010), Sweilam and AL-Mrawm (2011), and Yajima and Yamasaki (2012), and among these we have the aging phenomenon, as discussed in Beltempo et al. (2017).

Lorenzo and Hartley (1998) first suggested the idea of variable-order fractional operators and several candidate definitions for variable-order fractional integrals are addressed in Lorenzo and Hartley (2002). Moreover, the definitions introduced in Lorenzo and Hartley (2002) for the variable-order integration may be formally extended to the idea of variable-order fractional differentiation as illustrated in Ingman and Suzdalnitsky (2005) and Valério and Da Costa (2011), respectively.

Before introducing fractional variable-order operators, we hereinafter recall the definition of Riemann-Liouville fractional integrals and derivatives of  $f(t)$  such that  $t \in [a, b] \subset \mathbb{R}$  (Podlubny, 1998),

$$\left( I_a^\beta f \right) (t) = \frac{1}{\Gamma(\beta)} \int_a^t \frac{f(\tau)}{(t-\tau)^{1-\beta}} d\tau \quad (4.5a)$$

$$\left( D_a^\beta f \right) (t) = \frac{f(a)}{\Gamma(1-\beta)(t-a)^\beta} + \frac{1}{\Gamma(1-\beta)} \int_a^t \frac{f'(\tau)}{(t-\tau)^\beta} d\tau, \quad (4.5b)$$

where the order  $\beta \in ]0, 1[$  is assumed a non-integer constant number, and the Euler-Gamma function  $\Gamma(z)$  is a generalization of the factorial function, since for  $z$  integer we have that  $\Gamma(z + 1) = z!$ . In the case of variable-order fractional calculus, Equations (4.5) become,

$$\left( I_a^{\beta(t)} f \right) (t) = \int_a^t \frac{(t - \tau)^{\beta(t, \tau) - 1}}{\Gamma(\beta(t, \tau))} f(\tau) d\tau \quad (4.6a)$$

$$\left( D_a^{\beta(t)} f \right) (t) = \frac{(t - a)^{-\beta(t, a)}}{\Gamma(1 - \beta(t, a))} f(a) + \int_a^t \frac{(t - \tau)^{-\beta(t, \tau)}}{\Gamma(1 - \beta(t, \tau))} f'(\tau) d\tau, \quad (4.6b)$$

in which the order of integration/differentiation is now function of the independent variable  $t$  and the integration/differentiation variable  $\tau$ .

There are different conditions of order variability that can be assigned to the fractional operators in (4.6), such as  $\beta(t, \tau) = \beta(t)$ ,  $\beta(t, \tau) = \beta(\tau)$  and  $\beta(t, \tau) = \beta(t - \tau)$ . In the following, we focus on the case  $\beta(t, \tau) = \beta(\tau)$ , since it well describe the aging phenomenon under investigation. However, the interested readers can find more details about the chosen case and the aforementioned cases in Lorenzo and Hartley (2002) and Valério and Da Costa (2011).

Thus, we redefine the Riemann-Liouville fractional integral and derivative as follows,

$$\left( I_a^{\beta(t)} f \right) (t) = \int_a^t \frac{(t - \tau)^{\beta(\tau) - 1}}{\Gamma(\beta(\tau))} f(\tau) d\tau \quad (4.7a)$$

$$\left( D_a^{\beta(t)} f \right) (t) = \frac{(t - a)^{-\beta(a)}}{\Gamma(1 - \beta(a))} f(a) + \int_a^t \frac{(t - \tau)^{-\beta(\tau)}}{\Gamma(1 - \beta(\tau))} f'(\tau) d\tau. \quad (4.7b)$$

Since  $\beta(\tau)$  at the exponent of  $(t - \tau)$  is not a function of  $(t - \tau)$ , both fractional operators in (4.7) become time variant; in this respect, an operator is said to be time invariant when the input  $f(t)$  produces a response  $y(t)$  and the input  $f(t + \Delta t)$  produces the response  $y(t + \Delta t)$  (Lorenzo and Hartley, 2002). Moreover, we also highlight that the fractional operators in (4.7) are not linear with respect to their order  $\beta(t)$ . Hence, the composition property, valid for constant orders, is no more applicable, i.e.,

$$I_+^{\beta(t)} I_+^{\alpha(t)} f(t) \neq \left( I_+^{\beta(t) + \alpha(t)} f \right) (t). \quad (4.8)$$

This last inequality strongly influences the evaluation of a fractional-order relaxation function through the iterated-kernels method described in Subsection 4.2.1. In particular, if the composition property was still suitable for the case  $\beta(t, \tau) = \beta(\tau)$ , the derived relaxation function would simply be a sum of Riemann-Liouville integrals with maximum order equal to  $k \cdot \beta$ , where  $k$  indicates the number of iterated kernels used to approximate the solution.

### 4.2.3 A fractional-hereditary aging constitutive law

A creep law that accounts for fractional variable-order operators was proposed for any aging material by Beltempo et al. (2017). In the following, we describe the main aspects characterizing this creep law and the relevant relaxation function to be involved into the derivation procedure of the fractional numerical integration scheme for structural analysis.

The creep phenomenon is described through a two-term function of power-law type, whose fractional-order nature is related to the choice of a real exponent. Furthermore, to account for the deterioration/improvement of material mechanical properties, the power-law exponent and other two material parameters are made dependent on the material age,  $t_0$ . Thus, the fractional-order creep function reads,

$$J_F(t, t_0) = \frac{1}{G_\beta(t_0)} + \frac{(t - t_0)^{\beta(t_0)}}{C_\beta(t_0)\Gamma(\beta(t_0) + 1)}, \quad (4.9)$$

where  $C_\beta(t_0)$ ,  $G_\beta(t_0)$  and  $\beta(t_0)$  are aging functions representative of the material mechanical characteristics. Moreover,  $G_\beta(t_0)$  and  $C_\beta(t_0)$  belong to  $\mathbb{R}^+$ ; while  $\beta(t_0) \in ]0, 1[$ . Thus, the creep function in (4.9) corresponds to the definition of a rheological model consisting of a time-varying spring and a variable-order fractional dashpot, as depicted in Figure 4.1.

As regards the derivation of the relevant relaxation function, it can be obtained by introducing the fractional-order creep function (4.9) in (4.4), i.e.  $J(t, t_0) = J_F(t, t_0)$ . However, the multiple integrals now involved in (4.4) are not so trivial to be solved,

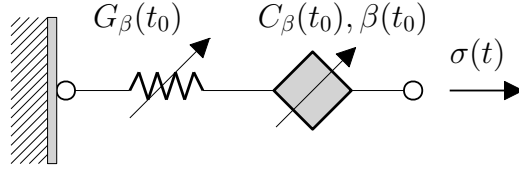


Figure 4.1: Variable-order fractional Maxwell model.

especially for large numbers assigned to the variable  $k$ . A possible way to reduce the complexity of such fractional order integrals is given by the introduction of the Grünwald-Letnikov approximation (Podlubny, 1998). Thus, we obtain the following expressions of the second and third iterated kernels and we can derive similar expressions for the successive kernels,

$$\mathbf{G}_F^{(2)}(t, t_0) = \mathbf{G}_\beta(t_0) - \frac{\mathbf{G}_\beta(t_0)h_1^{\beta(t_0)}}{C_\beta(t_0)} \left( \sum_{r_1=0}^{\bar{n}_1} (-1)^{r_1} \binom{-\beta(t_0)}{r_1} \mathbf{G}_\beta(t_0 + r_1 h_1) \right) \quad (4.10a)$$

$$\begin{aligned} \mathbf{G}_F^{(3)}(t, t_0) = & \mathbf{G}_\beta(t_0) - \frac{\mathbf{G}_\beta(t_0)h_1^{\beta(t_0)}}{C_\beta(t_0)} \left[ \left( \sum_{r_1=0}^{\bar{n}_1} (-1)^{r_1} \binom{-\beta(t_0)}{r_1} \mathbf{G}_\beta(t_0 + r_1 h_1) \right) + \right. \\ & - \left( \sum_{r_1=0}^{\bar{n}_1} (-1)^{r_1} \binom{-\beta(t_0)}{r_1} \frac{\mathbf{G}_\beta(t_0 + r_1 h_1)}{C_\beta(t_0 + r_1 h_1)} h_2^{\beta(t_0 + r_1 h_1)} \cdot \right. \\ & \left. \left. \cdot \left( \sum_{r_2=0}^{\bar{n}_2} (-1)^{r_2} \binom{-\beta(t_0 + r_1 h_1)}{r_2} \mathbf{G}_\beta(t_0 + r_1 h_1 + r_2 h_2) \right) \right) \right], \quad (4.10b) \end{aligned}$$

where,  $\bar{n}_i$  indicates the number of subintervals used to approximate the generic fractional integral and  $h_i$  is the interval amplitude. Moreover, according to Beltempo et al. (2017) we set a unique number of subintervals  $\bar{n}$  for all fractional integrals, thus,  $h_1 = h_2 = \dots = h_i = (t - t_0)/\bar{n} = h$  and  $\bar{n}_2 = \bar{n} - r_1$ ,  $\bar{n}_3 = \bar{n} - r_1 - r_2$ ,  $\bar{n}_4 = \bar{n} - r_1 - r_2 - r_3$ , and so on. As a result, it is possible to present a closed-form expression for the relaxation function,

$$\mathbf{G}_F^{(k)}(t, t_0) = \mathbf{g}_1(t_0) - \left[ \sum_{j=1}^{k-1} (-1)^{j-1} \mathbf{a}_1^j(t, t_0) \right], \quad (4.11)$$

which is proposed by referring to a generic  $k^{\text{th}}$  kernel approximation. Furthermore, Equation (4.11) is obtained by defining the column vector  $\mathbf{G}_\beta$  with dimension  $(\bar{n} + 1)$ ,

which includes the evaluation of the function  $\mathbf{G}_\beta$  at different time instants, and the upper-diagonal matrix  $\mathbf{L}$  with dimension  $(\bar{n}+1) \times (\bar{n}+1)$ , which represents the Grünwald-Letnikov terms. The extended form of vector  $\mathbf{G}_\beta$  and matrix  $\mathbf{L}$  reads,

$$\begin{aligned} \mathbf{G}_\beta &= [\mathbf{G}_\beta(t_0) \quad \mathbf{G}_\beta(t_0 + h) \quad \cdots \quad \mathbf{G}_\beta(t_0 + \bar{n}h)]^T = \\ &= [g_1(t_0) \quad g_2(t, t_0) \quad \cdots \quad g_{\bar{n}+1}(t, t_0)]^T \end{aligned} \quad (4.12)$$

$$\mathbf{L} = \begin{bmatrix} \frac{h^{\beta(t_0)} \mathbf{G}_\beta(t_0)}{C_\beta(t_0)} (-1)^0 \binom{-\beta(t_0)}{0} & \cdots & \frac{h^{\beta(t_0)} \mathbf{G}_\beta(t_0)}{C_\beta(t_0)} (-1)^{\bar{n}} \binom{-\beta(t_0)}{\bar{n}} \\ & \ddots & \vdots \\ & & \frac{h^{\beta(t_0 + \bar{n}h)} \mathbf{G}_\beta(t_0 + \bar{n}h)}{C_\beta(t_0 + \bar{n}h)} (-1)^0 \binom{-\beta(t_0 + \bar{n}h)}{0} \end{bmatrix}. \quad (4.13)$$

Moreover, the matrix product between the generic  $j^{\text{th}}$  power of  $\mathbf{L}$  and  $\mathbf{G}_\beta$  is indicated with the following notation,

$$\mathbf{L}^j \cdot \mathbf{G}_\beta = [a_1^j(t, t_0) \quad a_2^j(t, t_0) \quad \cdots \quad a_{\bar{n}+1}^j(t, t_0)]^T. \quad (4.14)$$

The effectiveness of the presented constitutive law was proved in Beltempo et al. (2017), through a representative application to a medium strength concrete and the relevant comparison with Model B3 (Bažant and Baweja, 2000).

### 4.3 Structural analysis in presence of fractional-order aging hereditariness

In this section, we present a fractional-order numerical integration scheme, which relies on the viscoelastic formulation proposed by Carini et al. (1995b). The main novelty of the presented scheme is the introduction of a fractional-order aging kernel, i.e. the relaxation function (4.11), into the viscoelastic formulation. Moreover, a time-discontinuous Galerkin scheme is hereinafter illustrated by employing linear shape functions for the time discretization, previously used in this context (Larsson et al., 2015). With regard to the spatial discretization, for the sake of clarity, the classical shape functions related to

the Bernoulli-Navier beam theory are considered. However, the same FE formulation can be extended to a generic 3D body.

### 4.3.1 The FE formulation

The FE formulation is based on the classical assumptions of Bernoulli-Navier and first-order beam theories. Thus, the object of the study is a beam, whose kinematics is uniquely described by  $u(x; t)$  and  $v(x; t)$ , which define the horizontal and vertical displacements of the cross-section centroid, respectively. In this respect, the rotation  $\theta(x; t)$  can be obtained through the relation  $\theta(x; t) = \partial v(x; t)/\partial x$ . Moreover, we assume that the beam is straight and its centroidal axis develops along the  $x$  axis.

The starting equation of the FE formulation, hereinafter presented for a generic aging kernel, is the extremal principle proposed in Carini et al. (1995b),

$$\begin{aligned}
 F[u, v] = \sum_{e=1}^{n^e} \left\{ \frac{1}{2} \int_{t_0}^{t_f} \int_0^{\ell^e} G^e(x; t_0, t_0) \left[ A^e(x) \left( \frac{\partial \hat{u}^e(x; t)}{\partial x} \right)^2 + \right. \right. \\
 \left. \left. + J^e(x) \left( \frac{\partial^2 \hat{v}^e(x; t)}{\partial x^2} \right)^2 \right] dx dt - \int_{t_0}^{t_f} \int_0^{\ell^e} p^e(x; t) \hat{u}^e(x; t) dx dt + \right. \\
 \left. - \int_{t_0}^{t_f} \int_0^{\ell^e} q^e(x; t) \hat{v}^e(x; t) dx dt \right\}, \quad (4.15)
 \end{aligned}$$

where  $\sum_{e=1}^{n^e}$  indicates the sum over elements,  $G^e(x; t_0, t_0)J^e(x)$  represents the flexural stiffness of the beam element, and  $G^e(x; t_0, t_0)A^e(x)$  the relevant axial stiffness. As regards  $\hat{u}^e(x; t)$  and  $\hat{v}^e(x; t)$ , they are the fictitious elastic displacements of the generic element  $e$ , which are obtained through an auxiliary elastic problem. The elastic response of this auxiliary problem is derived by invoking the stationarity of the total potential energy principle that under the hypotheses of Bernoulli-Navier and first-order beam theories can

be written as follows,

$$\begin{aligned}
F_{TPE}[\hat{u}, \hat{v}] = \sum_{e=1}^{n^e} \left\{ \frac{1}{2} \int_0^{\ell^e} G^e(x; t_0, t_0) \left[ A^e(x) \left( \frac{\partial \hat{u}^e(x; t)}{\partial x} \right)^2 + \right. \right. \\
\left. \left. + J^e(x) \left( \frac{\partial^2 \hat{v}^e(x; t)}{\partial x^2} \right)^2 \right] dx - \int_0^{\ell^e} \hat{p}^e(x; t) \hat{u}^e(x; t) dx + \right. \\
\left. - \int_0^{\ell^e} \hat{q}^e(x; t) \hat{v}^e(x; t) dx \right\}, \tag{4.16}
\end{aligned}$$

where  $\hat{p}^e$  and  $\hat{q}^e$  indicates two fictitious loads, which are both functions of the relaxation kernel,  $G^e(x; t, t_0)$ , and of the unknown displacement field,  $\mathbf{u}^e(x; t) = [u^e(x; t) \quad v^e(x; t)]^T$ .

The expressions of the fictitious loads follow,

$$\begin{aligned}
\hat{p}^e &= -\frac{\partial}{\partial x} \left( G^e(x; t, t_0) A^e(x) \frac{\partial u^e(x; t)}{\partial x} \right) - \frac{\partial}{\partial x} \int_{t_0}^t G^e(x; t, \tau) A^e(x) \frac{\partial du^e(x; \tau)}{\partial x} \\
\hat{q}^e &= -\frac{\partial^2}{\partial x^2} \left( G^e(x; t, t_0) J^e(x) \frac{\partial^2 v^e(x; t)}{\partial x^2} \right) - \frac{\partial^2}{\partial x^2} \int_{t_0}^t G^e(x; t, \tau) J^e(x) \frac{\partial^2 dv^e(x; \tau)}{\partial x^2}. \tag{4.17}
\end{aligned}$$

We underline that both loads include an additional integral over time, which is related to their dependence on the viscoelastic constitutive relationship. Furthermore, the presence of the real displacements,  $u(x; t)$  and  $v(x; t)$ , in the functional  $F[u, v]$  (4.15) has become now more evident.

As regards the derivation of the relevant FE technique, we need first to introduce a discretization in space and in time in both  $F[u, v]$  (4.15) and  $F_{TPE}[\hat{u}, \hat{v}]$  (4.16). The notation used for the two discretizations is described in the following and, for clarity, is referred to the real displacement field only. However, a similar notation is used for the discretization of the fictitious displacements.

The collection of the spatial shape functions, referred to each node of the mesh, into the matrix  $\mathbf{N}^e(x)$  and the collection of the relevant nodal Degrees of Freedom (DoFs) into

the vector  $\mathbf{r}^e(t)$  entail that the displacement vector  $\mathbf{u}^e(x; t)$  can be expressed as follows,

$$\mathbf{u}^e(x; t) = \begin{bmatrix} \mathbf{n}_u^e & \mathbf{0}^T \\ \mathbf{0}^T & \mathbf{n}_v^e \end{bmatrix} \cdot \begin{bmatrix} \mathbf{r}_u^e \\ \mathbf{r}_v^e \end{bmatrix} = \mathbf{N}^e(x) \mathbf{r}^e(t) = \mathbf{N}^e(x) \mathbf{A}^e \boldsymbol{\alpha}(t), \quad (4.18)$$

where  $\mathbf{A}^e$  denotes the coordinate transformation matrix and  $\boldsymbol{\alpha}(t)$  the vector of nodal DoFs of the assembled structure in the global reference system. Additionally,  $\mathbf{n}_u^e$  collects the axial shape functions,  $[n_1(x) \ n_2(x)]^T$ , while  $\mathbf{n}_v^e$  collects the flexural shape functions,  $[n_3(x) \ n_4(x) \ n_5(x) \ n_6(x)]^T$ ;  $\mathbf{r}_u^e = [r_1 \ r_2]^T$  defines the axial DoFs and  $\mathbf{r}_v^e = [r_3 \ r_4 \ r_5 \ r_6]^T$  the flexural DoFs. Hence, as depicted in Figure 4.2, beam finite elements with three spatial DoFs per node, horizontal displacement, transversal displacement and rotation, are considered. Furthermore, the classical shape functions associated to the DoFs of each generic FE read,

$$\begin{aligned} n_1(x) &= 1 - x/L & n_2(x) &= x/L \\ n_3(x) &= 1 - 3 \cdot x^2/L^2 + 2 \cdot x^3/L^3 & n_4(x) &= x - 2 \cdot x^2/L + x^3/L^2 \\ n_5(x) &= 3 \cdot x^2/L^2 - 2 \cdot x^3/L^3 & n_6(x) &= x^3/L^2 - x^2/L. \end{aligned} \quad (4.19)$$

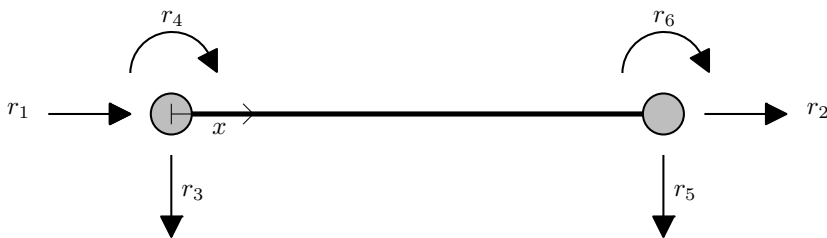


Figure 4.2: The beam finite element and its DoFs.

The time discretization is instead introduced by replacing the vector  $\boldsymbol{\alpha}(t)$  with the product of time shape functions, collected into the matrix  $\mathbf{M}(t)$ , and time DoFs, collected

into the column vector  $\mathbf{b}$ . Hence,

$$\boldsymbol{\alpha}(t) = \begin{bmatrix} \mathbf{m}_1^T & & \\ & \ddots & \\ & & \mathbf{m}_{ns}^T \end{bmatrix} \cdot \begin{bmatrix} \mathbf{b}_1 \\ \vdots \\ \mathbf{b}_{ns} \end{bmatrix} = \mathbf{M}(t)\mathbf{b}, \quad (4.20)$$

where  $ns$  indicates the number of spatial DoFs and  $\mathbf{b}_1 \cdots \mathbf{b}_{ns}$  are column vectors with dimension  $nt$ , i.e. the number of time DoFs assigned to each spatial degree of freedom. In what follows, each spatial degree of freedom is discretized in time using two linear shape functions. Thus,  $nt$  is set equal to 2 and for a generic time interval we set,

$$\mathbf{m}_1 = \cdots = \mathbf{m}_{ns} = \mathbf{m} = [m_1 \quad m_2]^T = \begin{bmatrix} (t_i - t) & (t - t_{i-1}) \\ (t_i - t_{i-1}) & (t_i - t_{i-1}) \end{bmatrix}^T, \quad (4.21)$$

$$\mathbf{b}_s = [b_s^{i-1} \quad b_s^i]^T \quad s = 1, \dots, ns \quad (4.22)$$

where  $t_{i-1}$  and  $t_i$  indicate the initial and the final time instant; likewise,  $b_s^{i-1}$  and  $b_s^i$  represent the DoFs relevant to the time instants  $t_{i-1}$  and  $t_i$ , respectively.

The introduction of the aforementioned discretizations in the functional  $F_{TPE}[\hat{u}, \hat{v}]$  and the condition of stationarity entails the following system of equations,

$$\mathbf{K}\hat{\boldsymbol{\alpha}} = \left( \sum_{e=1}^{n^e} \mathbf{A}^{eT} \mathbf{k}^e \mathbf{A}^e \mathbf{G}^e \right) \mathbf{b} = \mathbf{H}\mathbf{b}, \quad (4.23)$$

where  $\mathbf{k}^e$  is the elementary stiffness operator,  $\mathbf{K}$  is the stiffness operator of the assembled structure and  $\mathbf{H}$  is a matrix depending on both the relaxation kernel and time shape functions. Moreover,

$$\mathbf{G}^e = \frac{G^e(x; t, t_0)}{G^e(x; t_0, t_0)} \mathbf{M}(t_0) + \int_{t_0}^t \frac{G^e(x; t, \tau)}{G^e(x; t_0, t_0)} d\mathbf{M}(\tau), \quad (4.24)$$

which, particularized to the case of the fractional-order aging kernel illustrated in (4.11), reads,

$$\mathbf{G}^e = \frac{g_1(t_0) - \left[ \sum_{j=1}^{k-1} (-1)^{j-1} a_1^j(t, t_0) \right]}{G^e(t_0, t_0)} \mathbf{M}(t_0) + \int_{t_0}^t \frac{g_1(\tau) - \left[ \sum_{j=1}^{k-1} (-1)^{j-1} a_1^j(t, \tau) \right]}{G^e(t_0, t_0)} d\mathbf{M}(\tau),$$

(4.25)

where we have assumed constant mechanical properties along the element axis  $x$ . The fractional-order nature of (4.25) is now evident due to the Grünwald-Letnikov approximations involved in  $\left[ \sum_{j=1}^{k-1} (-1)^{j-1} \mathbf{a}_1^j(t, t_0) \right]$  and  $\left[ \sum_{j=1}^{k-1} (-1)^{j-1} \mathbf{a}_1^j(t, \tau) \right]$  (Podlubny, 1998). For additional details about the derivation of the linear system in (4.23), the interested reader may refer to Carini et al. (1995b).

Hence, the obtained fictitious vector of nodal DoFs,  $\hat{\alpha} = \mathbf{K}^{-1} \mathbf{H} \mathbf{b}$ , can be substituted into the energy principle (4.15) in the discretized form,

$$F[\mathbf{b}] = \frac{1}{2} \mathbf{b}^T \left\{ \int_{t_0}^{t_f} \mathbf{H}^T \mathbf{K}^{-1} \mathbf{H} dt \right\} \mathbf{b} - \mathbf{b}^T \left\{ \int_{t_0}^{t_f} \mathbf{H}^T \mathbf{K}^{-1} \mathbf{f} dt \right\} = \frac{1}{2} \mathbf{b}^T \mathbf{L} \mathbf{b} - \mathbf{b}^T \mathbf{g}, \quad (4.26)$$

where,

$$\mathbf{L} = \int_{t_0}^{t_f} \mathbf{H}^T \mathbf{K}^{-1} \mathbf{H} dt \quad \mathbf{g} = \int_{t_0}^{t_f} \mathbf{H}^T \mathbf{K}^{-1} \mathbf{f} dt. \quad (4.27)$$

The minimum of (4.26) is reached when  $\mathbf{b}$  represents the solution of the following linear system,

$$\mathbf{L} \mathbf{b} = \mathbf{g}. \quad (4.28)$$

More precisely,  $\mathbf{L}$  defines the extended stiffness matrix and  $\mathbf{g}$  is the extended vector of the equivalent nodal forces. As a result, the unknown displacement field can be derived using (4.18) and (4.20).

The presented method can also be applied to subintervals by using a step-by-step type procedure. This implies the use of a reduced number of time DoFs over each subinterval, e.g. two as in (4.21), as well as, a smaller dimension of matrices to be employed. More precisely, the time interval  $[t_0, t_f]$  is subdivided into  $n$  subintervals defined through the sequence  $t_0, t_1, \dots, t_n \equiv t_f$ .

Considering the generic time interval  $] t_{i-1}, t_i ]$ ,  $F(u, v)$  in (4.26) becomes,

$$\begin{aligned} F[\mathbf{b}_i] &= \frac{1}{2} \mathbf{b}_i^T \left\{ \int_{t_{i-1}}^{t_i} \mathbf{H}_i^T \mathbf{K}^{-1} \mathbf{H}_i dt \right\} \mathbf{b}_i - \mathbf{b}_i^T \left\{ \int_{t_{i-1}}^{t_i} \mathbf{H}_i^T \mathbf{K}^{-1} \left( \mathbf{f} - \sum_{p=1}^{i-1} \mathbf{b}_p \mathbf{H}_p \right) dt \right\} = \\ &= \frac{1}{2} \mathbf{b}_i^T \mathbf{L}_i \mathbf{b}_i - \mathbf{b}_i^T (\mathbf{g}_i - \mathbf{h}_i), \end{aligned} \quad (4.29)$$

where the inversion of the elastic stiffness operator has to be carried out only once, since it remains the same for all time steps; conversely, the operators  $\mathbf{L}_i$  and  $\mathbf{g}_i - \mathbf{h}_i$  must be calculated at every time step, where the vector  $\mathbf{h}_i$  accounts for the past history. Moreover, according to (4.29), in order to estimate displacements at the generic time instant  $t_i$ , the estimation of  $\mathbf{H}$  at the current time interval  $i$  and at all previous time intervals  $p$  is also needed. For the generic time step  $] t_{i-1}, t_i ]$  and considering the case of the fractional-order kernel (4.11), the operator  $\mathbf{H}_i$  can be evaluated as follows,

$$\begin{aligned} \mathbf{H}_i &= \sum_{e=1}^{n^e} \left( \mathbf{A}^{eT} \mathbf{k}^e \mathbf{A}^e \mathbf{G}_i^e \right) \\ \mathbf{G}_i^e &= \frac{\mathbf{g}_1(t_0) - \left[ \sum_{j=1}^{k-1} (-1)^{j-1} \mathbf{a}_1^j(t_i, t_0) \right]}{\mathbf{G}^e(t_0, t_0)} \mathbf{M}(t_0) + \int_{t_{i-1}}^{t_i} \frac{\mathbf{g}_1(\tau) - \left[ \sum_{j=1}^{k-1} (-1)^{j-1} \mathbf{a}_1^j(t_i, \tau) \right]}{\mathbf{G}^e(t_0, t_0)} d\mathbf{M}(\tau), \end{aligned} \quad (4.30)$$

and all previous operators  $\mathbf{H}_p$  can be evaluated as follows,

$$\begin{aligned} \mathbf{H}_p &= \sum_{e=1}^{n^e} \left( \mathbf{A}^{eT} \mathbf{k}^e \mathbf{A}^e \mathbf{G}_p^e \right) \\ \mathbf{G}_p^e &= \int_{t_{p-1}}^{t_p} \frac{\mathbf{g}_1(\tau) - \left[ \sum_{j=1}^{k-1} (-1)^{j-1} \mathbf{a}_1^j(t_i, \tau) \right]}{\mathbf{G}^e(t_0, t_0)} d\mathbf{M}(\tau). \end{aligned} \quad (4.31)$$

Thus, the vector  $\mathbf{b}_i$  represents the solution of the linear system  $\mathbf{L}_i \mathbf{b}_i = \mathbf{g}_i - \mathbf{h}_i$  for the generic time instant  $t_i$ .

The time marching procedure described above has been here particularized for the 1-dimensional case and for the case of a fractional-order aging kernel. A general overview of the step-by-step procedure is instead provided in Carini et al. (1995a).

## 4.4 Convergence analysis

In this section, we investigate the convergence of the proposed fractional-order numerical scheme with the aid of a model problem, whose exact solution is well known. The *a posteriori* accuracy analyses mainly focus on the evaluation of the global truncation error by setting different values of significant variables, listed hereinafter. With regard to the stability of the numerical integration scheme, readers may refer to Carini et al. (1995a), where the stability of the FE formulation was proven for a generic 3D body through an energy approach. Finally, important considerations about the computational time required to end each creep analysis are also stated.

### 4.4.1 The model problem

In order to study the accuracy of the fractional numerical integration scheme, we consider the model problem depicted in Figure 4.3. The clamped beam is made of a medium strength concrete, whose mechanical properties are summarized in Table 4.1; while the relevant expressions to be assigned to  $C_\beta(t_0)$ ,  $G_\beta(t_0)$  and  $\beta(t_0)$  are reported in Appendix 4.A. Moreover, the clamped beam is characterized by a unitary cross-section area and length,  $A = 1\text{m}^2$  and  $L = 1\text{m}$ , respectively; and we suppose to apply a compressive load of 1000 kN, after 1000 days from concrete casting.

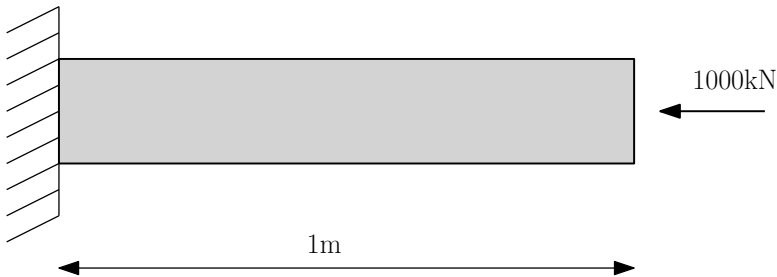


Figure 4.3: The model problem.

One of the main advantage of considering the problem depicted in Figure 4.3 is that it corresponds to the definition of the creep function; therefore, the strain undergone by

Table 4.1: Mechanical properties of the medium-strength concrete specimen for the 2D frame structure.

$\bar{f}_c$ - cylinder compression strength at 28 days [MPa]	43
$E_{28}$ - Young modulus at 28 days [MPa]	31043
$w/c$ - water-cement ratio	0.54
$a/c$ - aggregate-cement ratio	5.10
$c$ - cement content [kg/m <sup>3</sup> ]	343.04
$t'$ - drying time [days]	7
$\gamma$ - specific weight [kN/m <sup>3</sup> ]	25

the clamped beam due to the load applied at  $t_0$  is well know and can be exactly evaluated through Equation (4.9). The value of the creep function to be mostly used as reference solution by the following accuracy analyses is  $J_F(10000, 1000) = 6.57 \cdot 10^{-5}$ ; hence, we set  $t_0 = 1000$  days and  $t_f = 10000$  days. Moreover, the whole time-dependent response from  $t_0 = 1000$  days to  $t_f = 10000$  days is also going to be detected with the evaluation of the global error at several time instants within the interval [1000, 10000] days.

#### 4.4.2 Results

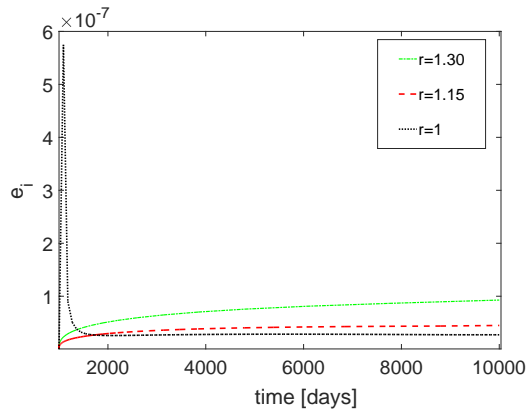
The accuracy of the integration scheme, characterized by the fractional-order viscous kernel presented in Subsection 4.2.3, is mainly influenced by the combination of several variables: i) the number of Gaussian quadrature points  $nG$ , used to approximate the external integrals in (4.27) and the internal integral in (4.24); ii) the number of subintervals

$n$ , in which we subdivide the whole time interval  $[t_0, t_f]$ ; iii) the ratio  $r$  between the current and previous time-step size  $\Delta t_i/\Delta t_{i-1} = r$ ; iv) the number of iterated kernels  $k$ , used to approximate the fractional-order relaxation function; lastly, v) the number of terms  $\bar{n}$ , used for the Grünwald-Letnikov approximation. Furthermore, additional considerations are needed for variables  $r$  and  $\bar{n}$ , i.e.  $r$  is kept constant within the whole creep analysis, and  $\bar{n}$  is set at most equal to 170 due to a working-precision limit imposed by the software MATLAB.

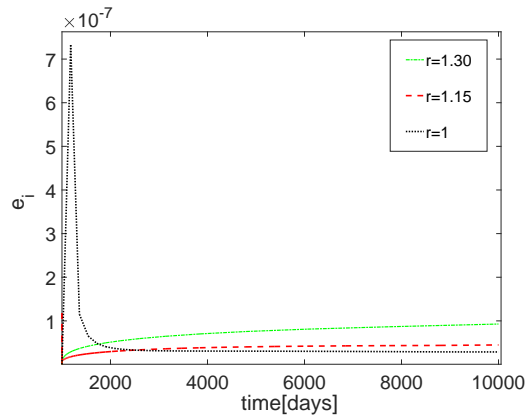
To investigate the accuracy of the proposed FE method, we first assign different values to the aforementioned variables and then, we evaluate the global truncation error  $\|\mathbf{e}_i\|$  by means of  $\|\mathbf{s}(t_i) - \mathbf{s}_i\|$ , where  $\mathbf{s}(t_i)$  is the reference solution and  $\mathbf{s}_i$  indicates the approximate solution, both estimated at the generic time instant  $t_i$ . In the end, after an attempt analysis of the accuracy and the computational cost, we select the best value for each variable. All results, presented in the following, were obtained in MATLAB by means of an Intel Core i7, 12 GB of RAM, and 2.60 GHz of CPU frequency.

Preliminary results focus on the choice of the best ratio  $r$  by fixing  $nG = 4$ ,  $k = 30$ , and  $\bar{n} = 170$  and by varying the number of subintervals  $n$ . Figure 4.4 includes the relevant plots, in which the global truncation error is measured along the  $y$  axis, whilst, the  $x$  axis represents the time interval  $[t_0, t_f]$ . In all graphs, we can observe that  $\|\mathbf{e}_i\|$  is very small, which proves the efficiency of the proposed FE fractional method. However, if the long-term response is investigated, the lowest error can be reached by setting  $r = 1$  and  $n = 100$ . Conversely, if we are interested in the short-term structural response, the best solution is given by  $r = 1.15$  and  $n = 100$ . Another important observation about Figure 4.4 regards the initial error trend, which is firstly increasing and after a time interval, whose size mainly depends on  $n$ , starts to decrease. The main reason is that all terms of vector  $\mathbf{h}$  in (4.29) are updated at every time step; thus, where the solution trend is smoother, i.e. in long term, the estimated error is smaller.

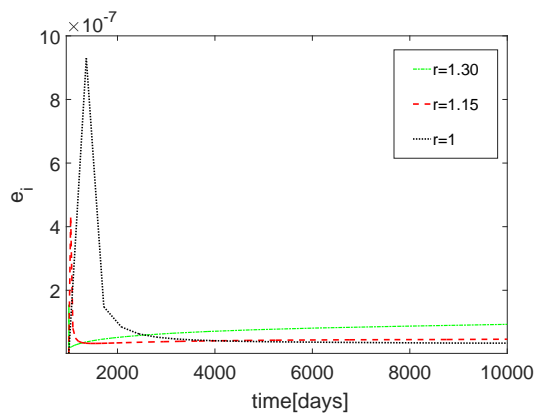
Figure 4.5 depicts another important plot, which analyzes the long-term global truncation error, i.e.  $t_f = 10000$ , by varying the number of subintervals  $n$  and the number of Gaussian points  $nG$ . Moreover, we set  $r = 1$ , according to the considerations on Figure



(a) Global truncation error for  $n = 100$ .



(b) Global truncation error for  $n = 50$ .



(c) Global truncation error for  $n = 25$ .

Figure 4.4: Global truncation error estimated from  $t_0 = 1000$  days to  $t_f = 10000$  days by varying  $n$  and  $r$ , with  $nG = 4$ ,  $k = 30$  and  $\bar{n} = 170$ .

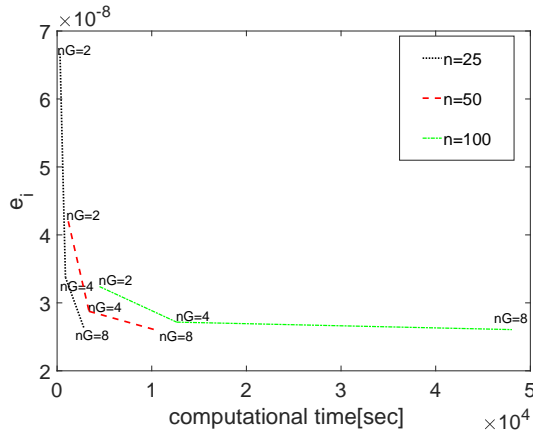


Figure 4.5: Global truncation error estimated at  $t_f = 10000$  days by varying the number of subintervals and the number of Gaussian quadrature points, with  $r = 1$ ,  $k = 30$  and  $\bar{n} = 170$ .

4.4,  $k = 30$ , and  $\bar{n} = 170$ . The computational time required to perform the creep analysis is also detected in Figure 4.5, since it may represent a decisive factor for choosing the best values of  $n$  and  $nG$ . Indeed, the graph shows that 25 subintervals and 8 Gaussian points are sufficient to reach the long-term most accurate solution with the lowest computational time. A similar accuracy is given by 8 Gaussian points and 100 subintervals, but the relevant computational burden is around ten times the computational burden obtained by setting  $nG = 8$  and  $n = 25$ .

Another interesting plot, depicted in Figure 4.6, focuses on the Grünwald-Letnikov approximation. More precisely, we set  $k = 30$  and we compare the most closest cases of Figure 4.5, i.e.  $nG = 8$  and  $n = 25$ ,  $nG = 4$  and  $n = 50$ , and  $nG = 2$  and  $n = 100$ . Once more, the most accurate solution is reached when  $nG = 8$  and  $n = 25$ ; moreover, as expected, when we consider  $\bar{n} = 170$ . Similar considerations can be drawn from the graph of Figure 4.7, in which we set  $\bar{n} = 170$  and we vary the number of iterated kernels  $k$  from 20 to 50. However, conversely from Figure 4.6, the computational burden required for the FE creep analysis does not change considerably by varying the number of iterated kernels. Another important aspect to highlight is that the solution obtained for  $k = 50$  is

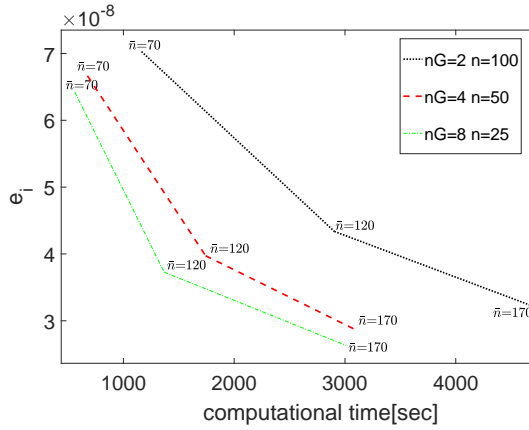


Figure 4.6: Global truncation error estimated at  $t_f = 10000$  days by varying the number of subintervals, the number of Gaussian quadrature points, and the number of terms involved into the Grünwald-Letnikov approximation, with  $r = 1$  and  $k = 30$ .

very close to the solution obtained for  $k = 30$ ; thus, the best value of iterated kernels to be used to approximate the relaxation function from  $t_0 = 1000$  days to  $t_f = 10000$  days is 30.

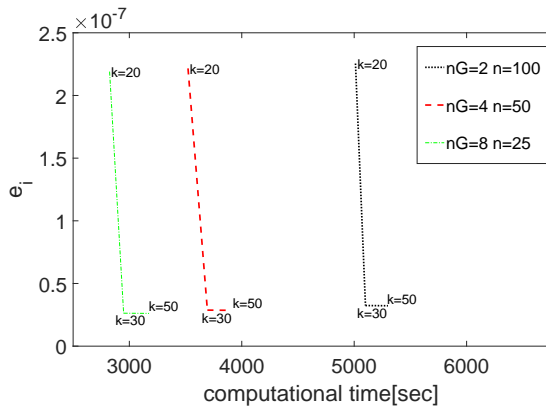


Figure 4.7: Global truncation error estimated at  $t_f = 10000$  days by varying the number of subintervals, the number of Gaussian quadrature points and the number of iterated Kernels, with  $r = 1$  and  $\bar{n} = 170$ .

After a careful analysis of all plots illustrated in this section, we can conclude that to

investigate the long-term behavior of concrete structures by means of the FE fractional-order formulation within the time interval [1000, 10000] days, 8 Gaussian points are sufficient together with a number of subintervals equal to 25. Moreover, the time-step size can be kept constant along the whole creep analysis, i.e.  $r = 1$ , and an acceptable accuracy for the fractional-order relaxation function is reached when  $\bar{n} = 170$  and  $k = 30$ . The computational time required to perform the relevant creep analysis is around 3000 seconds with a relative percentage error at 10000 days equal to 0.04%. A careful reader can note that no indication about the convergence order of the proposed method has been provided mainly because the fractional-order relaxation kernel (4.11) is affected by approximations, i.e. the iterated-kernels and Grünwald-Letnikov methods, both described in Subsection 4.2.3; thus, the estimation of the convergence order obtained by reducing time-subinterval sizes would not result accurate.

## **4.5 Representative numerical examples**

The proposed fractional-order numerical integration scheme is herein applied to study the short- and long-term behavior of two representative concrete structures. The first example is a frame structure and investigates the applicability of the proposed scheme to statically undetermined structures. The second example explores the structural behavior of a prestressed concrete viaduct, which, according to Bažant and Baweja (2000), belongs to the class of structures highly sensitive to time-dependent phenomena.

### **4.5.1 A 2D frame structure**

The frame structure depicted in Figure 4.8 consists of two horizontal beams and three fixed columns, all characterized by a square cross-section with sides 0.6 m, for a total number of ten finite elements. The structural behavior is analyzed under the assumption that concrete exhibits the same behavior in tension and compression, and the relevant material parameters are listed in Appendix 4.A.

Two load histories are considered for this creep analysis; the first includes two hori-

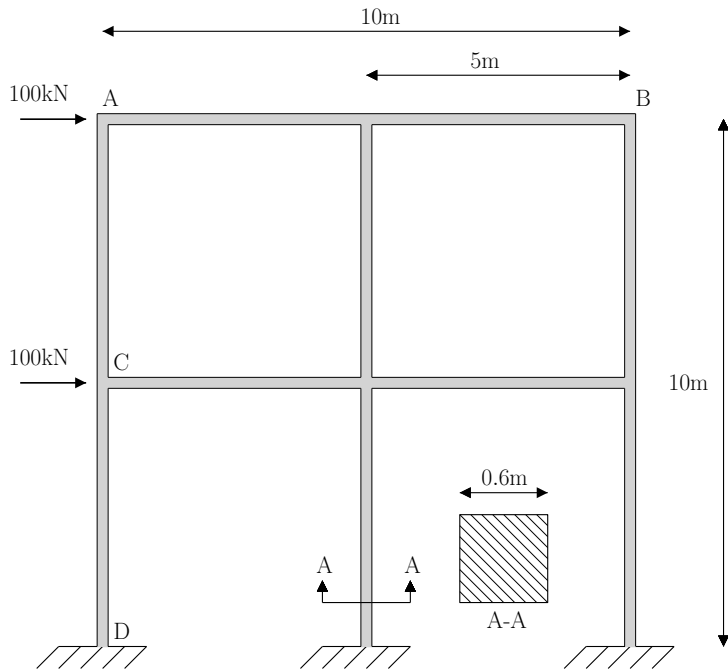


Figure 4.8: A 2D statically indeterminate frame.

zontal loads of  $100\text{kN}$  each applied at 1000 days to nodes  $A$  and  $C$ , the second considers the same loads applied at 4600 days. Figure 4.9 refers to the first load history and shows the time evolution of the horizontal displacement at node  $B$ , for the cases  $r = 1$  and  $r = 1.15$  and fixed Gaussian points, set to 8, and fixed subintervals, chosen equal to 25. As expected, the long-term difference in terms of accuracy between the two cases is very small; conversely, at short term, the case  $r = 1.15$  is more accurate. As regards the computational time, it is almost the same for the two cases and close to 23000 seconds.

Figure 4.10 shows the time evolution of the horizontal displacement at point  $B$  for the case of multiple load history, and we consider the following cases: i)  $nG = 8$  and  $n = 25$ ; ii)  $nG = 2$  and  $n = 100$ ; iii)  $nG = 2$  and  $n = 25$ ; where  $n = 25$  corresponds to  $\Delta t = 360$  days and  $n = 100$  refers to  $\Delta t = 90$  days. As expected, the difference in terms of accuracy among the three cases is very small, especially for the long-term solution. Conversely, as regards the short-term response, the accuracy is strongly influenced by the choice of the number of subintervals; thus, the best result is reached when  $nG = 2$  and

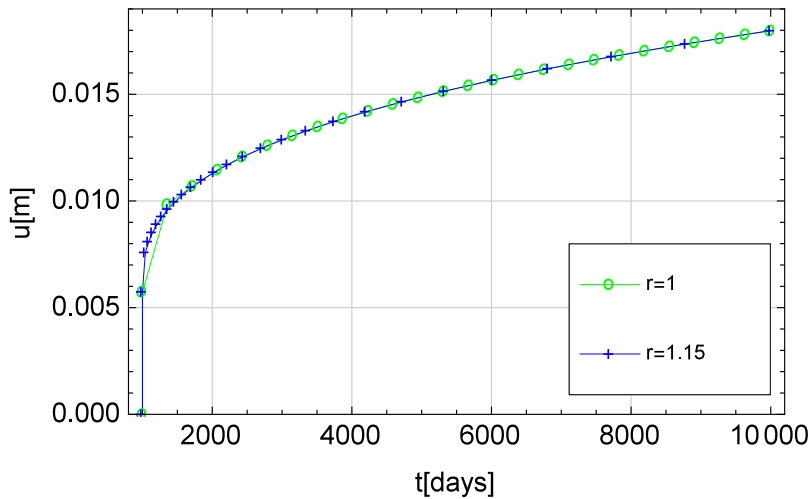


Figure 4.9: Time evolution of the horizontal displacement at node  $B$ , for two horizontal loads equal to  $100\text{kN}$  applied at 1000 days to nodes  $A$  and  $C$ .

$n = 100$ . However, another important aspect to be taken into account is the computational time required to carry out each creep analysis. The worst case is  $nG = 2$  and  $n = 100$  characterized by a computational time equal to 48016 seconds; the case  $nG = 8$  and  $n = 25$  requires 31530 seconds; in the end, the case  $nG = 2$  and  $n = 25$  is performed within the lowest computational time equal to 3177 seconds. Due to the small difference in terms of accuracy and the huge difference in terms of computational time between cases iii) and ii), we may conclude that the choice of 2 Gaussian points and 25 subintervals represents a good compromise for an efficient study of the time-dependent response of the structure depicted in Figure 4.8, with a reasonable computational burden.

#### 4.5.2 A prestressed concrete box girder

In what follows, we investigate both the short- and long-term behavior of the main span of the Colle Isarco viaduct, which is an Italian segmental prestressed concrete box girder belonging to the Highway A22. The viaduct was built between 1969 and 1971 and designed by engineers Bruno and Lino Gentilini (Gentilini and Gentilini, 1972).

Overall, the Colle Isarco viaduct comprises two structurally independent decks, the

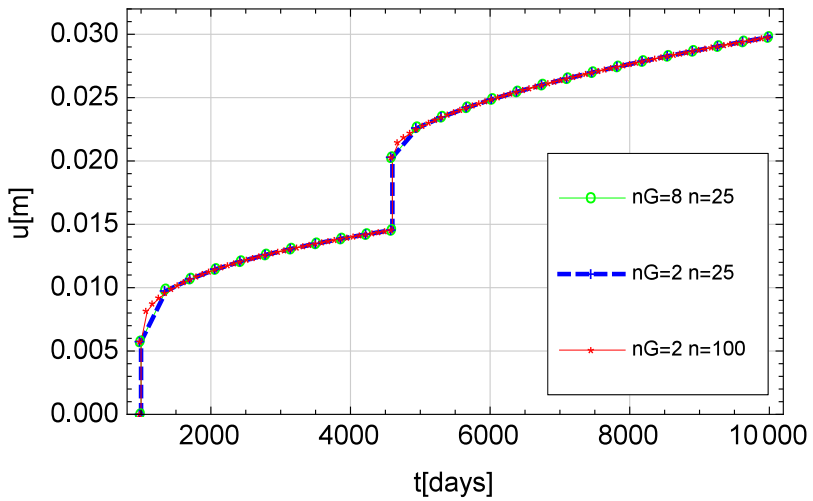


Figure 4.10: Time evolution of the horizontal displacement at node *B*, caused by two horizontal loads of  $100\text{kN}$  in nodes *A* and *C* applied at 1000 days and 4600 days, respectively.

so-called North and South carriageways, with 13 spans, for a total length of 1028.2 m. The main span of the viaduct, 163 m long, consists of two symmetric reinforced concrete Niagara box girders, which support a suspended beam of 45 m, as depicted in Figure 4.11. Each box girder ends with a 59m-long cantilever, counterbalanced by a back arm with a length of 91 m. The thickness of the top slab of the box girder is constant and equal to 0.26 m, while, the bottom slab varies from 0.99 m to 0.12 m.



Figure 4.11: The Colle Isarco viaduct.

Due to the symmetric configuration that characterizes the main span of the Colle Isarco viaduct, we limit the investigation to the time-dependent behavior of the South box girder and we account for the effects produced by the weight of the suspended beam through a vertical force applied at the end of each cantilever. Figure 4.12 schematically depicts the South box girder and its static configuration, which consists of a roller at node 6 and a pin at node 31. Moreover, we indicate with: i)  $Q_1 = 904.55$  kN and  $Q_{48} = 922.03$  kN the vertical forces introduced to model the self weight of the suspended beam; ii)  $q_{r1} = 38.82$  kN/m and  $q_{r2} = 39.57$  kN/m the sustained loads related to road-pavement finishes.

As regards the mesh generation, we subdivide the whole box girder into 47 beam elements, as the number of segments assembled during construction stages. Hence, 48 nodes, with three DoFs per node, characterize the FE model, for a total number of 144 DoFs, as shown in Figure 4.13. In order to account for the variability of the cross-section depth, we assign to each beam element a different value of area and momentum of inertia, both evaluated as mean value of the geometrical characteristics at the two beam ends. The geometry assigned to each beam element is summarized in Table 4.3, where  $L^e$  indicates the length of each single element,  $h^e$  its height,  $d^e$  the double of the volume-to-surface ratio,  $A^e$  the area, and  $J^e$  the momentum of inertia. More precisely, the quantity  $d^e$  is here introduced since it is determinant for the evaluation of the material parameters,  $\beta(t_0)$ ,  $C_\beta(t_0)$  and  $G_\beta(t_0)$ , as discussed in the following.

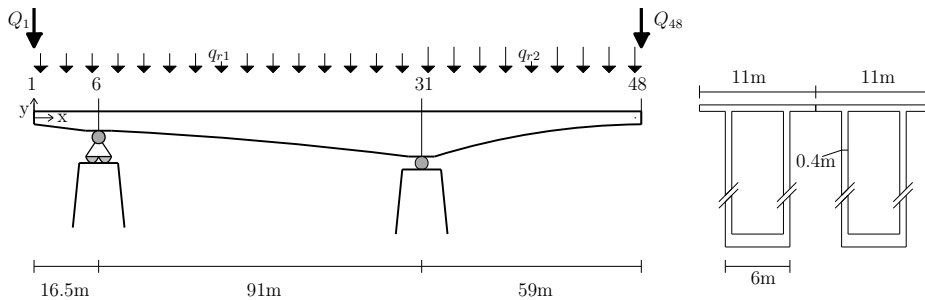


Figure 4.12: The static configuration of the main box girder and its generic cross section.

Table 4.2: Mechanical properties of the medium-strength concrete for the prestressed concrete box girder.

$\bar{f}_c$ - cylinder compression strength at 28 days [MPa]	43
$E_{28}$ - Young modulus at 28 days [MPa]	31043
$w/c$ - water-cement ratio	0.4
$a/c$ - aggregate-cement ratio	3.09
$c$ - cement content $[\text{kg}/\text{m}^3]$	525
$t'$ - drying time [days]	7
$\gamma$ - specific weight $[\text{kN}/\text{m}^3]$	25

The box girder is made of a medium strength concrete, whose mechanical properties are summarized in Table 4.2, and the expressions of the relevant parameters,  $\beta(t_0)$ ,  $C_\beta(t_0)$  and  $G_\beta(t_0)$ , are listed in Appendix 4.B. It is important to highlight that, due to the variability of the cross-section depth, the current parameters have been derived as function of both the material age and the volume-to-surface ratio, which represents a novelty with respect to the procedure used to derive the parameters in Beltempo et al. (2017). In fact, if the cross-section geometry is constant along the whole structure, as the example of Figure 4.8, the parameters are a function of the material age only; conversely, if the cross-section depth varies, in order to properly account for the shrinkage, the dependence on the volume-to-surface ratio has to be evident. In the latter case, the best-fitting procedure described in Beltempo et al. (2017), is performed by varying the material age for different values of volume-to-surface ratio.

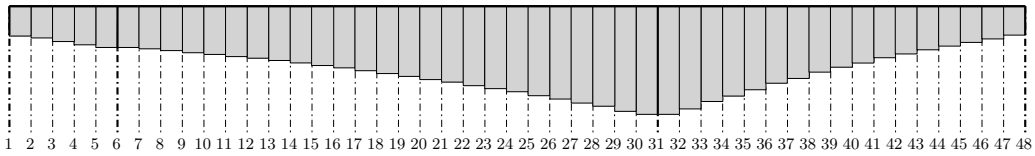


Figure 4.13: Mesh used for the creep analysis of the Colle Isarco viaduct.

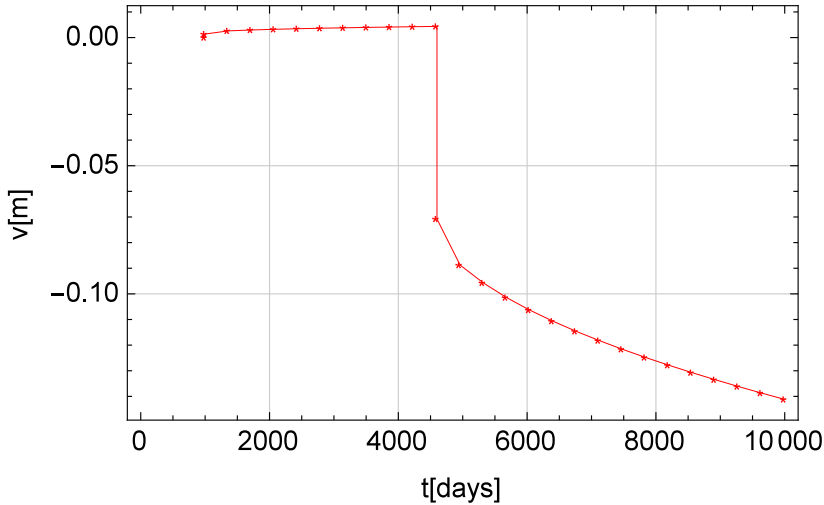


Figure 4.14: Time evolution of the vertical displacement at node 48, where negative values entail downward displacements.

As regards the load sustained by the structure, we consider: i) the self weight, modeled through vertical forces and moments applied at each mesh node; ii) the weight of the two suspended beams,  $Q_1$  and  $Q_{48}$ ; iii) the sustained load due to road-pavement finishes,  $q_{r1}$  and  $q_{r2}$ ; iv) the prestressing accounted for by means of horizontal forces and transposition moments applied at the end of each bar. In total, we model 266 Dywidag ST 85/105 threaded bars with a diameter of 32mm and a nominal tensile strength of 1030 MPa. The jacking tension applied to each bar is 720 MPa; additionally, we assume 15% as percentage of initial losses. The loads assigned to each node of mesh are collected in Table 4.4, where  $N^n$  indicates the generic horizontal nodal force,  $V^n$  the generic vertical nodal force and  $M^n$  the generic concentrated moment.

The creep analysis of the prestressed structure under investigation is performed by

considering the self weight and prestressing applied at  $t_0 = 1000$  days, and the weight of the suspended beams and road pavement finishes applied at  $t_0 = 4600$  days. Figure 4.14 shows the time evolution of the vertical displacement at node 48, for the case  $r = 1$ ,  $nG = 2$ , and  $n = 25$ , which, as previously discussed, represents the most efficient combination in terms of computational burden. Moreover, we can notice that until 4600 days the measured displacements are almost null and the prestressing prevails over the self weight; the observed trend is lightly growing, indeed. Conversely, after 4600 days the displacement approaches 10 cm with a change of trend. Furthermore, the time required to perform the whole creep analysis is about 16145 seconds. This solution time may appear significant for a structure relatively simple. Nonetheless, as underlined in Beltempo et al. (2018), solvers of creep problems for standard FE software may entail significant errors if complex load histories are not properly superposed. Conversely, the formulation proposed in Section 4.3 properly takes into account the combination of multiple load histories.

Table 4.3: Geometrical characteristics for the FEs of the box girder.

$FE$	$L^e$ [m]	$h^e$ [m]	$d^e$ [cm]	$A^e$ [m <sup>2</sup> ]	$J^e$ [m <sup>4</sup> ]
1	4.50	2.82	36	5.70	6.45
2	4.00	3.32	38	6.44	10.73
3	4.00	3.81	40	7.19	16.25
4	3.00	4.23	42	7.76	21.69
5	1.00	4.41	42	7.96	24.07
6	2.25	4.44	42	7.99	24.53
7	4.00	4.51	42	8.09	25.63
8	4.00	4.60	43	8.24	27.23
9	4.00	4.73	43	8.40	29.32
10	4.00	4.88	43	8.59	31.87
11	4.00	5.02	44	8.87	35.02
12	4.00	5.19	45	9.21	38.96
13	4.00	5.39	46	9.58	43.59

$FE$	$L^e$ [m]	$h^e$ [m]	$d^e$ [cm]	$A^e$ [m <sup>2</sup> ]	$J^e$ [m <sup>4</sup> ]
14	4.00	5.59	47	9.92	48.56
15	4.00	5.80	47	10.25	53.81
16	4.00	6.03	48	10.58	59.76
17	4.00	6.28	49	10.91	66.42
18	4.00	6.55	49	11.24	74.21
19	4.00	6.87	49	11.60	83.69
20	4.00	7.21	49	11.97	94.54
21	4.00	7.55	50	12.35	106.58
22	4.00	7.91	50	12.74	119.83
23	3.00	8.23	50	13.10	132.62
24	3.00	8.52	50	13.44	145.29
25	3.00	8.84	50	13.80	159.77
26	3.00	9.18	50	14.17	176.07
27	3.00	9.54	51	14.53	193.71
28	3.00	9.91	50	14.88	212.64
29	3.00	10.28	51	15.28	234.00
30	3.75	10.70	52	16.03	263.89
31	3.75	10.63	52	15.92	259.25
32	3.00	10.08	50	14.99	221.57
33	3.00	9.59	50	14.43	194.32
34	3.00	9.10	50	13.86	169.57
35	3.00	8.63	49	13.29	147.07
36	3.00	8.16	49	12.76	127.21
37	3.00	7.69	48	12.22	109.08
38	3.00	7.22	48	11.66	92.50
39	4.00	6.67	47	11.01	75.40

$FE$	$L^e$ [m]	$h^e$ [m]	$d^e$ [cm]	$A^e$ [m <sup>2</sup> ]	$J^e$ [m <sup>4</sup> ]
40	4.00	6.04	47	10.30	58.48
41	4.00	5.41	46	9.59	44.15
42	4.00	4.78	45	8.86	32.21
43	4.00	4.20	44	8.13	22.86
44	4.00	3.67	42	7.45	16.02
45	4.00	3.21	40	6.74	10.92
46	3.25	2.88	37	6.01	7.35
47	3.00	2.70	36	5.60	5.64

Table 4.4: Loads assigned to each node of the box-girder mesh at  $t_0 = 1000$  and  $t_0 = 4600$  days.

$n$	$t_0 = 1000$			$t_0 = 4600$
	$N^n$ [kN]	$V^n$ [kN]	$M^n$ [kNm]	$V^n$ [kN]
1	3841.13	-320.79	-3269.42	-991.90
2	9602.81	-642.88	-2940.57	-164.99
3	10563.10	-681.78	-12321.54	-155.28
4	10563.10	-650.84	-15498.11	-135.87
5	8642.53	-390.66	-14419.76	-77.64
6	5761.69	-324.18	-9782.21	-63.08
7	0.00	-629.40	-185.56	-121.31
8	2880.84	-816.97	15015.77	-155.28
9	1920.56	-832.19	38739.16	-155.28
10	960.28	-849.60	11125.36	-155.28
11	5761.69	-872.98	23947.23	-155.28
12	2880.84	-903.85	2824.28	-155.28
13	6721.97	-939.34	3463.14	-155.28

$n$	$N^n$ [kN]	$V^n$ [kN]	$M^n$ [kNm]	$V^n$ [kN]
14	2880.84	-974.94	-7301.05	-155.28
15	6721.97	-1008.44	3416.71	-155.28
16	11523.38	-1041.47	-30998.23	-155.28
17	960.28	-1074.62	-25590.66	-155.28
18	4801.41	-1107.30	-14725.67	-155.28
19	1920.56	-1141.66	-12558.42	-155.28
20	960.28	-1178.09	-29514.87	-155.28
21	3841.13	-1215.52	-34544.41	-155.28
22	-2880.84	-1254.08	-17261.69	-155.28
23	9602.81	-1127.94	-45626.75	-135.87
24	-960.28	-994.98	-34258.28	-116.46
25	-1440.42	-1021.23	-37121.21	-116.46
26	-3360.98	-1048.83	-21308.86	-116.46
27	-960.28	-1076.52	-28642.67	-116.46
28	9602.81	-1103.01	-47133.44	-116.46
29	5761.69	-1131.08	-29006.04	-116.46
30	9602.81	-1324.33	-50515.55	-131.08
31	0.00	-1131.08	3.13	-146.98
32	-3841.13	-1308.50	19673.21	-133.55
33	-1920.56	-1103.42	9559.36	-118.71
34	-7682.25	-1060.92	35144.36	-118.71
35	-4801.41	-1018.07	21011.74	-118.71
36	-4801.41	-976.60	18851.08	-118.71
37	-5761.69	-936.56	21245.58	-118.71
38	-4801.41	-895.55	16575.93	-118.71
39	-4801.41	-987.99	15085.48	-138.50

$n$	$N^n$ [kN]	$V^n$ [kN]	$M^n$ [kNm]	$V^n$ [kN]
40	-7682.25	-1065.76	21642.04	-158.28
41	-1920.56	-994.56	4790.81	-158.28
42	-7682.25	-922.26	15767.71	-158.28
43	-4801.41	-849.16	9292.97	-158.28
44	-9602.81	-778.76	14222.68	-158.28
45	-11523.38	-709.46	12965.56	-158.28
46	-9602.81	-581.24	8421.77	-143.44
47	-15364.50	-454.27	7331.84	-123.66
48	-6721.97	-210.11	3601.51	-981.38

## 4.6 Conclusions

The use of fractional-calculus for the characterization of the time-dependent behavior exhibited by aging materials has very recent bases (Beltempo et al., 2017); thus, its effective use still needs a wide investigation. On this basis, the main aims of the present work are: i) to provide a numerical integration scheme compatible with a fractional-order aging kernel; ii) to perform a relevant convergence analysis thorough a model problem; iii) to test the proposed method on realistic structures.

Along these lines, in Section 4.2, a fractional-order constitutive law, which includes both the hereditariness and the aging of the material, is illustrated, with a particular attention on the derivation of the relevant relaxation function. The resulting relaxation function is then introduced into the FE formulation presented in Section 4.3, leading to a numerical integration scheme, whose main novelty relates to the fractional-order aging kernel. The convergence of the derived fractional-order integration scheme is investigated in Section 4.4 by means of an *a posteriori* accuracy analysis on a model problem, i.e. a clamped beam made of a medium strength concrete and subjected to a unitary stress at the free end, for which the exact viscoelastic solution is known. Moreover, by choosing

different values of significant variables, like the number of Gaussian quadrature points and subintervals, we find that the best solution in terms of accuracy and computational time is reached by setting  $nG = 8$  and  $n = 25$ , i.e.  $\Delta t = 360$  days, for a creep analysis performed within  $[1000, 10000]$  days. Similar considerations are drawn by applying the fractional-order integration to more complex structures. More precisely, we consider a frame structure, characterized by ten beam finite elements, and a prestressed concrete box girder, consisting of 47 finite elements. By means of these two case studies, we also show that the proposed numerical method is suitable for the analysis of the long-term behavior of concrete structures subjected to multiple load histories.

As further development of this research work, the proposed fractional-order numerical integration scheme and the relevant convergence analysis can be extended to the case of 2D and 3D bodies.

#### 4.A Aging functions for a medium strength concrete for the 2D frame structure

The trends of parameters  $\beta(t_0)$ ,  $G_\beta(t_0)$ , and  $C_\beta(t_0)$ , characterizing the medium strength concrete, whose mechanical properties are summarized in Table 4.1, were derived in Beltempo et al. (2017) through a best-fitting procedure with Model B3 (Bažant and Prasannan, 1989), which represents one of the most widely used creep models for structural concretes. Then, from the results of the best-fitting procedure, specific functions of the material age  $t_0$  were derived and assigned to each parameter, i.e.,

$$\begin{aligned} \beta(t_0) = & \Theta(T_2 - t_0) \cdot f_1^\beta(t_0) + \Theta(t_0 - T_2) \cdot f_2^\beta(t_0) + \Theta(t_0 - T_3) \cdot f_3^\beta(t_0) \\ & - \Theta(t_0 - T_3) \cdot f_2^\beta(t_0) \end{aligned} \quad (4.32a)$$

$$\begin{aligned} G_\beta(t_0) = & \Theta(T_2 - t_0) \cdot f_1^{G_\beta}(t_0) + \Theta(t_0 - T_2) \cdot f_2^{G_\beta}(t_0) + \Theta(t_0 - T_3) \cdot f_3^{G_\beta}(t_0) \\ & - \Theta(t_0 - T_3) \cdot f_2^{G_\beta}(t_0) \end{aligned} \quad (4.32b)$$

$$\begin{aligned} C_\beta(t_0) = & \Theta(T_4 - t_0) \cdot f_1^{C_\beta}(t_0) + \Theta(t_0 - T_4) \cdot f_2^{C_\beta}(t_0) + \Theta(t_0 - T_3) \cdot f_3^{C_\beta}(t_0) \\ & - \Theta(t_0 - T_3) \cdot f_2^{C_\beta}(t_0) \end{aligned} \quad (4.32c)$$

where  $\Theta(\cdot)$  indicates the Heaviside step function and  $T_1 = 10$  days,  $T_2 = 100$  days,  $T_3 = 1000$  days,  $T_4 = 200$  days. Moreover, in the following we list all functions needed to define  $\beta(t_0)$ ,  $C_\beta(t_0)$ , and  $G_\beta(t_0)$ , i.e.

$$f_1^\beta(t_0) = -3.10 \cdot 10^{-6}(t_0 - T_1)^2 + 7.99 \cdot 10^{-4}(t_0 - T_1) + 0.199 \quad (4.33a)$$

$$\begin{aligned} f_2^\beta(t_0) = & -1.11 \cdot 10^{-18}(t_0 - T_2)^6 + 3.63 \cdot 10^{-15}(t_0 - T_2)^5 + \\ & -4.81 \cdot 10^{-12}(t_0 - T_2)^4 + 3.39 \cdot 10^{-9}(t_0 - T_2)^3 + \\ & -1.45 \cdot 10^{-6}(t_0 - T_2)^2 + 4.68 \cdot 10^{-4}(t_0 - T_2) + f_1^\beta(T_2) \end{aligned} \quad (4.33b)$$

$$\begin{aligned} f_3^\beta(t_0) = & -6.41 \cdot 10^{-24}(t_0 - T_3)^6 + 1.53 \cdot 10^{-19}(t_0 - T_3)^5 + \\ & -1.46 \cdot 10^{-15}(t_0 - T_3)^4 + 7.17 \cdot 10^{-12}(t_0 - T_3)^3 + \\ & -2.02 \cdot 10^{-8}(t_0 - T_3)^2 + 4.36 \cdot 10^{-5}(t_0 - T_3) + f_2^\beta(T_3) \end{aligned} \quad (4.33c)$$

$$f_1^{G_\beta}(t_0) = 8674.33 \cdot \ln(t_0) + 7379.72 \quad (4.33d)$$

$$\begin{aligned}
f_2^{\text{G}\beta}(t_0) = & -3.03 \cdot 10^{-15}(t_0 - T_2)^6 + 9.65 \cdot 10^{-11}(t_0 - T_2)^5 + \\
& -1.24 \cdot 10^{-7}(t_0 - T_2)^4 + 8.45 \cdot 10^{-5}(t_0 - T_2)^3 + \\
& -3.41 \cdot 10^{-2}(t_0 - T_2)^2 + 7.72(t_0 - T_2) + f_1^{\text{G}\beta}(T_2)
\end{aligned} \tag{4.33e}$$

$$\begin{aligned}
f_3^{\text{G}\beta}(t_0) = & 3.06 \cdot 10^{-20}(t_0 - T_3)^6 - 6.47 \cdot 10^{-16}(t_0 - T_3)^5 + \\
& + 5.89 \cdot 10^{-12}(t_0 - T_3)^4 - 3.50 \cdot 10^{-8}(t_0 - T_3)^3 + \\
& + 2.07 \cdot 10^{-4}(t_0 - T_3)^2 - 1.06(t_0 - T_3) + f_2^{\text{G}\beta}(T_3)
\end{aligned} \tag{4.33f}$$

$$f_1^{\text{C}\beta}(t_0) = -0.37(t_0 - T_1)^2 + 931(t_0 - T_1) + 74753.76 \tag{4.33g}$$

$$\begin{aligned}
f_2^{\text{C}\beta}(t_0) = & 2.32 \cdot 10^{-13}(t_0 - T_4)^6 - 3.65 \cdot 10^{-10}(t_0 - T_4)^5 + \\
& -5.71 \cdot 10^{-8}(t_0 - T_4)^4 + 4.9 \cdot 10^{-4}(t_0 - T_4)^3 + \\
& -0.55(t_0 - T_4)^2 + 767.75(t_0 - T_4) + f_1^{\text{C}\beta}(T_4)
\end{aligned} \tag{4.33h}$$

$$\begin{aligned}
f_3^{\text{C}\beta}(t_0) = & -5.62 \cdot 10^{-17}(t_0 - T_3)^6 + 1.2 \cdot 10^{-12}(t_0 - T_3)^5 + \\
& -1.06 \cdot 10^{-8}(t_0 - T_3)^4 + 4.74 \cdot 10^{-5}(t_0 - T_3)^3 + \\
& -0.11(t_0 - T_3)^2 + 437.57 \cdot 10^{-3}(t_0 - T_3) + f_2^{\text{C}\beta}(T_3)
\end{aligned} \tag{4.33i}$$

#### 4.B Aging functions for a medium strength concrete for the prestressed concrete box girder

The trends of parameters  $\beta(t_0)$ ,  $G_\beta(t_0)$ , and  $C_\beta(t_0)$ , characterizing the medium strength concrete, whose mechanical properties are summarized in Table 4.2, were derived by means of a best-fitting procedure with Model B3 (Bažant and Prasannan, 1989). Then, from the results of the best-fitting procedure, specific functions of both the material age  $t_0$  and the double of the volume-to-surface ratio  $d$  [cm] were derived and assigned to each parameter, i.e.,

$$\beta(t_0, d) = \Theta(T_3 - t_0) \cdot f_1^\beta(t_0, d) + \Theta(t_0 - T_3) \cdot f_2^\beta(t_0, d) \quad (4.34a)$$

$$G_\beta(t_0, d) = \Theta(T_3 - t_0) \cdot f_1^{G_\beta}(t_0, d) + \Theta(t_0 - T_3) \cdot f_2^{G_\beta}(t_0, d) \quad (4.34b)$$

$$C_\beta(t_0, d) = G_\beta(t_0, d) \cdot \left[ \Theta(T_3 - t_0) \cdot f_1^{C_\beta}(t_0, d) + \Theta(t_0 - T_3) \cdot f_2^{C_\beta}(t_0, d) \right] \quad (4.34c)$$

where  $\Theta(\cdot)$  indicates the Heaviside step function and  $T_3 = 1000$  days. Moreover, in the following we list all functions needed to define  $\beta(t_0, d)$ ,  $C_\beta(t_0, d)$ , and  $G_\beta(t_0, d)$ , i.e.

$$f_1^\beta(t_0, d) = (-1.96558 \cdot 10^{-5} d^2 + 2.565926 \cdot 10^{-3} d + 8.6357846 \cdot 10^{-3}) \cdot \ln(t_0) + \\ + (5.81780 \cdot 10^{-5} d^2 - 9.6176929 \cdot 10^{-3} d + 0.165214) \quad (4.35a)$$

$$f_2^\beta(t_0, d) = (-7.74 \cdot 10^{-28} d^2 + 3.2342 \cdot 10^{-26} d - 7.315605 \cdot 10^{-24})(t_0 - T_3)^6 + \\ + (9.269253 \cdot 10^{-24} d^2 + 1.664701 \cdot 10^{-22} + \\ + 1.600193 \cdot 10^{-19})(t_0 - T_3)^5 + (5.015519 \cdot 10^{-20} d^2 + \\ - 1.582950 \cdot 10^{-17} d - 1.301324 \cdot 10^{-15})(t_0 - T_3)^4 + \\ + (-1.507718 \cdot 10^{-15} d^2 + 2.1069845 \cdot 10^{-13} d + \\ + 3.9951503 \cdot 10^{-12})(t_0 - T_3)^3 + (1.0247320 \cdot 10^{-11} d^2 + \\ - 1.3035123 \cdot 10^{-9} d + 2.7571166 \cdot 10^{-9})(t_0 - T_3)^2 + \\ + (-1.6538236 \cdot 10^{-8} d^2 + 2.550901 \cdot 10^{-6} d +$$

$$- 3.436172 \cdot 10^{-6})(t_0 - T_3) + f_1^\beta(T_3) \quad (4.35b)$$

$$\begin{aligned} f_1^{G\beta}(t_0, d) = & (5.9995665 \cdot 10^{-2} d^3 - 9.240464 \cdot d^2 + 472.951599 \cdot d + \\ & - 6768.5842585) \cdot \ln(t_0) + (-0.4718785 \cdot d^3 + 72.97975 \cdot d^2 + \\ & - 3768.0474637 \cdot d + 100564.2030785) \end{aligned} \quad (4.35c)$$

$$\begin{aligned} f_2^{G\beta}(t_0, d) = & (-1.031235 \cdot 10^{-24} d^3 + 1.60602535 \cdot 10^{-22} d^2 - 8.501484 \cdot 10^{-21} d + \\ & + 1.1461851 \cdot 10^{-19})(t_0 - T_3)^6 + (3.111534 \cdot 10^{-20} d^3 + \\ & - 4.8630255 \cdot 10^{-18} d^2 + 2.59303 \cdot 10^{-16} d + \\ & - 3.2769143 \cdot 10^{-15})(t_0 - T_3)^5 + (-3.839225 \cdot 10^{-16} d^3 + \\ & + 6.023999 \cdot 10^{-14} d^2 - 3.2344107 \cdot 10^{-12} d + \\ & + 3.88004719 \cdot 10^{-11})(t_0 - T_3)^4 + (2.500146 \cdot 10^{-12} d^3 + \\ & - 3.9374909 \cdot 10^{-10} d^2 + 2.1270574 \cdot 10^{-8} d + \\ & - 2.4473893 \cdot 10^{-7})(t_0 - T_3)^3 + (-9.8578135 \cdot 10^{-9} d^3 + \\ & + 1.5486765 \cdot 10^{-6} d^2 - 8.3512766 \cdot 10^{-5} d + \\ & + 9.449694 \cdot 10^{-4})(t_0 - T_3)^2 + (2.8760292 \cdot 10^{-5} d^3 + \\ & - 4.4871794 \cdot 10^{-3} d^2 + 0.2398676 \cdot d + \\ & - 2.8320368)(t_0 - T_3) + f_1^{G\beta}(T_3) \end{aligned} \quad (4.35d)$$

$$\begin{aligned} f_1^{C\beta}(t_0, d) = & (-1.0184577 \cdot 10^{-2} d^2 + 1.3001315 \cdot d - 20.0444338) \cdot \ln(t_0) + \\ & + (5.337443 \cdot 10^{-2} d^2 - 6.9691459 \cdot d + 111.581249) \end{aligned} \quad (4.35e)$$

$$\begin{aligned} f_2^{C\beta}(t_0, d) = & (-4.87905 \cdot 10^{-25} d^2 + 5.5879957 \cdot 10^{-23} d + \\ & - 3.182039 \cdot 10^{-21})(t_0 - T_3)^6 + (3.003096 \cdot 10^{-21} d^2 + \\ & - 7.3016134 \cdot 10^{-19} d + 6.4229665 \cdot 10^{-17})(t_0 - T_3)^5 + \\ & + (1.0981881 \cdot 10^{-16} d^2 - 2.5132916 \cdot 10^{-15} d + \\ & - 4.523209 \cdot 10^{-13})(t_0 - T_3)^4 + (-1.7499694 \cdot 10^{-12} d^2 + \\ & + 1.0752874 \cdot 10^{-10} d + 3.74069998 \cdot 10^{-10})(t_0 - T_3)^3 + \end{aligned}$$

$$\begin{aligned}
& + (-1.544642 \cdot 10^{-10} \mathbf{d}^3 + 3.023302 \cdot 10^{-8} \mathbf{d}^2 + \\
& - 1.7781695 \cdot 10^{-6} \mathbf{d} + 2.567407 \cdot 10^{-5})(t_0 - T_3)^2 + \\
& + (-1.634351 \cdot 10^{-5} \mathbf{d}^2 + 0.002419626 \cdot \mathbf{d} + \\
& - 0.0413951)(t_0 - T_3) + f_1^{C\beta}(T_3)
\end{aligned} \tag{4.35f}$$



## Chapter 5

### Summary, conclusions and future perspectives

#### 5.1 Summary

Many concrete structures, among which long-span prestressed concrete box-girders, very tall buildings, cooling towers, and dams, reveal, during their service life, increasing deformations, sometimes inexplicable through models and techniques presented in technical standards. Recent studies on this topic found that one of the major cause of such an apparently anomalous behavior relates to the high sensitivity of these structures to time-dependent phenomena like creep and shrinkage. This thesis concentrates on the study of these phenomena and on the strong influence that creep and shrinkage may have on the short- and long-term behavior of concrete structures, with particular attention to long-span prestressed concrete box-girders. Thus, the following research activities were conducted: i) the development of a FE model, based on the refined creep and shrinkage Model B3, and its application to a representative prestressed concrete box-girder; ii) the development of a novel creep constitutive law with the aid of Model B3; and iii) the implementation of a FE scheme characterized by the proposed fractional-order aging kernel and its application to realistic concrete structures. A more detailed summary about the aforementioned research activities follows.

The FE model illustrated in Chapter 2 for the study of long-span prestressed concrete box-girders relies on an energetic formulation for linear viscoelastic problems (Carini et al., 1995b), properly integrated with the approximate relaxation function of Model B3 (Bažant and Baweja, 2000). Model B3 is selected among other creep models available

in literature mainly because of its success at predicting the future behavior of structures highly sensitive to creep (Bažant et al., 2012); moreover, it includes an additional component, whose creep effect never tends to an asymptotic value. With regard to the presented FE model, it is derived from an extension of the well-known total potential energy principle, discretized in space through the classical FE technique and in time by means of linear shape functions. The resulting 1D FE scheme is then validated on a representative concrete structure susceptible to creep, i.e. the Colle Isarco viaduct, which is faithfully modeled keeping into account all changes of sustained loads from its construction to the last maintenance work. In order to estimate the deflection trend at the tip of the viaduct longest cantilever, a creep analysis is also performed from 1969 up to 2040, and the relevant results are compared to the monitoring field data. Finally, important considerations about the model efficiency are stated in relation to its implementation in a decision support system.

The second part of this thesis focuses on the development of a novel creep constitutive law with the following main requirements: being characterized by a simpler form than Model B3; and being a function of both the load duration (hereditariness) and the material age (aging). Along these bases, the presented creep model is developed within the framework of variable-order fractional calculus. Indeed, there are many advantages related to the use of fractional operators in the context of linear viscoelasticity, among which the description of both creep and relaxation through simple laws; however, this and many other advantages were deduced from studies on hereditary materials. Thus, the research work presented in Chapter 3 mainly aims to explore the applicability of such operators to more complex cases, like aging materials. The proposed creep constitutive law consists of a real-order power law, function of the load duration  $(t - t_0)$ , and three aging parameters,  $C_\beta(t_0)$ ,  $\beta(t_0)$  and  $G_\beta(t_0)$ , properly derived through a best-fitting procedure with Model B3. Specifically, the inverse of  $G_\beta(t_0)$  aims to describe the time-dependent compliance of concrete, and both  $\beta(t_0)$  and  $C_\beta(t_0)$  are related to the change of pore shapes and to the re-arranging of material microstructure. Then, in order to derive the relevant relaxation function, an efficient procedure, based on the iterated-kernels method and the

Grünwald-Letnikov approximation, is also illustrated. Finally, interesting comparisons with the Model B3 creep and relaxation functions are shown and discussed.

The last research activity presented in this thesis focuses on the development of a numerical integration scheme to be used with the aforementioned fractional-order constitutive model. The derivation procedure is illustrated in Chapter 4 and starts with an extension of the total potential energy principle (Carini et al., 1995b), defined under the assumptions of Euler-Bernoulli and first-order beam theories. The relevant FE scheme is then arranged by employing specific spatial and time discretizations; and through an auxiliary elastic problem, solved with a step-by-step procedure, the resolutive linear system with displacement unknowns is derived. More precisely, the spatial shape functions, utilized for the relevant discretization, are the classical ones involved in a 1D elastic problem; while the time shape functions for the time discretization are borrowed from the discontinuous Galerkin method. With regard to the investigation of the FE-formulation efficiency, a detailed convergence analysis is performed by means of a simple model problem, for which the exact creep solution is well known. Eventually, two more complex case studies subjected to multiple load histories are investigated, including the central span of the Colle Isarco viaduct.

The major results obtained in each chapter of this thesis are summarized in the next section.

## **5.2 Conclusions**

This thesis aims to examine the short- and long-term behavior of creep-sensitive concrete structures through the development of FE models and their use with suitable constitutive laws. The first developed 1D FE model includes the refined creep and shrinkage Model B3 (Bažant and Baweja, 2000) and is utilized to predict the behavior of a representative concrete structure, the Colle Isarco viaduct in Italy. Specifically, the deflection at the tip of the longest viaduct cantilever and its variation over years are investigated, obtaining satisfactory results both in terms of accuracy and simulation time.

There is indeed very good agreement between the model results and the monitoring field data, especially during the last maintenance work of 2014. Such a high level of accuracy is actually surprising, considering the simple assumptions at the bases of the model, i.e. Euler-Bernoulli and first-order beam theories. Furthermore, thanks to these specific simple assumptions the simulation time required to perform a full creep analysis results to be acceptable and suitable for model implementation in a decision support system. The creep analysis performed with the 1D FE model from 1969 up to 2040 lasted 8 hours, with an 8-core desktop machine, 32 GB of RAM and 2.10 GHz of CPU frequency, versus 12 plus days required to perform the same analysis by means of an already existing 3D ANSYS model of the viaduct. The main reason lies in the huge number of DoFs characterizing the 3D model, i.e. 260000 DoFs, versus 147 DoFs of the 1D model.

Another contribution of this thesis to the study of highly creep-sensitive concrete structures relates to the development of a novel creep constitutive law, which is characterized by a simpler form than Model B3, but highly accurate nonetheless. The proposed law is conceived for describing the aging hereditariness of concrete, but it can be successfully applied to the study of any other aging material by simply assigning different values to the model parameters. The principal novelty of the proposed law concerns the use of variable-order fractional operators for the description of the material aging. Moreover, another fundamental aspect relates to its simplicity, which allows the derivation of the relevant relaxation function from the fundamental relationship of linear viscoelasticity, impossible to obtain in presence of very complex law like the Model B3 one. More precisely, the relaxation function of the presented model is obtained by solving the Volterra integral equation with the iterated-kernels method and the Grünwald-Letnikov approximation. Thus, the accuracy of the resulting relaxation formula strictly depends on the number of kernels, set to 200, and the number of Grünwald-Letnikov terms, set to 170. Interesting comparisons between the novel creep model and Model B3 are also proposed, with the following conclusions: i) the approximate relaxation function of Model B3 is less accurate than the fractional-order relaxation function, except for the case of short-term relaxation beginning at young ages; and ii) the comparison between creep functions entails

percentage errors less than 6%, which is a reasonable value in engineering practice.

In order to further investigate the efficiency of the novel creep constitutive law previously presented, a compatible numerical integration scheme is finally provided in this thesis. As anticipated, the numerical scheme is characterized by a fractional-order aging kernel and relies on the energetic formulation proposed by Carini et al. (1995b). The convergence of the derived fractional-order integration scheme is investigated by means of an *a posteriori* accuracy analysis on a model problem, i.e. a clamped beam made of a medium strength concrete and subjected to a unitary stress at the free end, for which the exact viscoelastic solution is known. Moreover, by choosing different values of significant variables, like the number of Gaussian quadrature points ( $nG$ ) and subintervals ( $n$ ), the best solution in terms of accuracy and computational time is reached when  $nG = 8$  and  $n = 25$ , i.e.  $\Delta t = 360$  days for a creep analysis performed within  $[1000, 10000]$  days. Similar considerations are drawn though the application of the fractional-order integration scheme to more complex structures, including the main span of the Colle Isarco viaduct.

### 5.3 Future perspectives

A first interesting development of the work presented in this thesis entails the improvement of the efficiency of the 1D FE model. The model was utilized to study the behavior of the Colle Isarco viaduct and the relevant creep analysis required almost 8 hours. This simulation time is certainly satisfactory compared to the simulation time required by an already existing 3D model; however, it is still excessive in view of the model implementation in a decision support system. Possible solutions can be: i) to parallelize the algorithm for different load histories; and ii) to reduce the number of load histories by merging some of them. Further improvement of the 1D FE model may also concern its accuracy, which can be enhanced through the introduction of enriched finite elements. However, it is important to highlight that the use of a more refined FE model may increase the computational costs, making the model not suitable for a decision support system.

Further developments of this thesis may also involve the proposed creep constitutive

law and its three parameters,  $C_\beta(t_0)$ ,  $\beta(t_0)$  and  $G_\beta(t_0)$ . In this thesis, they are derived for a medium-strength concrete with the aid of Model B3. However, a more refined characterization of such parameters can be achieved through: i) the use of experimental data for the best-fitting procedure, such as the one collected in the RILEM database (RILEM, 2016); and ii) the study of the influence that mechanical properties, environmental conditions, and cross-section geometry may have on their trends.

Eventually, the numerical integration scheme, proposed for the novel fractional-order constitutive law, can be extended to include shear deformations; and the same scheme can be formulated for more general 2D and 3D bodies.

## Bibliography

- Committee ACI. Guide for modeling and calculating shrinkage and creep in hardened concrete. *ACI Committee*, 2008.
- Gianluca Alaimo and Massimiliano Zingales. Laminar flow through fractal porous materials: the fractional-order transport equation. *Communications in Nonlinear Science and Numerical Simulation*, 22(1):889–902, 2015.
- Daniel Balageas, Claus-Peter Fritzen, and Alfredo Güemes. *Structural health monitoring*, volume 90. John Wiley & Sons, 2010.
- Zdeněk P Bažant. Prediction of concrete creep effects using age-adjusted effective modulus method. In *ACI Journal Proceedings*, volume 69. ACI, 1972.
- Zdeněk P. Bažant. Theory of creep and shrinkage in concrete structures: a précis of recent developments, mechanics today, vol. 2, 1975.
- Zdeněk P. Bažant and Sandeep Baweja. Creep and shrinkage prediction model for analysis and design of concrete structures: Model b3. *ACI Special Publications*, 194:1–84, 2000.
- Zdeněk P Bažant and Sang-Sik Kim. Approximate relaxation function for concrete. *Journal of the Structural Division*, 105(12):2695–2705, 1979.
- Zdeněk P Bažant and Robert L’Hermite. *Mathematical modeling of creep and shrinkage of concrete*. Wiley Chichester, 1988.
- Zdeněk P Bažant and Guang-Hua Li. Comprehensive database on concrete creep and shrinkage. *ACI Materials Journal*, 105(6):635–637, 2008.
- Zdeněk P. Bažant and Liisa Panula. Creep and shrinkage characterization for analyzing prestressed concrete structures. *PCI journal*, 25(3):86–122, 1980.
- Zdeněk P Bažant and Santosh Prasannan. Solidification theory for concrete creep. i: Formulation. *Journal of engineering mechanics*, 115(8):1691–1703, 1989.

Zdeněk P Bažant and Folker H Wittmann. Creep and shrinkage in concrete structures. 1982.

Zdeněk P Bažant and XI Yunping. Drying creep of concrete: constitutive model and new experiments separating its mechanisms. *Materials and structures*, 27(1):3–14, 1994.

Zdeněk P Bažant, Anders Boe Hauggaard, Sandeep Baweja, and Franz-Josef Ulm. Microprestress-solidification theory for concrete creep. i: Aging and drying effects. *Journal of Engineering Mechanics*, 123(11):1188–1194, 1997.

Zdeněk P Bažant, Qiang Yu, and Guang-Hua Li. Excessive long-time deflections of prestressed box girders. i: Record-span bridge in palau and other paradigms. *Journal of structural engineering*, 138(6):676–686, 2012.

Zdeněk P Bažant, Mija H Hubler, and Milan Jirásek. Improved estimation of long-term relaxation function from compliance function of aging concrete. *Journal of Engineering Mechanics*, 139(2):146–152, 2013.

Angela Beltempo, Carlo Cappello, Daniele Zonta, Alessio Bonelli, Oreste S. Bursi, Carlo Costa, and Walter Pardatscher. Structural health monitoring of the colle isarco viaduct. In *Environmental, Energy and Structural Monitoring Systems (EESMS), 2015 IEEE Workshop on*, pages 7–11. IEEE, 2015.

Angela Beltempo, Massimiliano Zingales, Oreste S. Bursi, and Luca Deseri. A fractional-order model for aging materials: An application to concrete. *International Journal of Solids and Structures*, 2017. ISSN 0020–7683. doi: <https://doi.org/10.1016/j.ijsolstr.2017.12.024>.

Angela Beltempo, Oreste S. Bursi, Carlo Cappello, Daniele Zonta, and Massimiliano Zingales. A viscoelastic model for the long-term deflection of segmental prestressed box girders. *Computer-Aided Civil and Infrastructure Engineering*, 33(1):64–78, 2018. ISSN 1467-8667. doi: 10.1111/mice.12311.

- Maurice A. Biot. *Variational and Lagrangian Methods in Viscoelasticity*, pages 251–263. Springer Berlin Heidelberg, Berlin, Heidelberg, 1956. ISBN 978-3-642-48236-6. doi: 10.1007/978-3-642-48236-6\_23.
- George W. Scott Blair. *A survey of general and applied rheology*. Sir Isaac Pitman & Sons, 1949.
- William M. Bolstad. *Understanding computational Bayesian statistics*, volume 644. John Wiley & Sons, 2010.
- Ludwig Boltzmann. Zur theorie der elastischen nachwirkung. *Annalen der Physik*, 241 (11):430–432, 1878.
- Donatella Bongiorno. Riemann-type definition of the improper integrals. *Czechoslovak Mathematical Journal*, 54(3):717–725, 2004.
- Donatella Bongiorno. Metric differentiability of lipschitz maps. *Journal of the Australian Mathematical Society*, 96(1):25–35, 2014.
- Donatella Bongiorno and Giuseppa Corrao. On the fundamental theorem of calculus for fractal sets. *Fractals*, 23(02):1550008, 2015a.
- Donatella Bongiorno and Giuseppa Corrao. An integral on a complete metric measure space. *Real Analysis Exchange*, 40(1):157–178, 2015b.
- Donatella Bongiorno et al. A regularity condition in sobolev spaces. *Illinois Journal of Mathematics*, 46(2):557–570, 2002.
- Sholmo Breuer. Minimum principles for incompressible viscoelastic solids. *Meccanica*, 8(2):102–104, Jun 1973. ISSN 1572-9648. doi: 10.1007/BF02155849.
- Salvatore Butera and Mario Di Paola. Mellin transform approach for the solution of coupled systems of fractional differential equations. *Communications in Nonlinear Science and Numerical Simulation*, 20(1):32–38, 2015.

- Carlo Cappello, Daniele Zonta, Matteo Pozzi, Branko Glisic, and Riccardo Zandonini. Impact of prior perception on bridge health diagnosis. *Journal of Civil Structural Health Monitoring*, 5(4):509–525, 2015.
- Carlo Cappello, Daniele Zonta, and Branko Glišić. Expected utility theory for monitoring-based decision-making. *Proceedings of the IEEE*, 104(8):1647–1661, 2016.
- Luca Caracoglia, Salvatore Noè, and Vincenzo Sepe. Nonlinear computer model for the simulation of lock-in vibration on long-span bridges. *Computer-Aided Civil and Infrastructure Engineering*, 24(2):130–144, 2009.
- Angelo Carini, Piero Gelfi, and Egidio Marchina. An energetic formulation for the linear viscoelastic problem. part ii: step-by-step time integration approach. Technical report, University of Brescia (Italy), 1995a.
- Angelo Carini, Piero Gelfi, and Egidio Marchina. An energetic formulation for the linear viscoelastic problem. part i: Theoretical results and first calculations. *International journal for numerical methods in engineering*, 38(1):37–62, 1995b.
- Erasmus Cataldo, Salvatore Di Lorenzo, Vincenzo Fiore, Mirko Maurici, Francesco Nicoletti, Antonina Pirrotta, Roberto Scaffaro, and Antonino Valenza. Bending test for capturing the vivid behavior of giant reeds, returned through a proper fractional viscoelastic model. *Mechanics of Materials*, 89:159–168, 2015.
- MC90 CEB-FIP. 90, design of concrete structures. ceb-fip model code 1990. *British Standard Institution, London*, 1993.
- (European Committee for Standardization) CEN. *Eurocode 2: Design of Concrete Structures: Part 1-1: General Rules and Rules for Buildings*. British Standards Institution, 2004.
- Mario A. Chiorino. *CEB Design Manual on Structural Effects of Time-dependent Behaviour of Concrete*. CEB bulletin d’information. Georgi Publishing Company, 1984. ISBN 9782604000679.

- Richard M. Christensen. Variational and minimum theorems for the linear theory of viscoelasticity. *Zeitschrift für angewandte Mathematik und Physik ZAMP*, 19(2):233–243, Mar 1968. ISSN 1420-9039. doi: 10.1007/BF01601468.
- Richard M. Christensen. Theory of viscoelasticity: An introduction academic. *New York*, 1971.
- Richard M. Christensen. *Theory of viscoelasticity: an introduction*. Elsevier, 2012.
- Carlos FM Coimbra. Mechanics with variable-order differential operators. *Annalen der Physik*, 12(11-12):692–703, 2003.
- Fernando Cortés and María Jesús Elejabarrieta. Finite element formulations for transient dynamic analysis in structural systems with viscoelastic treatments containing fractional derivative models. *International journal for numerical methods in engineering*, 69(10): 2173–2195, 2007.
- Luca Deseri, Mario Di Paola, Massimiliano Zingales, and Pietro Pollaci. Power-law hereditarity of hierarchical fractal bones. *International journal for numerical methods in biomedical engineering*, 29(12):1338–1360, 2013.
- Luca Deseri, Mario Di Paola, and Massimiliano Zingales. Free energy and states of fractional-order hereditarity. *International Journal of Solids and Structures*, 51(18): 3156–3167, 2014a.
- Luca Deseri, Massiliano Zingales, and Pietro Pollaci. The state of fractional hereditary materials (fhm). *Discr. Contin. Dyn. Syst. Ser. B*, 19:2065–2089, 2014b.
- Luca Deseri, Massiliano Zingales, and Pietro Pollaci. The state of fractional hereditary materials (fhm). *Discrete and Continuous Dynamical Systems - Series B*, 19(7):2065–2089, 2014c.
- Mario Di Paola and Michele Fabio Granata. Fractional model of concrete hereditary viscoelastic behaviour. *Archive of Applied Mechanics*, pages 1–14, 2016.

- Mario Di Paola and Massimiliano Zingales. Exact mechanical models of fractional hereditary materials (fhm). *Journal of Rheology*, 58:986–1004, 2012.
- Mario Di Paola, Antonina Pirrotta, and Antonino Valenza. Visco-elastic behavior through fractional calculus: an easier method for best fitting experimental results. *Mechanics of Materials*, 43(12):799–806, 2011.
- Mario Di Paola, R. Heuer, and Antonina Pirrotta. Fractional visco-elastic eulerbernoulli beam. *International Journal of Solids and Structures*, 50(22):3505 – 3510, 2013a. ISSN 0020-7683. doi: <https://doi.org/10.1016/j.ijsolstr.2013.06.010>.
- Mario Di Paola, Francesco Paolo Pinnola, and Massimiliano Zingales. Fractional differential equations and related exact mechanical models. *Computers & Mathematics with Applications*, 66(5):608–620, 2013b.
- Aleksey D. Drozdov. *Viscoelastic structures: mechanics of growth and aging*. Academic Press, 1998.
- Michael Evans and Tim Swartz. Methods for approximating integrals in statistics with special emphasis on bayesian integration problems. *Statistical Science*, pages 254–272, 1995.
- Michael H. Faber and Marc A. Maes. Issues in societal optimal engineering decision making. *Structure and Infrastructure Engineering*, 4(5):335–351, 2008.
- Wilhelm Flügge. *Viscoelasticity*. Springer Science & Business Media, 2013.
- Andrew Gemant. Xlv. on fractional differentials. *The London, Edinburgh, and Dublin Philosophical Magazine and Journal of Science*, 25(168):540–549, 1938.
- Lino Gentilini and Bruno Gentilini. Il viadotto di colle isarco per l’autostrada del brennero. *L’Industria Italiana del Cemento (in Italian)*, 1972.
- Branko Glisic and Daniele Inaudi. *Fibre optic methods for structural health monitoring*. John Wiley & Sons, 2008.

- Rajeev Goel, Ram Kumar, and DK Paul. Comparative study of various creep and shrinkage prediction models for concrete. *Journal of materials in civil engineering*, 19(3):249–260, 2007.
- M. E. Gurtin. Variational principles in the linear theory of viscoelasticity. *Archive for Rational Mechanics and Analysis*, 13(1):179–191, Dec 1963. ISSN 1432-0673. doi: 10.1007/BF01262691.
- Bing Han, Tian-Yu Xiang, and Hui-Bing Xie. A bayesian inference framework for predicting the long-term deflection of concrete structures caused by creep and shrinkage. *Engineering Structures*, 142:46–55, 2017.
- C. Huet. Minimum theorems for viscoelasticity. *European Journal of Mechanics, A/Solids*, 11(5):653–684, 1992. cited By 14.
- Alexander Idesman, Rainer Niekamp, and Erwin Stein. Continuous and discontinuous galerkin methods with finite elements in space and time for parallel computing of viscoelastic deformation. *Computer methods in applied mechanics and engineering*, 190(8):1049–1063, 2000.
- Dov Ingman and Joseph Suzdalnitsky. Application of differential operator with servo-order function in model of viscoelastic deformation process. *Journal of Engineering Mechanics*, 131(7):763–767, 2005.
- Milan Jirásek and Zdenek P Bazant. *Inelastic analysis of structures*. John Wiley & Sons, 2002.
- Les Kirkup and Robert B. Frenkel. *An introduction to uncertainty in measurement: using the GUM (guide to the expression of uncertainty in measurement)*. Cambridge University Press, 2006.
- Stig Larsson, Milena Racheva, and Fardin Saedpanah. Discontinuous galerkin method for an integro-differential equation modeling dynamic fractional order viscoelasticity.

*Computer Methods in Applied Mechanics and Engineering*, 283(Supplement C):196 – 209, 2015. ISSN 0045-7825. doi: <https://doi.org/10.1016/j.cma.2014.09.018>.

Carl F. Lorenzo and Tom T. Hartley. Initialization, conceptualization, and application in the generalized fractional calculus. 1998.

Carl F. Lorenzo and Tom T. Hartley. Variable order and distributed order fractional operators. *Nonlinear dynamics*, 29(1-4):57–98, 2002.

Carl F. Lorenzo and Tom T. Hartley. Initialization, conceptualization, and application in the generalized (fractional) calculus. *Critical Reviews in Biomedical Engineering*, 35 (6), 2007.

Richard L. Magin, Carson Ingo, Luis Colon-Perez, William Triplett, and Thomas H. Mareci. Characterization of anomalous diffusion in porous biological tissues using fractional order derivatives and entropy. *Microporous and Mesoporous Materials*, 178: 39–43, 2013.

Francesco Mainardi. Fractional calculus. In *Fractals and fractional calculus in continuum mechanics*, pages 291–348. Springer, 1997.

Francesco Mainardi. *Fractional Calculus and Waves in Linear Viscoelasticity*, volume 198. Academic press, 2010.

S Mazzoni, F Mckenna, and GL Fenves. Opensees command language manual v. 1.7. 3. department of civil environmental engineering. *University of California: Berkeley, CA, USA*, 2006.

Gaetano Di Mino, Gordon Airey, Mario Di Paola, Francesco Paolo Pinnola, Giacomo D'Angelo, and Davide Lo Presti. Linear and nonlinear fractional hereditary constitutive laws of asphalt mixtures. *Journal of Civil Engineering and Management*, 22(7):882–889, 2016.

- Silvano Mussi. Putting value of information theory into practice: a methodology for building sequential decision support systems. *Expert Systems*, 21(2):92–103, 2004.
- Marco Musto and Giulio Alfano. A fractional rate-dependent cohesive-zone model. *International Journal for Numerical Methods in Engineering*, 103(5):313–341, 2015.
- P. G. Nutting. A new general law of deformation. *Journal of the Franklin Institute*, 191(5):679–685, 1921.
- Gerald Pickett. The effect of change in moisture-content on the crepe of concrete under a sustained load. In *Journal Proceedings*, volume 38, pages 333–356, 1942.
- Igor Podlubny. *Fractional differential equations: an introduction to fractional derivatives, fractional differential equations, to methods of their solution and some of their applications*, volume 198. Academic press, 1998.
- P. Rafalski. Orthogonal projection method, iii. linear viscoelastic problem. *Bull. Acad. Pol. Sci., Ser. Sci. Tech.*, 17:167, 1969. cited By 2.
- R. Reiss and E.J. Haug. Extremum principles for linear initial-value problems of mathematical physics. *International Journal of Engineering Science*, 16(4):231 – 251, 1978. ISSN 0020-7225. doi: [https://doi.org/10.1016/0020-7225\(78\)90090-3](https://doi.org/10.1016/0020-7225(78)90090-3).
- RILEM. Database on creep and shrinkage of concrete and concrete structures. *website: <http://www.civil.northwestern.edu/people/bazant/>*, hosted by Professor Z.P. Bazant, 2016.
- S.G. Samko, A.A. Kilbas, and O.I. Marichev. Fractional integrals and derivatives and some of their applications. *Science and Technica*, 1, 1987.
- Vicki L. Sauter. *Decision support systems for business intelligence*. John Wiley & Sons, 2014.
- Robert Schlaifer and Howard Raiffa. *Applied statistical decision theory*. 1961.

- Kelli Shapiro. *Finite-element modeling of a damaged prestressed concrete bridge*. PhD thesis, 2007.
- Devinderjit Sivia and John Skilling. *Data analysis: a Bayesian tutorial*. OUP Oxford, 2006.
- Michael Smith. *ABAQUS/Standard User's Manual, Version 6.9*. Simulia, 2009.
- Daniel Straub. Value of information analysis with structural reliability methods. *Structural Safety*, 49:75–85, 2014.
- N.H. Sweilam and H.M. AL-Mrawm. On the numerical solutions of the variable order fractional heat equation. *Studies in Nonlinear Sciences*, 2(1):31–36, 2011.
- Robert L. Taylor, Karl S. Pister, and Gerald L. Goudreau. Thermomechanical analysis of viscoelastic solids. *International Journal for Numerical Methods in Engineering*, 2(1): 45–59, 1970. ISSN 1097-0207. doi: 10.1002/nme.1620020106.
- J.A. Tenreiro Machado, Manuel F. Silva, Ramiro S. Barbosa, Isabel S. Jesus, Cecília M. Reis, Maria G. Marcos, and Alexandra F. Galhano. Some applications of fractional calculus in engineering. *Mathematical Problems in Engineering*, 2010, 2010.
- E. Tonti. Variational formulation for every nonlinear problem. *International Journal of Engineering Science*, 22(11):1343 – 1371, 1984. ISSN 0020-7225. doi: [https://doi.org/10.1016/0020-7225\(84\)90026-0](https://doi.org/10.1016/0020-7225(84)90026-0).
- Marco Torbol, Hugo Gomez, and Maria Feng. Fragility analysis of highway bridges based on long-term monitoring data. *Computer-Aided Civil and Infrastructure Engineering*, 28(3):178–192, 2013.
- Francesco Giacomo Tricomi. *Integral equations*, volume 5. Courier Corporation, 1957.
- Duarte Valério and Jose Sa Da Costa. Variable-order fractional derivatives and their numerical approximations. *Signal Processing*, 91(3):470–483, 2011.

Massimo Viviani. Consolidamento strutturale dell'impalcato del viadotto colle isarco, a progressiva km 8+957. Technical report, Autostrada del Brennero SpA (in Italian), 2013.

Vito Volterra. Theory of functionals and of integral and integro-differential equations. 1959.

John Von Neumann and Oskar Morgenstern. *Theory of games and economic behavior*. Princeton university press, 2007.

R. Wendner, M. H. Hubler, and Z. P. Bazant. The b4 model for multi-decade creep and shrinkage prediction. In *Conference: Ninth International Conference on Creep, Shrinkage, and Durability Mechanics (CONCREEP-9)*, 2013.

Takahiro Yajima and Kazuhito Yamasaki. Geometry of surfaces with caputo fractional derivatives and applications to incompressible two-dimensional flows. *Journal of Physics A: Mathematical and Theoretical*, 45(6):065201, 2012.